NEUTRONIC ANALYSIS AND OPTIMIZATION OF THE ADVANCED HIGH TEMPERATURE REACTOR FUEL DESIGN USING MACHINE LEARNING

A Dissertation
Presented to
The Academic Faculty

by

Lloyd Michael Huang

In Partial Fulfillment
of the Requirements for the Degree
Doctor of Philosophy
Nuclear and Radiological Engineering Program
School of Mechanical Engineering

Georgia Institute of Technology
August 2017

NEUTRONIC ANALYSIS AND OPTIMIZATION OF THE LIQUID SALT COOLED REACTOR FUEL DESIGN USING MACHINE LEARNING

Approved by:

Dr. Bojan Petrovic Advisor
Nuclear and Radiological Engineering Program
School of Mechanical Engineering
Georgia Institute of Technology

Dr. Dingkang Zhang
Nuclear and Radiological Engineering Program
School of Mechanical Engineering
Georgia Institute of Technology

Dr. Weston Stacey
Nuclear and Radiological Engineering Program
School of Mechanical Engineering
Georgia Institute of Technology

Dr. Ivan Maldonado
Department of Nuclear Engineering
College of Engineering
University of Tennessee Knoxville

Dr. Farzad Rahnema
Nuclear and Radiological Engineering Program
School of Mechanical Engineering
Georgia Institute of Technology

Date Approved: June 9th, 2017

ACKNOWLEDGEMENTS

First and foremost, I thank and praise God Almighty, his love always working in my life to give me strength and help me mature. I would not have been able to persist in my studies without his care.

I express my deepest gratitude to Dr. Bojan Petrovic, my faculty advisor, for his guidance and patience in helping me to reach my goals. It is with his advice that this dissertation was made possible.

Also, I very thankful for the support of my PhD committee in giving guidance and feedback on my research and ensuring the quality of my work.

I am abundantly thankful for my loving wife who supported me through some of the hardest years of my life. I have learned more about myself through our relationship than any other time in my life.

I give thanks to my loving Mother and Father, to all of my family and friends who are caring and supportive of my endeavors. I am truly blessed to have the love and care of many good people in my life.

Research presented in this dissertation was performed using funding received from the US Department of Energy under the Nuclear Energy University Program (NEUP) Project 12-3870, "Fuel and Core Design Options to Overcome the Heavy Metal Loading Limit and Improve Performance and Safety of Liquid Salt Cooled Reactors", and Integrated Research Project (IRP) 14-7829, "Integrated Approach to Fluoride High Temperature Reactor Technology and Licensing Challenges".

TABLE OF CONTENTS

LIST OF TABLES

LIST OF FIGURES

LIST OF ABBREVIATIONS

AHTR	Advanced High Temperature Reactor
TRISO	Tristructural-Isotropic Fuel
HTR	High Temperature Reactor (Gas cooled)
CHM	Carbon-to-heavy-metal Ratio
ORNL	Oak Ridge National Laboratory
CE	Continuous Energy Neutron Transport
LRM	Linear Reactivity Model
NLRM	Non-linear Reactivity Model
UTK	University of Tennessee Knoxville
FHR	Fluoride-salt-cooled High Temperature Reactor
PB-AHTR	Pebble-bed Advanced High Temperature Reactor
ANN	Artificial Neural Network
MG	Multi-group Neutron Transport
BOC	Beginning of Cycle
PMF	Pitch Modification Factor
FPD	Full Power Days
EOC	End of Cycle
MOC	Middle of Cycle
LOCA	Loss of Coolant Accident
LHS	Latin Hypercube Sampling
MLP	Multi-layer Perceptron
PReLU	Parametric Rectified Linear Unit
SGD	Stochastic Gradient Decent
PNA	Preferred Neighborhood Aggregation
CDF	Cumulative Distribution Function
DE	Differential Evolution
GA	Genetic Algorithm
Fev	Objective Function Evaluations

FCC	Fuel Cycle Cost

SUMMARY

Gen IV reactor designs show promise in providing safer, cleaner and potentially cheaper options for electricity generation. The Advanced High Temperature Reactor (AHTR) is a Gen IV reactor design that can provide cheaper electricity costs safely due to its operation at low, near-atmospheric pressure and increased thermodynamic efficiency due to higher temperatures. However, this new design concept is challenging to model, making design optimization more computationally expensive.

A new methodology for design optimization of double heterogeneous fuel in the AHTR is evaluated in this dissertation. The approach is to apply physics-based approximations to the neutronics calculations allowing for a practical analysis of the design space. Then, using advanced sampling techniques and artificial neural networks, surrogate models are created to generate the constrained objective function for optimization. A novel optimization algorithm was developed to efficiently find the optimal design and the region of solutions near the optimal design in a concave nonlinear design space. This approach provides a rigorous design optimization search and characterizes the sensitivity of the solutions near the optimum with regards to the features of the model. This helps with understanding how optimal costs are affected by changes in external factors.

CHAPTER 1

INTRODUCTION

As evidence of the harmful effects of fossil fuel emissions continues to grow in our daily lives, cleaner technology is being developed in an effort to mitigate the potentially disastrous effects of pollution and reduce the cost of electricity. Arguments are being made about which solutions are most effective. Decreasing harmful emissions requires a technology that can cheaply and cleanly meet electricity demand. Nuclear power has the ability to meet these requirements safely. In particular Gen IV reactor designs, including the Advanced High Temperature Reactor (AHTR), have very attractive features that improve safety and economics of nuclear power generation.

The AHTR is a relatively new design concept and further design optimization is needed to provide the most economic and safe configuration. The fuel cycle cost of running a reactor is extremely sensitive to design parameters and a small change in performance effects the economic gain by many millions of dollars. In recent years, artificial intelligence has become a very powerful tool for analysis of large multidimensional data sets. Advances in this field have made the tool more widely available and improved the performance dramatically. This research combines the fields of nuclear engineering and artificial intelligence to provide a rigorous optimization methodology to solve a challenging reactor physics and statistics problem.

1.1 AHTR Design Background

The AHTR is a 3400 MWth high temperature reactor concept with 252 hexagonal fuel assemblies with Tristructural-isotropic fuel particles (TRISO) sintered into planks

cooled by liquid FLiBe salt. This design operates at low, near-atmospheric pressure and at high temperature. It is designed to tolerate high temperatures and high burnup. Overall, the AHTR design is expected to be more economic and safer, but low heavy metal loading presents a challenge to optimizing the fuel design's performance, potentially resulting in higher fuel cycle costs [13], [33]. Also, the complex double heterogeneous geometry presents a major neutronics modeling challenge.

TRISO particles are coated fuel particles with three outer layers. The fuel kernel has a radius of 213.5 μm. The first layer is comprised of thick porous carbon designed to trap most of the fission product gasses and allow for fuel swelling. The second layer is a SiC shell that provides structural support. The outermost shell is dense pyrocarbon. The fuel kernel is made of uranium oxycarbide, UCO, which in reality may have a complex chemical composition, such as 71.4% UO_2, 12.3% $UC_{1.86}$, and 16.4% UC reported for test HTR fuel kernels [25].

Each fuel assembly has 18 fuel plates with three groups of 6 rotated 120 degrees around a central graphite moderator region which also contains the control blade. Each fuel plank has two fuel stripes with TRISO particles randomly dispersed inside a carbon matrix on either side of a center carbon moderator region. The fuel planks are six meters tall with an active fuel length of 5.5 m. The 2011 design fuel planks are 2.55 cm thick. The fuel plank design modeled in this research uses a thickness of 2.735 cm, which was increased based on preliminary analysis in order to increase moderation with a nearly negligible increase in average fuel temperature. This FHR design uses carbon, graphite, and FLiBe as moderating materials resulting in a thermal spectrum. However, the spectrum is harder than in a LWR since, for the same volume, carbon is not as effective a

moderator as water. Two important parameters that affect moderation in the fuel design are packing fraction and fuel stripe thickness. As packing fraction and the number of fuel layers is decreased, the carbon-to-heavy-metal ratio (CHM) increases. CHM refers to carbon atom to fuel atom ratio in the fuel plank. The initial conceptual 2011 design [13] had a CHM of roughly 200 and an enrichment of 19.75%, while a more updated design from 2012 [33] has a CHM of 400 and 9% enriched uranium, resulting in a much softer spectrum. Figure 1 shows the neutron spectrum of the AHTR with different CHM and enrichment compared to a standard PWR spectrum.

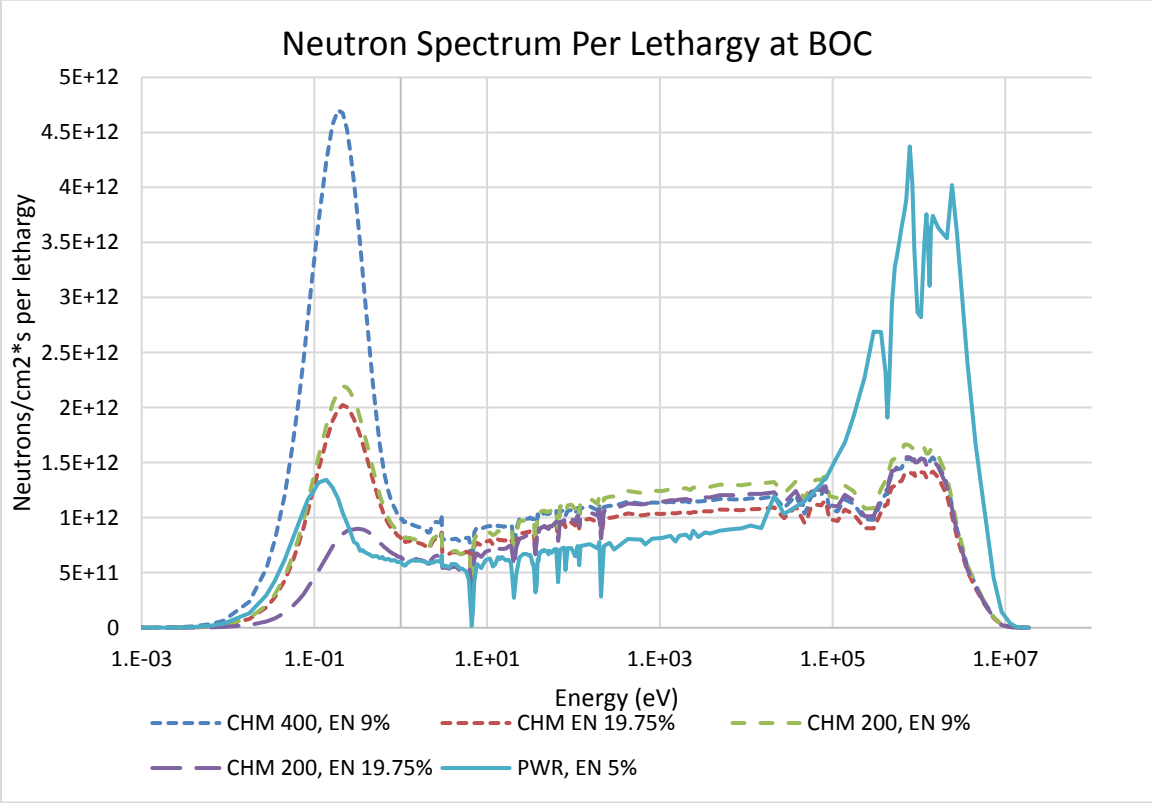

Figure 1. Neutron spectrum per lethargy for AHTR designs with different CHM and enrichment compared to a PWR spectrum.

The above figure shows increasing CHM and decreasing enrichment significantly softens the spectrum. The fast flux is lower compared to the PWR fast flux due to the lower heavy metal loading, but the epithermal flux is higher due to the higher mass of carbon compared to hydrogen. The updated design has a two batch cycle length of six months [13], [33]. The coolant outlet temperature is 750 °C. The average fuel temperature is roughly 825 °C. Figure 2 shows the cross-section of the fuel plank design. Figure 3 shows the cross section of the fuel assembly design [13].

Table 1 displays values for some important design parameters. Research in this dissertation presents a methodology for modeling the difficult neutronics of the design and a new methodology for optimizing the fuel design with machine learning algorithms. Parameters of interest for optimization include packing fraction, fuel stripe thickness, enrichment, and number of batches for refueling.

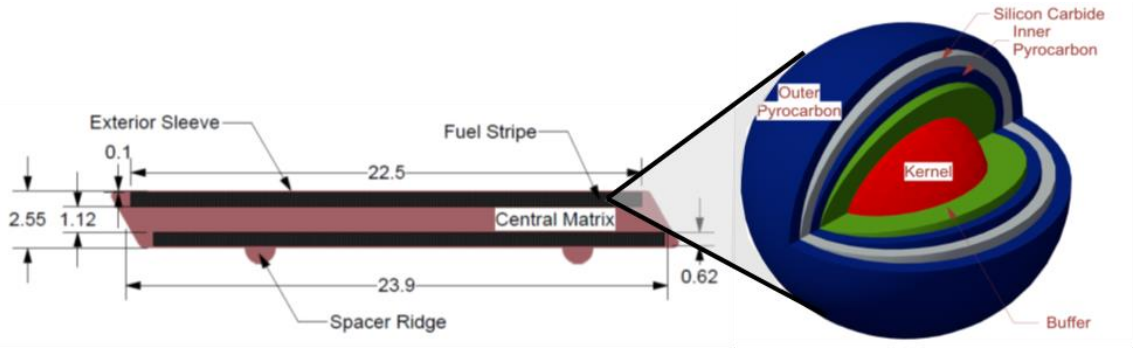

Figure 2. Fuel plank 2011 design cross-section with dimensions shown in cm [13].

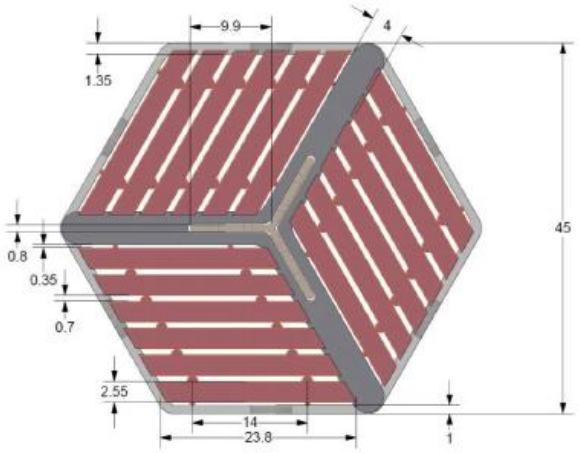

Figure 3. Fuel assembly cross-section with dimensions shown in cm [13].

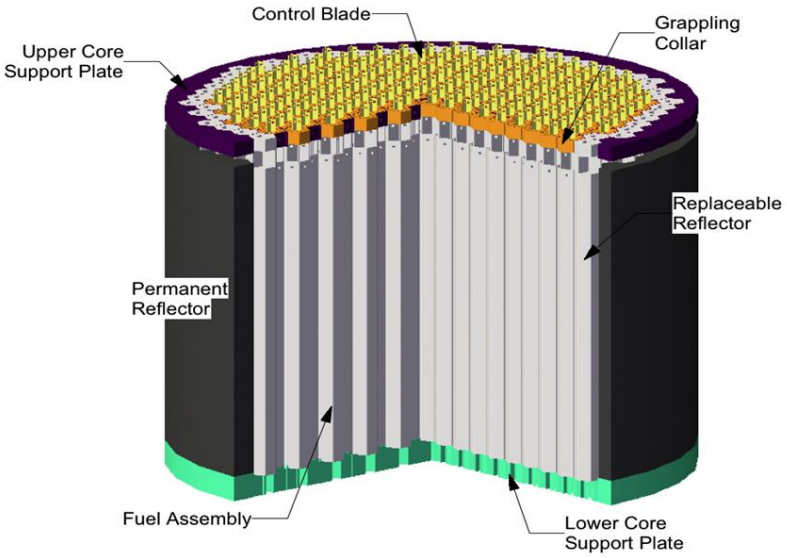

Figure 4. Cutaway of the AHTR core design, from upper support plate to lower support plate [13].

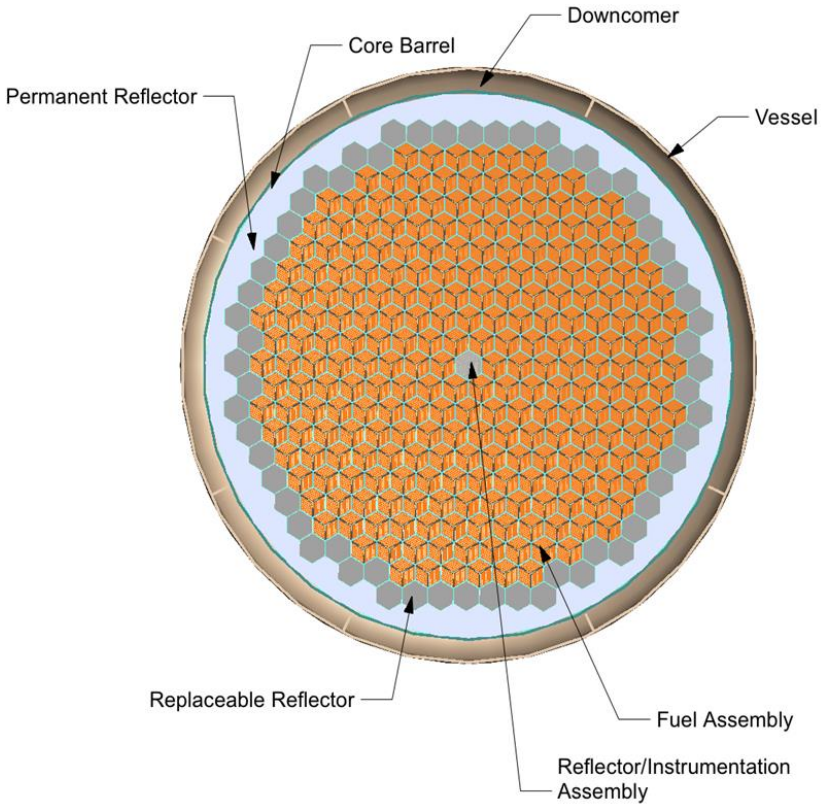

Figure 5. Cross-sectional view of the AHTR core [13].

Table 1. Geometric and composition parameters for the FHR.

Assembly Model Dimensions and Compositions at 40% PF	
Reactor Power	3400 MWt
Thermal Efficiency	~45%
Number of Fuel Assemblies	253
Assembly Half Pitch	23.375 cm
Plate Thickness	2.735 cm
Thickness of Fuel Regions	0.649 cm
Plate Sleeve Thickness	1 mm
TRISO Pitch	926 μm
Fuel Kernal Radius	213.5 μm
Core height (fueled region)	5.5 m
Core height (including axial reflector)	6 m
Equivalent core diameter (fueled region)	7.81 m
Core diameter (including radial reflector)	9.56 m
Fuel Material	Uranium Oxycarbide
Moderator Material	Graphite/Amorphous Carbon
Coolant	Li_2BeF_4 (Flibe)
Fuel Density	10.9 g/cc
Fuel Enrichment	< 20%
Average Coolant Temperature	948.15 K
Coolant Pressure	atmospheric
Core Volume	263.38 m^3
Core Power Density	12.91 MW/m^3
Mass Flow Rate	28408.1 kg/s
Average Coolant Velocty	1.93 m/s

1.2 Previous FHR Research

Several previous studies contributed to improvements in the neutronics modeling of AHTRs. Important work on modeling double heterogeneous geometry in multi-group approximation using MCDancoff Factor was performed at ORNL [16]. In this study an iterative method using continuous energy transport calculations and adjusting the Dancoff Factor until multi-group transport matched the CE calculation was evaluated. In addition to this work, a study at ORNL showed that the Linear Reactivity Model (LRM) is

insufficient for multi-batch depletion analysis when compared to a simple Non-linear Reactivity Model (NLRM) [5].

Research at Georgia Tech was performed to analyze the effect of different levels of homogenization on the prediction of K_{inf}. The study also included a comparison of cycle length between reflected single fuel assembly models and a full core model [21]. This research led to useful approximations that decreased runtimes with minimal impact on accuracy.

A different study at University of Tennessee Knoxville (UTK) using SERPENT evaluated effects of fuel geometry and random TRISO dispersion. It was shown that modeling the TRISO particles in a uniform lattice leads to errors up to 300 pcm [10]. The study also included a parametric evaluation of the fuel assembly dimensions and composition, relating to cycle length, burnup, and reactivity coefficients [27], [10], [11].

Some important preliminary thermal hydraulics calculations were performed partly in support of neutronics calculations by Pietro Avigni. Work was done to develop a 1D single channel thermal hydraulics model which was used for neutronics parametric studies in previous research for the AHTR. The model provides average temperatures in the different parts of the plank and the coolant as reactor power or pumping power, channel width, and other parameters are changed [2], [27].

Several previous efforts have been made to model the economics and fuel cycle cost of the AHTR. These studies also include initial optimization calculations under different assumptions and economic scenarios [23], [18], [14]. A major issue to be resolved in modeling the fuel cycle cost is due to the large uncertainty in the manufacturing cost of TRISO fuel.

There are other projects contributing to FHR technology that take a different approach to improving the fuel cycle cost of FHRs. At Berkeley the Pebble Bed Advanced High Temperature Reactor (PB-AHTR) takes an online refueling approach to optimizing the fuel cycle. This design approach allows for more electricity to be generated from less uranium and achieves excellent fuel utilization. However, one drawback of this approach is the need for an on-line refueling machine. For simulations, the challenge is in the random nature of the pebble packing leaving a high uncertainty for calculating reactivity coefficients [9].

An innovative, even more radical, approach was investigated by Pietro Avigni that involves online on-power refueling with AHTR plank assemblies. This work provided preliminary calculations to show the possibility of maintaining power stability and thermal margins during the full power refueling process. This approach also provides a more efficient and potentially more economic use of nuclear fuel. Also, this design approach provides a more straight forward way of verifying negative reactivity temperature coefficients since the geometry does not change randomly during refueling. More work needs to be done for this approach since there is uncertainty around the need for active controls during refueling to prevent a power spike [1]. In general, the online refueling approach requires further investigation for the feasibility and verification of the theoretical economic advantage. It is uncertain how the cost of online refueling devices and maintenance will impact overall costs. The current traditional multi-batch refueling is well established and provides a more straight-forward approach to developing a reactor design optimization methodology.

1.3 Motivation

The AHTR provides several advantages over current LWR technology. It operates at high temperature increasing thermodynamic efficiency. The reactor operates at low, near-atmospheric pressure reducing the structural requirements of the pressure vessel and reducing capital cost. TRISO fuel particles give additional layers of safety for trapping fission products and fission product gasses in the event of an accident. Also, the fuel is able to achieve a higher burnup because of the more robust fuel form and materials inside the core.

There are several challenges for the progression of the AHTR design. The high temperatures, high burnup, and corrosive coolant, make materials development important, especially with regard to the structural materials. Also, the toxicity of the coolant, which contains beryllium, contributes to more stringent safety requirements throughout the fuel cycle. Tritium production is another significant operational challenge. These issues, while important for the development of the AHTR, are beyond the scope of this dissertation. The main challenge addressed in this research is the low heavy metal loading which makes minimizing the fuel cycle cost more difficult. Another very important issue is the double heterogeneous geometry, which greatly increases the complexity of generating multi-group cross-sections. This results in extremely long computational runtimes for neutronics calculations and is limiting for modeling the highly non-linear non-convex design space. The focus of this work is therefore to develop a methodology that couples high fidelity neutronics calculations with rigorous optimization calculations with machine learning techniques to reduce necessary computational resources for design optimization.

1.4 Research Objectives and Approach

The purpose of this research is to develop a methodology to model the challenging neutronics of the AHTR and to minimize the fuel cycle cost. The approach is to model neutronics with high fidelity and then evaluate which approximations are most beneficial since CE depletion runtimes are impractically long. The first approximation is to model a single fuel assembly, with appropriate corrections, to represent the whole core and obtain the parameters of interest (e.g., cycle length) with acceptable accuracy. This is a frequently used approach in fuel cycle studies [7]. Even with approximations the depletion calculations are quite expensive. Taking this into account, a modeling methodology that can accurately model the physics over the large design space given sparse data points is necessary. In order to achieve the goal of this research, a neutronics modeling methodology was developed to efficiently approximate high fidelity neutronics over the design space using surrogate models. The problem then becomes a constrained non-convex global optimization problem. The objective of this research is to accurately model the physics and to solve this difficult optimization problem.

Modeling the neutronics is challenging due to the double heterogeneous geometry. A major objective of this research is to develop an efficient methodology to model the double heterogeneity over the design space. This methodology makes use of the multi-group approximation to reduce required runtime with minimal impact on accuracy. In order to make use of the multi-group approximation the double-heterogeneous geometry has to be accounted for using a MCDancoff Factor approach. Another challenge addressed in this research is to automate modeling the reactivity coefficients over the design space. The reactivity coefficients must be taken into account in order to consider the safety of the design and effectively constrains the design optimization problem.

Development of a neutronics surrogate model is necessary given the long runtimes of neutronics calculations. This is challenging since there is only a small amount

of data to train a model on. Also, the surrogate model must be extremely precise since numbers as small as 10^{-5} are significant for neutronics calculations. This is difficult to achieve with noisy data. This research aims to develop a model that can accurately predict the physics over the design space using machine learning.

Non-convex global optimization requires careful selection of an optimization algorithm and its hyperparameters, which adjust the settings of the algorithm to more efficiently search for the optimum. The surrogate model used for optimization has numerous local minima and is constrained by a complex function. A stochastic method is ideal for such a problem. Also, it is important to capture the region of solutions which are within the error of the optimal solution to give understanding to how sensitive the optima is to the parameters. This can be useful information given that there is a high uncertainty in constraints and costs to manufacture the fuel. Another objective of this research is to use a stochastic machine learning algorithm to optimize the design and characterize the objective function near the optima.

The organization of this dissertation is as follows: first, Chapter 2 covers the methodology for modeling the neutronics of the AHTR. Chapter 3 then continues with a description of the neutronics results and a parametric study of the physics over the design space. The results also include an evaluation of reactivity coefficients constraining the design. After showing an in depth analysis of the neutronics, the statistical methods and methodology for optimization are presented in Chapter 4. Also, the cost modeling methodology is described. The results from the statistical modeling methodology are then analyzed in Chapter 5. Finally the two sides of the research, reactor physics and statistics, are brought together to show a rigorous design optimization approach for the AHTR fuel that safely reduces fuel cycle costs. Figure 6 shows the overall methodology for solving this optimization problem.

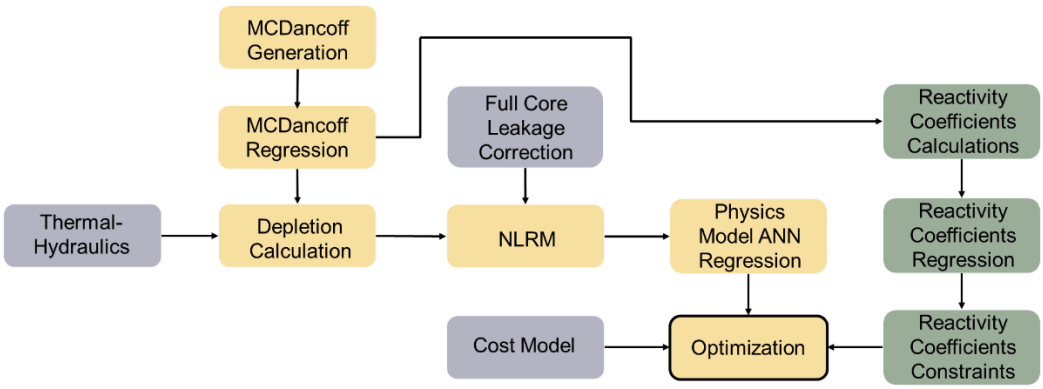

Figure 6. Flowchart of overall neutronics and modeling methodology. Physics surrogate model is generated with Artificial Neural Network (ANN) regression.

CHAPTER 2

NEUTRONICS METHODOLOGY

2.1 Approach to Modeling AHTR Neutronics

The objective of modeling AHTR neutronics for this research is to accurately predict cycle length, burnup, and basic reactivity coefficients over the design space. The AHTR provides many challenges to modeling due to the double heterogeneous geometry and carbon composite materials. Cycle length and burnup are of interest since they directly influence fuel cycle costs. Reactivity coefficients are calculated to ensure the exploration of economic designs is within a stable part of the design space. More in depth safety analysis is beyond the scope of this dissertation. Power peaking factors and xenon power oscillations are among other important design safety considerations. However, detailed full core calculations are currently too computationally expensive for evaluation over the entire design space. Given the much longer diffusion and migration length of graphite moderated reactors, it is expected that xenon power oscillations would not be more of concern compared to LWRs [8]. While inter-assembly peaking factors are relatively high, the peaking factor within a plank is usually less than 1.3. Also, assembly power peaking factors decrease with increasing CHM [11].

Several approximations are necessary due to the extremely long runtimes of CE full core depletion calculations. A fuel assembly can be used to represent the full core, with adequate corrections for the purpose of predicting cycle length and burnup. The methodology involves first calculating average temperatures in the fuel plank and coolant channel. Then resonance self-shielding in taken into account for the double heterogeneous geometry using the MCDancoff Correction over the design space. The fuel

assembly depletion calculations are corrected for full core leakage to reproduce core depletion results. The Non-linear Reactivity Model (NLRM) is used to determine multi-batch fuel cycle length and burnup, as well as fuel discharge burnup. Branch calculations are performed to obtain reactivity coefficients to narrow the design space over parameters that give a stable design. Branch calculations are performed with CE Monte Carlo transport with the main depletion calculation using multigroup (MG) depletion with the MCDancoff Correction. This overall approach of using an assembly model to cover the fuel design space is a practical approach to capture trends in performance and identify regions of viable fuel designs. Figure 7 shows with a flow chart of the neutronics modeling approach employed in this research.

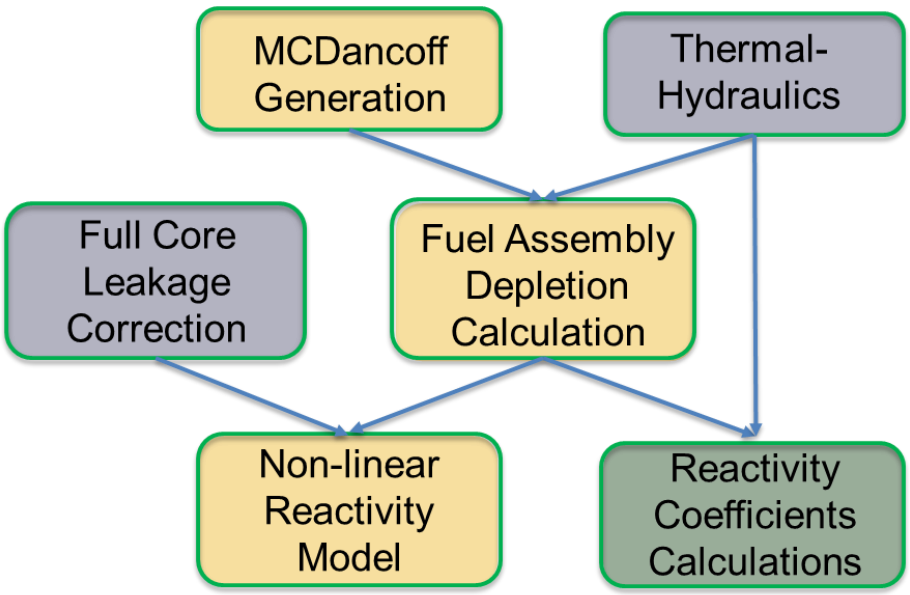

Figure 7. AHTR neutronics methodology. The flow chart shows calculations performed for each design.

2.2 Monte Carlo Transport and Depletion in SCALE

Due to the challenging geometry of the AHTR, it is necessary to use Monte Carlo neutron transport unless tedious homogenization techniques are used. SCALE6.1 was used for the most part of this research, but the first stable release of SCALE6.2 was used to produce the final results. Two code sequences within the SCALE package, CSAS6 and Triton6-depl, are used to evaluate the expected performance of the AHTR. CSAS6 provides the predicted beginning of cycle (BOC) K_{inf} using the KENOVI Monte Carlo Transport code. The Triton6-depl sequence uses KENOVI and Origen to determine K_{inf} at each burnstep over the residence time.

The SCALE model was developed from the 2011 Oak Ridge AHTR base design which has a CHM of ~200 [13]. The model development progressed from an infinite TRISO lattice to a pseudo 1D plank, to an infinite height fuel assembly model, and then to an infinite height full core model. The infinite height fuel assembly model was found to be the most practical model (from the standpoint of adequate accuracy and acceptable computational speed) to use for parametric and optimization studies. The pseudo 1D plank model was found to be inaccurate because it poorly captured the effects of the double heterogeneous geometry. The infinite height fuel assembly model is a sufficient approximation to the 3D full core model since the core is relatively tall. The runtimes of the full core models are impractically long for parametric design studies. Thus, it is an adequate approximation to use a 2D fuel assembly model to do preliminary design optimization to narrow the design space. It is expected that this model will accurately capture trends in the parameters of the design. Studies were performed to find how many axial layers of TRISO particles high the assembly model with reflective boundary conditions should have to minimize excessive reflection on top and bottom model

boundaries. It was found that runtime was minimized with a lattice of 100 TRISO particles axially.

SCALE does not have the option to model randomly distributed TRISO particles. This results in an error of up to approximately 300 pcm. The TRISO particles are instead modeled with a spherical square pitch lattice [27]. It was demonstrated that using a regular lattice for modeling the fuel stripe is valid despite this error [10]. Designs are evaluated between two and nine fuel layers of the TRISO spherical square lattice which varies the thickness of the fuel stripe. Adjusting the pitch of the lattice changes the packing fraction, which is defined as the TRISO volume to fuel stripe volume. CHM is increased or decreased by adjusting the packing fraction and number of fuel layers. Table 2 shows CHM as function of packing fraction (PF) and number of fuel layers (FL).

Table 2. CHM as a function of packing fraction and number of fuel layers.

FL/PF	10.00	12.14	14.29	16.43	18.57	20.71	22.86	25.00	27.14	29.29	31.43	33.57	35.71	37.86	40.00
9	409	360	323	294	271	252	236	222	210	200	191	183	175	169	162
8	461	405	363	331	305	283	265	250	237	225	215	205	197	190	183
7	526	462	415	378	348	324	303	286	271	257	245	235	225	217	209
6	614	540	484	441	406	378	354	333	316	300	286	274	263	253	244
5	737	647	581	529	488	453	425	400	379	360	343	329	315	303	292
4	921	809	726	662	610	567	531	500	473	450	429	411	394	379	366
3	1228	1079	968	882	813	756	708	667	631	600	572	548	526	506	487
2	1842	1619	1452	1323	1219	1134	1062	1000	947	900	859	822	788	758	731

Each Monte Carlo simulation is performed with approximately five to ten million particles total, 200-250 generations, and 60-75 inactive generations depending on whether depletion is being calculated, resulting in the reactivity statistical uncertainty standard deviation in the range approximately from 30 pcm to 45 pcm. The ENDF/B-VII cross-section library was used. The 238 group library is used for MG depletion

calculations in the parametric study. The multi-group approximation is necessary to be able to sufficiently cover the design space due to CE depletion's very long runtime. As an example, it takes about 68 hours to complete a 2D fuel assembly CE depletion calculation, while a MG depletion calculation only takes 10 hours employed on a typical cluster with 32 processors. Currently, there is a newer 252 group library available in SCALE6.2, however the 238 group library is used for this study in order to keep consistency with calculations performed before the release of SCALE6.2. Depletion calculations are run with approximately 25 burnsteps with the first six covering the first two days to capture initial xenon buildup. Figure 8 is an image of the fuel assembly model in SCALE [30]. Table 3 describes the material composition and dimensions used in the 2D fuel assembly model.

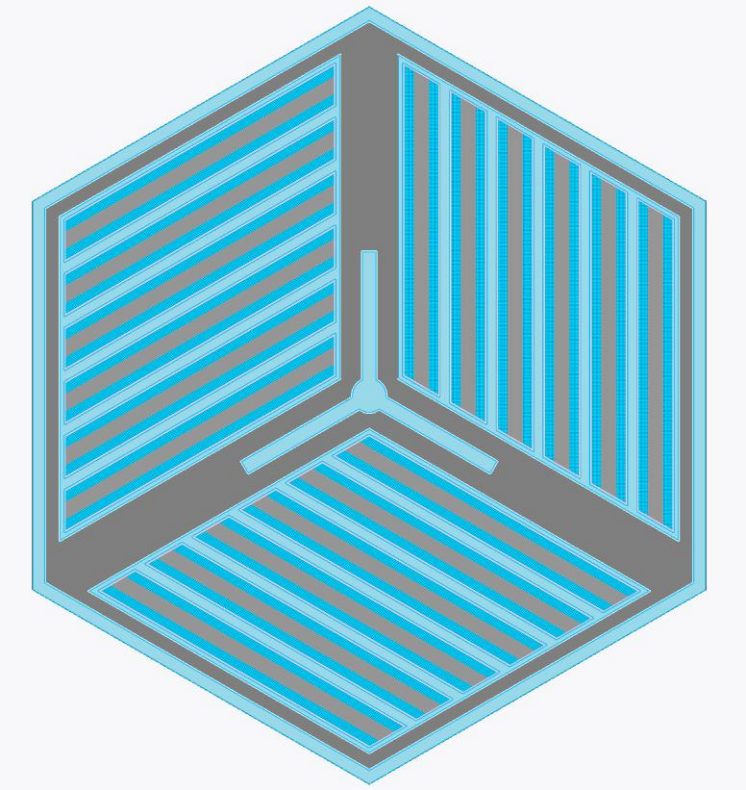

Figure 8. 2D fuel assembly model in SCALE6.2.

Table 3. Materials and density of TRISO particle layers.

Region	Material	Density
Structural Y	Graphite	1.96 g/cc
Coolant Channel	FLiBe	1.99 g/cc
Plank Cladding	Carbon	1.59 g/cc
Central Plank Moderator	Carbon	1.59 g/cc
Matrix	Homogenized Carbon and SiC	1.70 g/cc
Fuel	Uranium Oxycarbide	10.92 g/cc
Control Blade Slot	FLiBe	1.99 g/cc

A study was performed to evaluate whether if homogenization of the fuel planks to reduce runtime without sacrificing significant accuracy is acceptable. The fuel assembly with fully double heterogeneous geometry was compared to two homogenization scenarios. The first simulation homogenized the protective carbon and SiC layers of the TRISO particle with the carbon matrix within the fuel stripe. The second approximation homogenized the UCO fuel kernel with the rest of the TRISO particle and the carbon fuel stripe matrix. Homogenizing the protective layers of the TRISO particle with the carbon matrix has a very small effect on K_{inf} of roughly 22 pcm. This approximation effectively reduced runtime by about 30%, from 1550 minutes down to only 1200 minutes. Homogenizing the fuel kernel results in a large, unacceptable error in K_{inf}, more than 5000 pcm, while providing only a modest reduction in runtime [21].

2.3 1D Single Channel Thermal Hydraulic Model

A single channel thermal hydraulics model was used to provide average fuel, moderator, and coolant temperatures for neutron transport calculations. The model, developed by Pietro Avigni, was developed in MATLAB [2], [3]. It approximates the radial power distribution within the thin fuel stripe to be uniform; a sensitivity study has shown that the impact of this simplification is minimal.

The coolant channel thickness was reduced from 7 mm to 5 mm and the fuel plank thickness increased accordingly in order to increase moderation in the highly undermoderated design. Decreasing the coolant channel thickness slightly has a very small effect on the maximum fuel temperature, only increasing it by 10 K. Figure 9 shows the average temperature of the coolant as the coolant channel thickness and fuel stripe thickness are changed. It can be seen from the figure that the fuel stripe thickness has a much more significant impact on temperature than the coolant channel thickness, except when the channel becomes very thin (below 5mm).

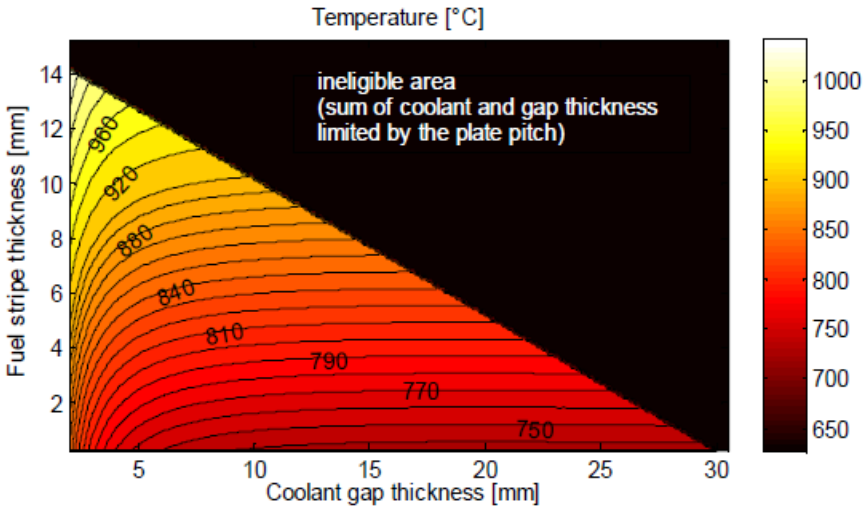

Figure 9. Coolant temperature as a function of fuel stripe thickness and coolant stripe thickness [2].

2.4 Treatment of Resonance Self-Shielding

Due to the very long runtime of CE depletion calculations the Multi-group Approximation is used with the ENDF/B-VII cross-section library collapsed to 238 groups, which provides a speedup factor of about fourteen. The multi-group approximation requires correction for resonance self-shielding effects to accurately predict K_{inf}. SCALE6.1 only has built in functionality to correct for LWR geometries, while SCALE6.2's newer features for double heterogeneity self-shielding calculations

need further testing and debugging. The Centrm module in the CSAS6 and Triton6-depl sequences has an option for a user defined Dancoff Correction which modifies the specified lattice pitch to account for rod shadowing effects: the dan2pitch parameter. Unfortunately, SCALE6.2, the newest version does not have the dan2pitch parameter available in TRITON. Since it was necessary to use SCALE6.2 for its parallel computing capabilities a workaround was found. The dan2pitch option in SCALE6.1 allowed the input of a Dancoff Factor which was used to modify the pitch within the Celldata input block, used for the resonance self-shielding calculations [29]. Instead of using a Dancoff Factor, a Celldata "Pitch Modification Factor" (PMF) is calculated to match multi-group Monte Carlo Transport predicted K_{inf} with continuous energy predicted K_{inf} at BOC. The PMF provides chord length stretching resulting in increased resonance absorption. Using this approach gives the equivalent result to a Dancoff Correction which is described by the following equations:

$$\boldsymbol{I^{NR}} = \int \frac{\boldsymbol{dE}}{\boldsymbol{E}} \frac{\boldsymbol{\sigma_\gamma^F \sigma_p^F}}{\boldsymbol{\sigma_t^F}} + \int \frac{\boldsymbol{dE}}{\boldsymbol{E}} \frac{\boldsymbol{P_{FO}}\left(\boldsymbol{\sigma_t^F - \sigma_p^F}\right)\boldsymbol{\sigma_\gamma^F}}{\boldsymbol{\sigma_t^F}} \tag{2.1}$$

$$\boldsymbol{P_{FO}^*} = \boldsymbol{P_{FO}} \frac{(\mathbf{1}-\boldsymbol{C})}{\mathbf{1}-\boldsymbol{C}(\mathbf{1}-\boldsymbol{\Sigma_t^F}\langle \boldsymbol{R}\rangle_{\boldsymbol{F}}\boldsymbol{P_{FO}})} \tag{2.2}$$

$$\boldsymbol{N_F \sigma_e} = \frac{\mathbf{1}-\boldsymbol{C}}{\langle \boldsymbol{R}\rangle_{\boldsymbol{F}}} \tag{2.3}$$

Where I^{NR} is the narrow resonance approximated resonance integral used in multi-group cross-section calculations. P_{FO} is the probability a neutron born in fuel will escape and make its next collision outside the fuel. C is the Dancoff-Ginsburg factor, and $<R>_F$ is the average chord length of the fuel [8]. Calculating K_{inf} without consideration of rod shadowing effects can result in an error of over 5000 pcm. The approach developed here

for calculating the MCDancoff Factor or PMF is similar to the method used by Kelly and Ilas [16].

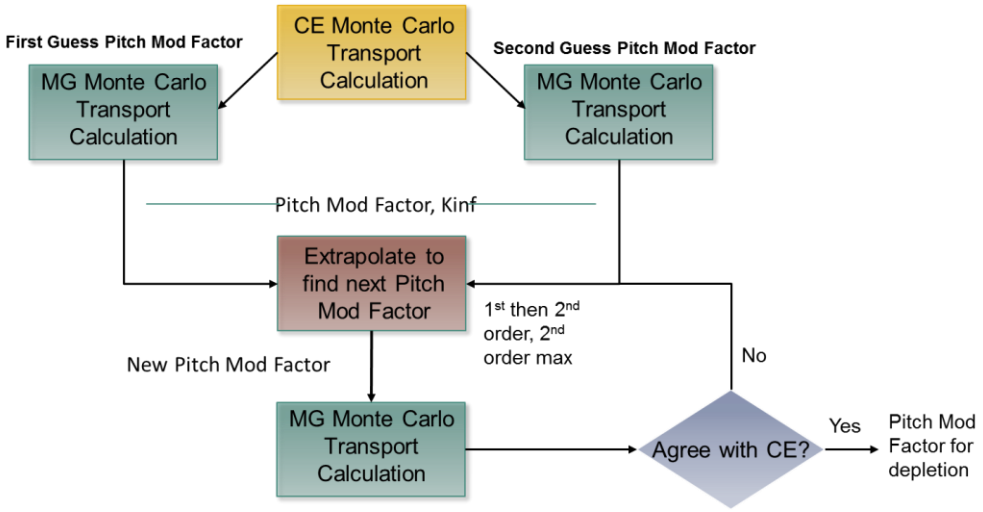

Figure 10. Flow chart describing Pitch Mod Factor generation methodology, solving for PMF that provides MG BOC K_{inf} within ±σ CE K_{inf}.

The PMF is generated at BOC and used at each burnstep over the cycle length. To ensure that the BOC PMF is valid over the whole cycle length MG depletion with a PMF correction is compared to CE depletion performed with SCALE6.2 Beta. SCALE6.2 Beta and SCALE6.1 MG depletion were compared and found to be in agreement. Figure 11 through Figure 14 show ΔK_{inf} between CE and MG depletion and ±2σ uncertainty band of CE depletion for four different designs. Figure 15 shows the same thing but with better statistics for a design with 4 fuel layers, 35% packing fraction, and 9% enrichment. This demonstrates that the BOC generated PMF sufficiently corrects MG depletion to within the statistical uncertainty of CE depletion predicted K_{inf}, comparable to the MCDancoff approach [15]. It can be seen from the figures that there is some small drift over burnup compared to CE depletion. Particularly for the two simulations, having 4 fuel layers, 35% packing fraction, and 9% enrichment, there appears to be a more noticeable drift in ΔK_{inf}.

However, it seems that the resulting error is still acceptable, i.e., comparable to the statistical uncertainty. Out of about 80 burnup steps in Figure 10, Figure 11, Figure 12, and Figure 13, only 3 differences (or ~4%) are clearly outside the ±2σ band, with another about 10 being around ±2σ.

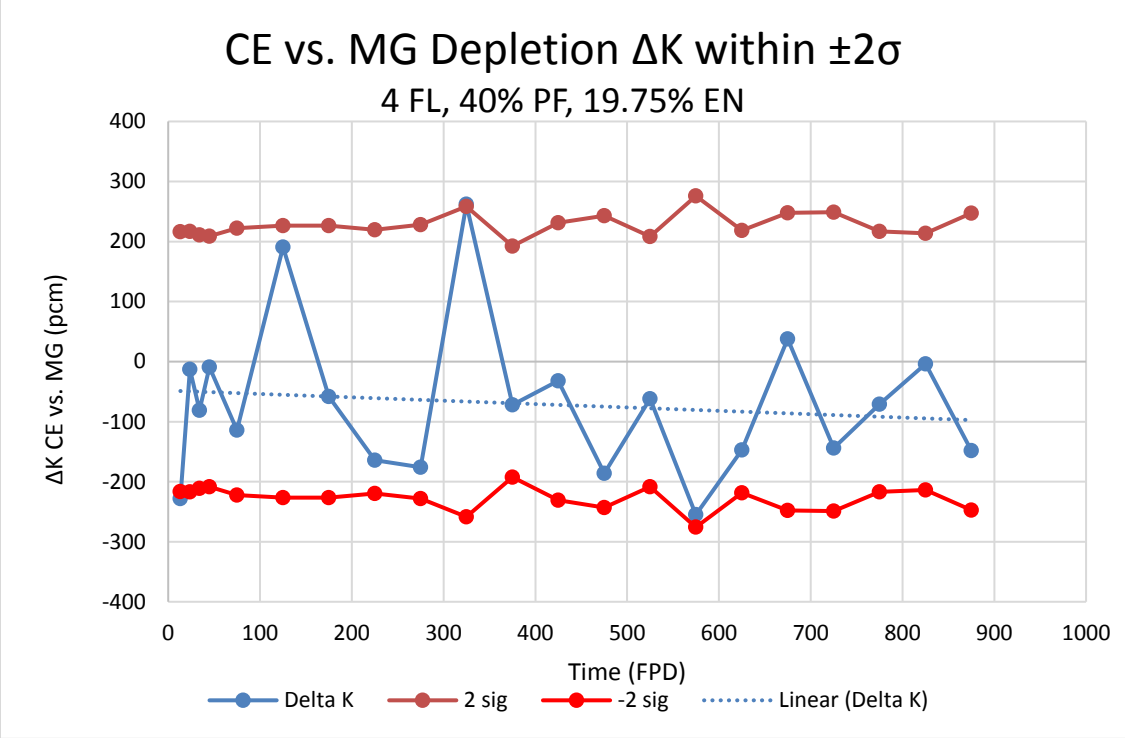

Figure 11. ΔK_{inf} between CE and MG depletion and propagated ±2σ of K_{inf} for 4 FL, 40% PF, and 19.75% EN.

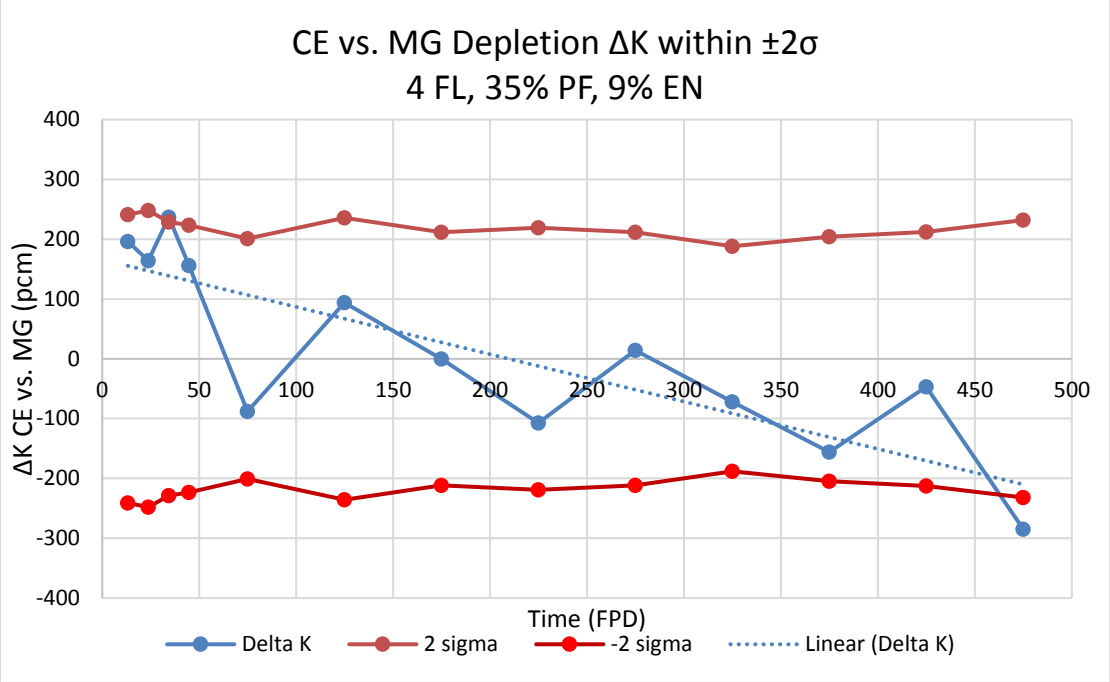

Figure 12. ΔK_{inf} between CE and MG depletion and propagated ±2σ of K_{inf} for 4 FL, 35% PF, and 9% EN.

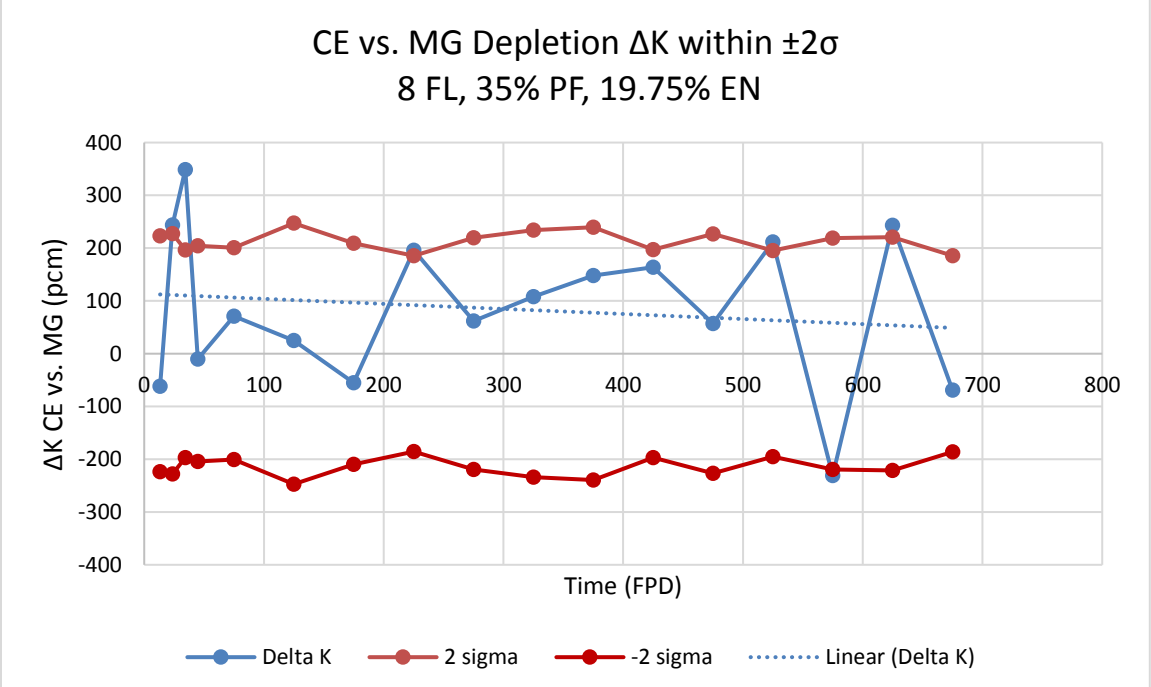

Figure 13. ΔK_{inf} between CE and MG depletion and propagated ±2σ of K_{inf} for 8 FL, 35% PF, and 19.75% EN.

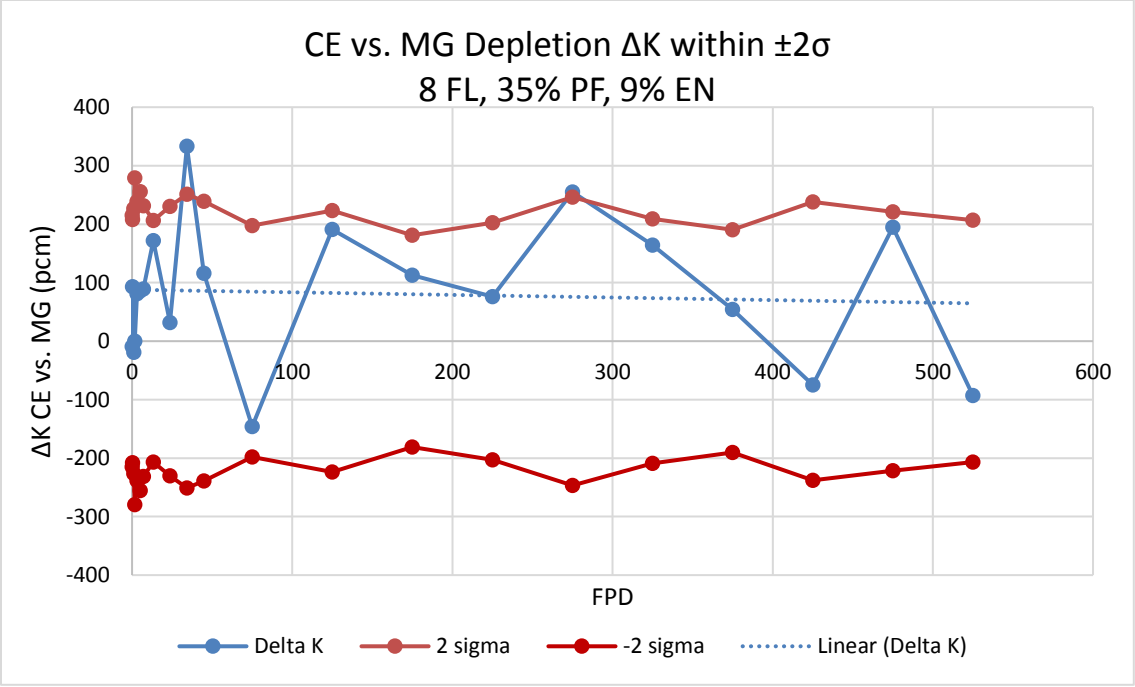

Figure 14. ΔK_{inf} between CE and MG depletion and propagated ±2σ of K_{inf} for 8 FL, 35% PF, and 9% EN.

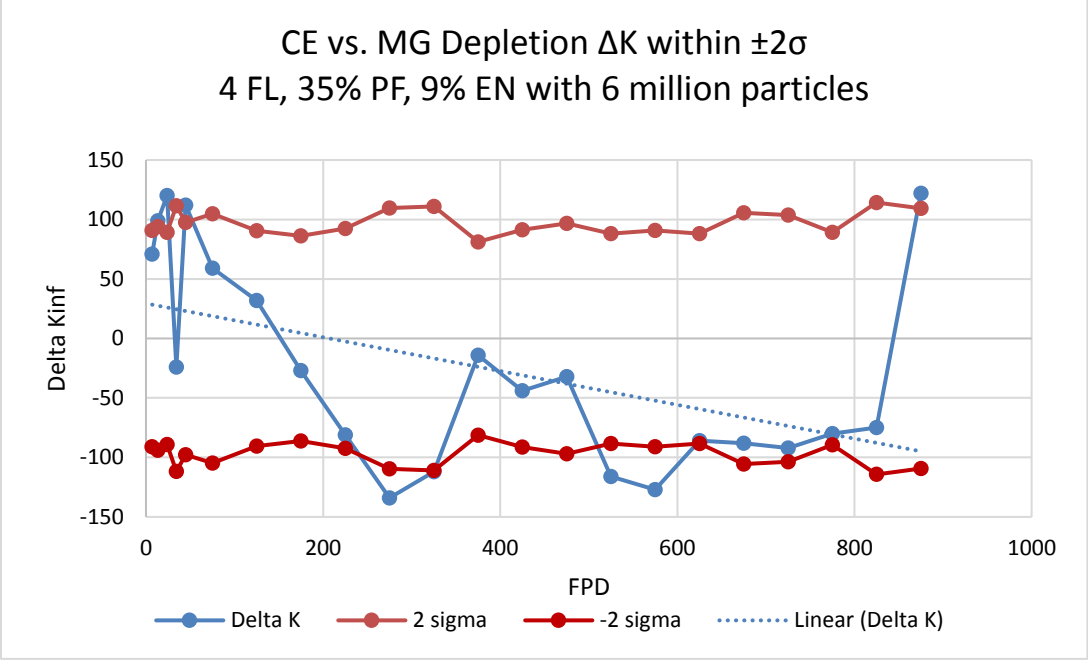

Figure 15. ΔK_{inf} between CE and MG depletion (with reduced statistical uncertainty) and propagated ±2σ of K_{inf} for 4 FL, 35% PF, and 9% EN.

2.5 Non-Linear Reactivity Model for Multi-batch Fuel Cycle

Depletion calculations are performed with the TRITON6-depl sequence in SCALE6.2, which uses the KENO Monte Carlo neutron transport solver in multi-group. Each calculation uses 23 burnsteps with 6 burnsteps in the first 6 days to account for the rapid reactivity drop due to xenon buildup before equilibrium. Figure 16 and Figure 17 show predicted reactivity over the cycle length (expressed in full power days, FPD) for fuel designs with 200 and 400 CHM, respectively, at 19% enrichment. Figure 18 shows predicted reactivity over the cycle length for a fuel design with 400 CHM and 10% enrichment. Each of these figures do not account for the full core leakage correction factor. Depleting the fuel results in a significantly non-linear change in reactivity for 200 CHM fuel. The linear trend-line shows a very poor fit for the change in reactivity over the cycle length. It is especially poor at EOC, which is where the fit is most important since the objective of this approximation is to correct cycle length of a 2D assembly model. The trend line has a standard error of 536 pcm and an EOC ΔK_{inf} of about 1800 pcm, where the standard error is defined as the mean square error of the least squares residuals. The non-linear reactivity behavior, most likely due to undermoderation, results in a slightly harder neutron spectrum which promotes conversion of ^{238}U into ^{239}Pu. At 400 CHM the spectrum is much softer so fission reactions dominates in the fuel and significantly less conversion takes place. It can be seen that a linear trend line better approximates fuel planks with a higher CHM, resulting in standard error of 217 pcm. At 10% enrichment and 400 CHM the behavior is only slightly more linear compared to 19% enrichment and 400 CHM. Decreasing CHM has a much larger effect on non-linear reactivity than enrichment.

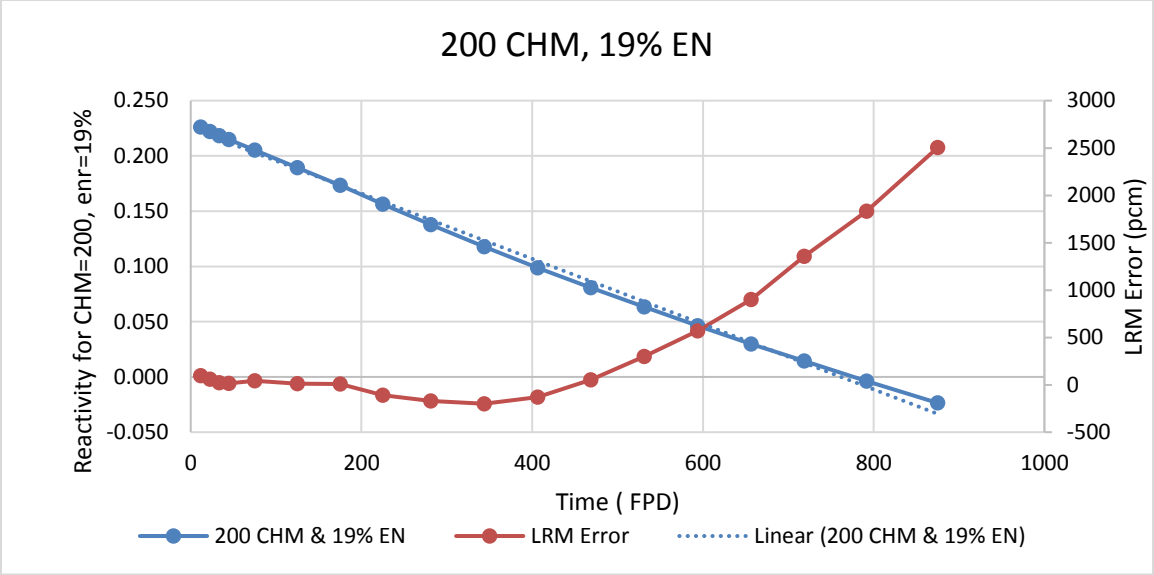

Figure 16. Reactivity as a function of FPD with a linear trend line showing a linear approximation to reactivity for CHM=200 and 19% EN.

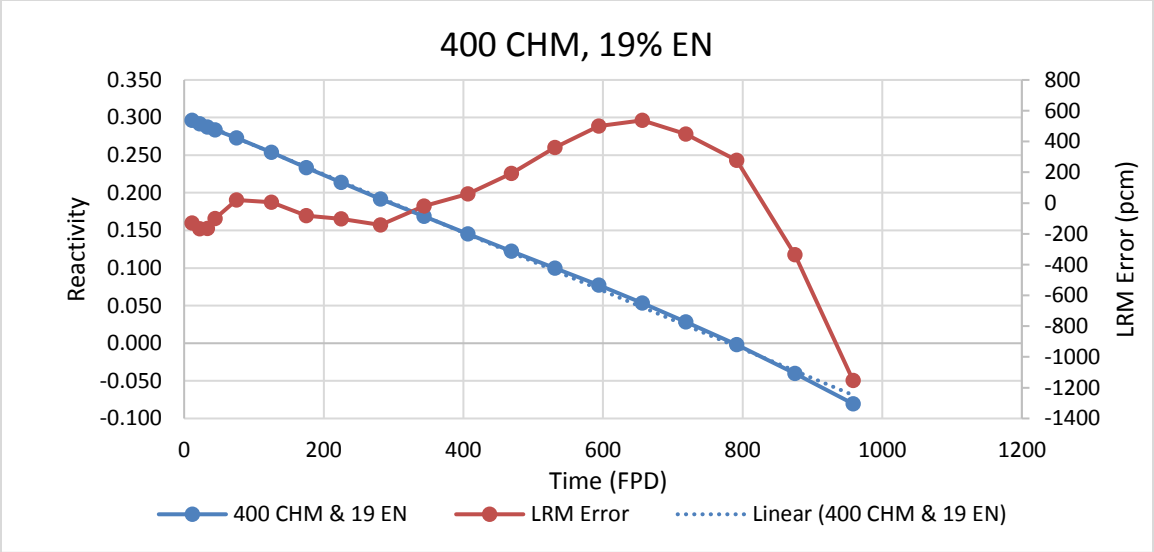

Figure 17. Reactivity as a function of FPD with a linear trend line showing a linear approximation to reactivity for CHM=400 and 19% EN..

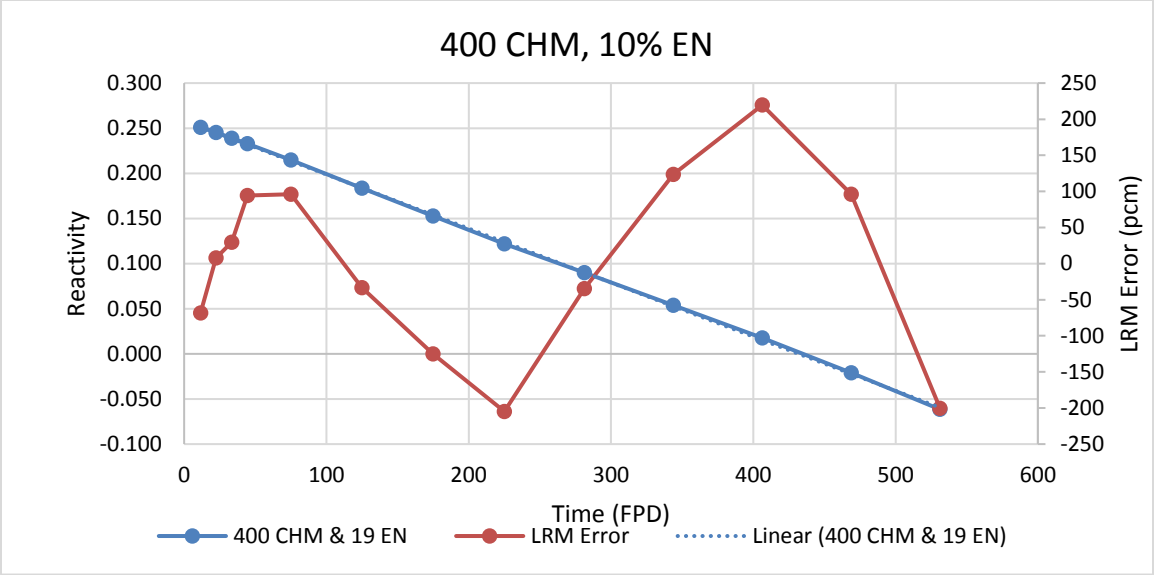

Figure 18. Reactivity as a function of FPD with a linear trend line showing a linear approximation to reactivity for CHM=400 and 9% EN.

In order to compare the NLRM the LRM is used. The LRM has been demonstrated to be accurate and effective for LWR fuel cycle analysis. The LRM simply assumes that reactivity decreases linearly with burnup, that equal-size batches are used (same number of fuel assemblies), and that the reactivity is the average of the batch reactivities. Thus, the equation describing the multi-batch discharge burnup is described by the following formula [7]:

$$\boldsymbol{B_{discharge}} = \frac{2n}{2n+1}\frac{2n}{n+1} \cdot \boldsymbol{B_1} \quad \textbf{(2.4)}$$

$$\boldsymbol{B_{cycle}} = \frac{2}{n+1} \cdot \boldsymbol{B_1} \quad \textbf{(2.5)}$$

Where n is the number of batches and B is burnup, thus B_1 represents straight burn, i.e., single batch.

Due to the non-linear reactivity over the cycle length the Linear Reactivity Approximation is inaccurate in predicting cycle length of multi-batch fuel cycles for a significant portion of the design space. A simple Non-linear Reactivity Model has been

found to be more accurate in predicting multi-batch cycle lengths over the whole design space. The following equations are used to calculate the NLRM [5]:

$$\boldsymbol{\rho(b) = y^0 + y^1 b + .. + y^{(m)} b^m}$$

$$\rho_{EOEC} = \frac{1}{n}\sum_{i=1}^{n} \rho(b_i^{EOEC})\boldsymbol{\rho_{EOEC}} = \boldsymbol{\frac{1}{n}\sum_{i=1}^{n} \rho(b_i^{EOEC})}$$

$$\rho_{EOEC} = \frac{1}{n}\sum_{i=1}^{n} \rho(\frac{ib_i^{EOEC}}{n})\boldsymbol{\rho_{EOEC}} = \boldsymbol{\frac{1}{n}\sum_{i=1}^{n} \rho(\frac{ib_i^{EOEC}}{n})}$$

$$\rho_{EOEC} = \frac{1}{n}\sum_{i=1}^{n} y^0 + \frac{y^1 i b_{discharge}}{n^2} + \cdots + y^{(m)}\left(\frac{ib_{discharge}}{n}\right)^m \boldsymbol{\rho_{EOEC}}$$

$$= \boldsymbol{\frac{1}{n}\sum_{i=1}^{n} y^0 + \frac{y^1 i b_{discharge}}{n^2} + \cdots + y^{(m)}\left(\frac{ib_{discharge}}{n}\right)^m}$$

$$\rho_{EOEC} = y^0 + \frac{y^1 b_{discharge}}{n^2}\sum_{i=1}^{n} i + \cdots + \frac{y^{(m)} b_{discharge}^m}{n^{m+1}}\sum_{i=1}^{n} i^m \boldsymbol{\rho_{EOEC}}$$

$$= \boldsymbol{y^0 + \frac{y^1 b_{discharge}}{n^2}\sum_{i=1}^{n} i + \cdots + \frac{y^{(m)} b_{discharge}^m}{n^{m+1}}\sum_{i=1}^{n} i^m}$$

$$\boldsymbol{0 = y^0 + \frac{y^1 b_{max}}{n^2}\sum_{i=1}^{n} i + \cdots + \frac{y^{(m)} b_{max}^m}{n^{m+1}}\sum_{i=1}^{n} i^m} \qquad \textbf{(2.6)}$$

Where y values are coefficients of the polynomial fit, b is burnup, n is number of batches, and m is the order of the polynomial. This model averages the reactivity of the assemblies burned n times given by the polynomial fit, and the solution to the last equation (when reactivity is zero) provides an estimate of the discharge burnup.

As number of the number batches increases the residence time of the fuel increases. The increase in the difference in residence time diminishes as the number of batches increases further. Figure 19 shows fuel residence time and the difference in residence time as number of batches increase for the NLRM and LRM. The results show that the LRM gives an error in predicted cycle length greater than the 2σ of the simulations, where the standard error is approximately 4 days. The difference between

the models increases as the number of batches increases. It is apparent that the LRM consistently underestimates cycle length compared to the NLRM.

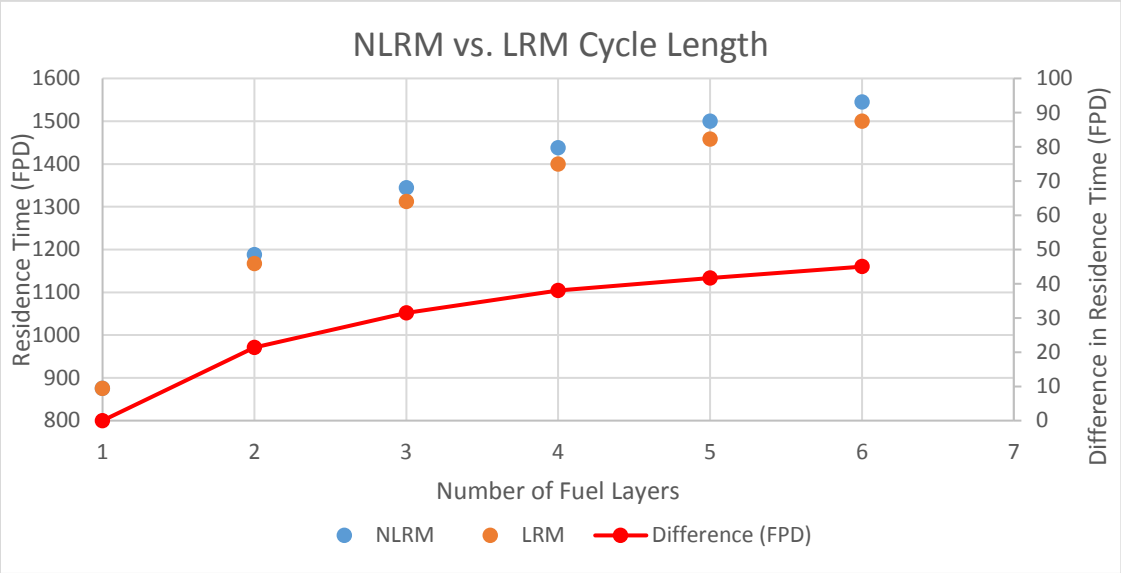

Figure 19. Plot shows a comparison between the NLRM and the LRM cycle length (left axis) and the difference in predicted residence time between the models (right axis).

2.6 Full Core Leakage Factor Approximation

A correction factor is calculated in order to improve the accuracy of using a 2D assembly model to evaluate cycle length. Previous work was done to compare the 3D full core model to the 2D assembly model [21], [22]. The full core depletion calculations were performed over several different packing fractions and enrichments. A leakage correction factor was calculated by comparing the K_{eff} of the full core calculations at EOC (which is unity) with the K_{inf} of the assembly model at the same burnup. The full core model depletion was performed as a single zone for consistency with the assembly model.

Table 4. ΔK_{inf} between 3D full core model and 2D fuel assembly model at EOC for different fuel designs.

EOC ΔK Full Core vs. 2D Fuel Assembly				
PF\EN	**5%**	**10%**	**15%**	**19.75%**
20%	1523	1018	774	531
30%	973	423	113	-99
40%	651	17	-253	-522

The model was further expanded by extrapolating the results treating a change in packing fraction as a change in CHM allowing the model consider an additional dimension, number of fuel layers. Figure 20, Figure 21, and Figure 22 show how the extrapolated model approximates the full core leakage for the assembly model of three different designs. The expanded model was generated with multiple polynomial regression. Table 5 shows the results from several cases predicted by the model to provide cross-validation. The model shows very good agreement and it is clear that it can adequately approximate the leakage effect to correct the 2D fuel assembly model's predicted cycle length.

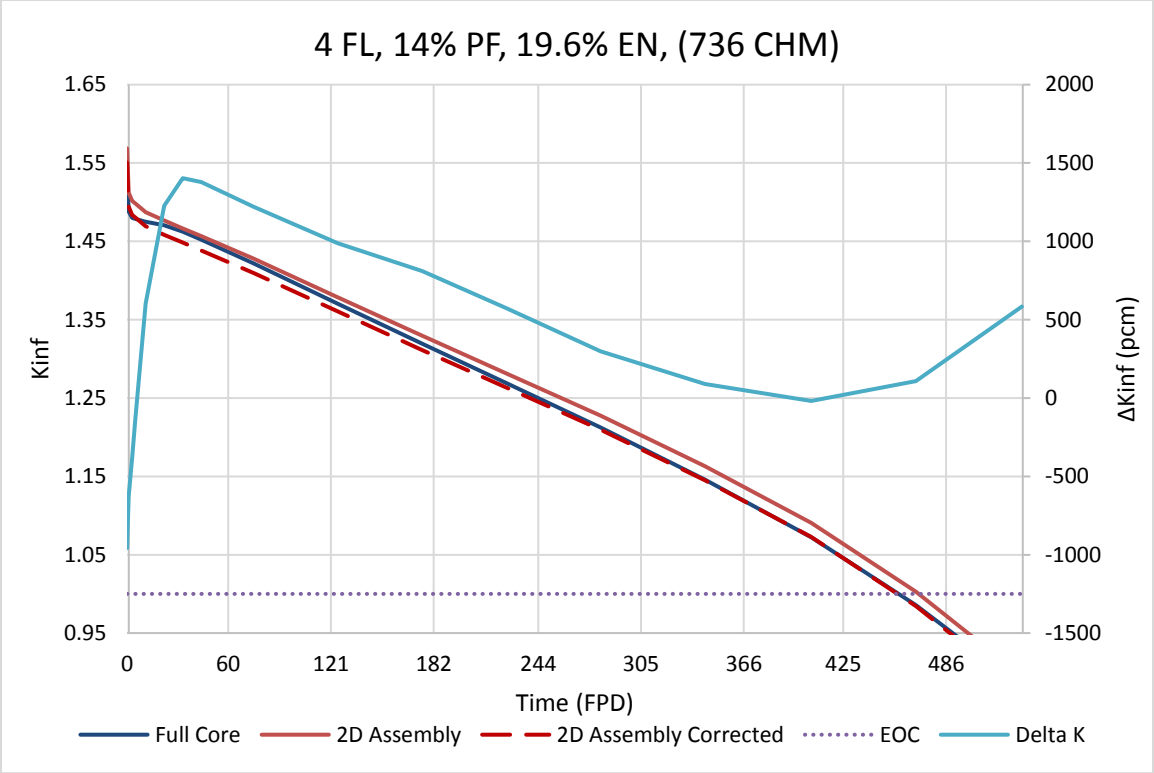

Figure 20. Effect of full core leakage correction factor on ΔK_{inf} for 4 FL, 14% PF, and 19.6% EN.

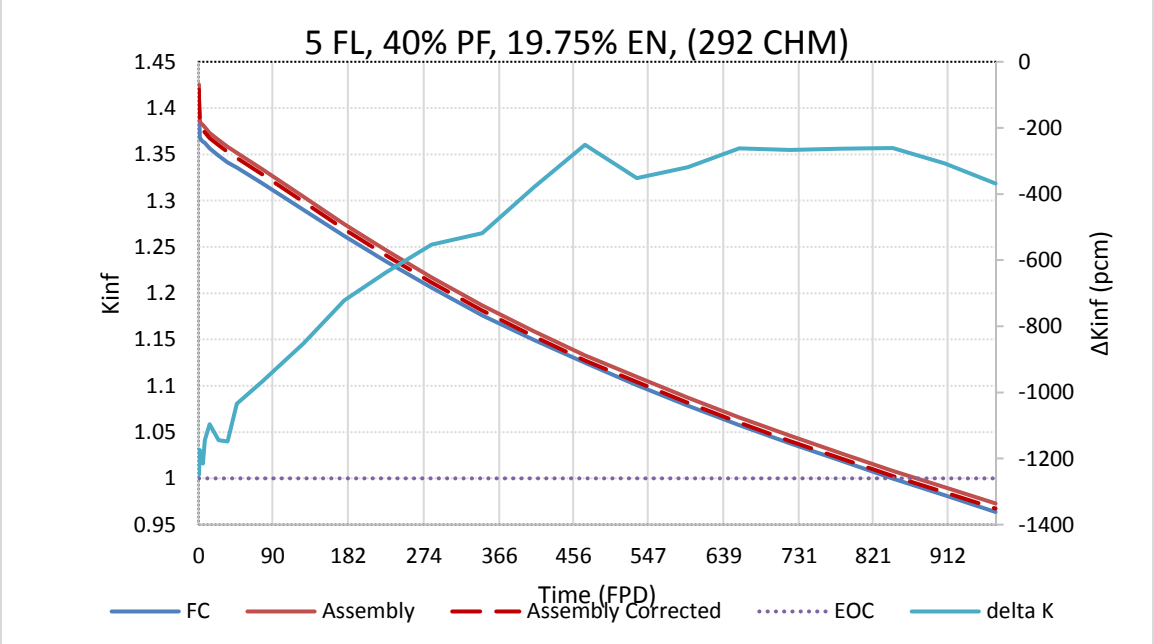

Figure 21. Effect of full core leakage correction factor on ΔK_{inf} for 5 FL, 40% PF, and 19.75% EN.

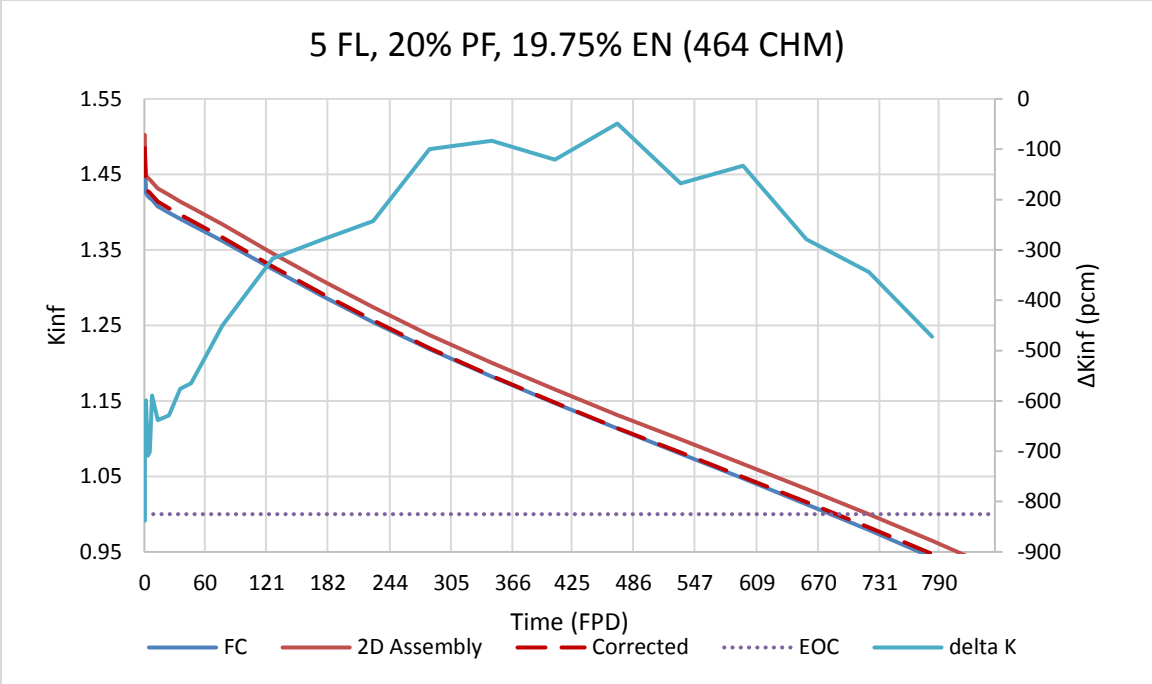

Figure 22. Effect of full core leakage correction factor on ΔK_{inf} for 5 FL, 20% PF, and 19.75% EN.

Table 5. Cross-validation cases for the full core leakage correction model.

Cross Validation						
FL	PF	EN	CHM	ΔK with Full Core (before correction)	EOC K_{inf} Fit Error	CL error
4	14	19.6	736	1170	-19	2 days
5	40	19.75	292	820	250	6 days
5	20	19.75	464	2050	300	9 days

2.7 Calculating Reactivity Coefficients for Optimization Constraints

It is of great importance to consider safety constraints on the fuel design optimum search. If the most seemingly economic design is unstable, it will not be acceptable. Reactivity temperature and power coefficients are calculated at BOC, MOC, and EOC to provide some very basic constraints on optimization. The coefficients are calculated at three temperature levels to provide data for a quadratic fit. The fuel temperature coefficient, moderator temperature coefficient, and coolant temperature coefficients are

calculated at 1300 K, 1000 K, and 750 K. The coolant temperature coefficient also takes changes in density due to temperature into account with the following equation [4]:

$$\boldsymbol{\rho}\left(\frac{\boldsymbol{g}}{\boldsymbol{cm^3}}\right) = \mathbf{2413.03} - \mathbf{.4884} \times \boldsymbol{T}(\boldsymbol{K}) \tag{2.7}$$

Since the moderator materials, which include graphite and carbonaceous materials, have low coefficients of thermal expansion the density is left constant for the branch cases. The coefficient of thermal expansion for isotropic nuclear grade graphite is less than $5x10^{-6}$ K^{-1} [24]. The average fuel stripe temperature is used for calculating the fuel temperature coefficient since the flux gradient is small across the fuel strip and TRISO fuel particles.

The void reactivity coefficient is calculated by reducing the coolant density by a fraction at constant temperature. The coolant void coefficient is calculated with all materials held constant at 1000 K and coolant density reduced to 80%, 40%, and 20% of normal average coolant density. Since the reactor does not operate anywhere near the boiling point of FLiBe, the void coefficient in this study is not referring to boiling in the coolant, but is more of a conservative hypothetical consideration of how blockages in the flow channel or a loss of coolant accident (LOCA) might affect reactivity. Such an event could occur if one or more of the fuel planks has a structural failure and blocks the flow.

Calculating power coefficient of reactivity requires contributing coefficients of reactivity and partial derivatives of material temperatures with respect to power. A single channel thermal hydraulic model provides the average material temperatures as a function of power. The temperature reactivity coefficients are calculated by the previous branch calculations. The temperatures are calculated for a change in power from zero

power up to 150% power. The following equation is used to calculate the power reactivity coefficient from temperature coefficients:

$$\boldsymbol{\alpha_P = \frac{d\rho}{dP} = \sum_j \left(\frac{\partial \rho}{\partial T_j}\right)\left(\frac{\partial T_j}{\partial P}\right) = \sum_j \alpha_T^j \left(\frac{\partial T_j}{\partial P}\right)} \quad (2.8)$$

Where α_T^j is temperature reactivity coefficient of material j and $\frac{\partial T_j}{\partial P}$ is the derivative of the temperature of material j with respect to power calculated from the 1D single channel thermal hydraulics model. The power reactivity coefficient requires a thermal hydraulics model that relates appropriate average temperatures of the compositions as the power is increased.

The reactivity coefficients are calculated in several steps over the whole design space. Figure 23 is a diagram showing what part of the cycle length the reactivity coefficients are calculated. First a multi-group depletion calculation is performed with fine burnsteps. Then, each branch calculation takes the isotopics from the BOC, MOC, and EOC to perform the branch calculations at three levels at each of the three burnsteps. A quadratic fit is then used to calculate the reactivity coefficients over the range of interest. The maximum value of each reactivity coefficient is used for calculating the power reactivity coefficient or void coefficient. This approach is quite conservative, but turns out not to be too limiting.

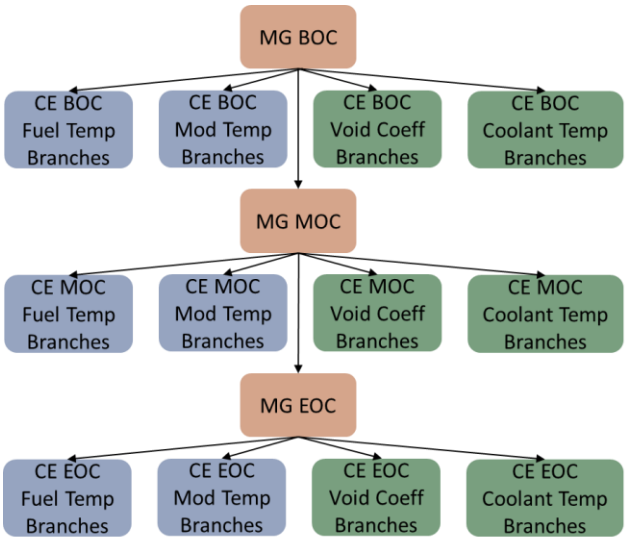

Figure 23. Flowchart of branch cases at BOC, MOC, and EOC.

CHAPTER 3

AHTR NEUTRONIC RESULTS

3.1 Neutronics Results

The results in this chapter describe the neutronics performance of the AHTR plank fuel over the design space. The design space is considered to be between two and nine fuel layers, 10%-40% packing fraction, and 5%-19.75% enrichment. The multi-batch fuel analysis considers single batch to six batch fuel cycles. First, the calculations to account for resonance self-shielding are analyzed and tabulated. Pitch Mod Factors are calculated over the design space. Then, a depletion parametric study is performed using PM factors predicted from a surrogate model. Finally, the reactivity coefficient results are analyzed to show where the design space is stable (i.e., acceptable) and where a realistic optimum can be realized. In each section the full results are tabulated and a fit over the design space is shown.

3.2 Resonance Self-shielding Results

In order to allow for the multi-group approximation to be used, Pitch Mod Factors are calculated over the design space. Periodic Latin Hypercube Sampling (LHS) is used to generate the designs the PM factors are solved for. Periodic LHS provides good coverage of the design space for a surrogate model reducing the number of required simulations [32]. Table 6 lists all of the Latin Hypercube sampled runs for calculating the Pitch Mod Factors. The PMF increases as CHM increases. Figure 24 shows the PMF as a function of packing fraction and number of fuel layers, with enrichment held constant at

19.75%. The Artificial Neural Network regression model shows a drastic change in slope near the highest CHM designs. This is likely due to statistical error in the transport calculations and low resolution in that area. This leads to an error of approximately 200 pcm in K_{inf} due to the fit error.

Table 6. Resulting Pitch Mod Factor calculations.

FL	PF	EN	PM	FL	PF	EN	PM	FL	PF	EN	PM
2	10.6	10.4	1.60727	5	38.8	8.9	1.41792	8	22.6	17.9	1.19461
2	24.4	15.2	1.78227	5	22	13.7	1.35169	8	36.4	7.4	1.24259
2	38.2	20	1.8934	5	35.8	18.5	1.4083	8	19.6	12.2	1.17309
2	21.4	9.5	1.74664	6	19	8	1.27291	8	33.4	17	1.23528
3	35.2	14.3	1.63542	6	32.8	12.8	1.31499	9	16.6	6.5	1.11729
3	18.4	19.1	1.5	6	16	17.6	1.25863	9	30.4	11.3	1.1759
3	32.2	8.6	1.60522	6	29.8	7.1	1.31624	9	13.6	16.1	1.09913
3	15.4	13.4	1.5193	6	13	11.9	1.23125	9	27.4	5.6	1.16174
3	29.2	18.2	1.61748	6	26.8	16.7	1.31008	9	40	20	1.21626
3	12.4	7.7	1.5	6	10	6.2	1.18936	2	40	20	1.91535
3	26.2	12.5	1.55741	6	23.8	11	1.28937	2	10	5	1.56949
4	40	17.3	1.53367	7	37.6	15.8	1.2872	9	40	5	1.21175
4	23.2	6.8	1.44533	7	20.8	5.3	1.2246	2	40	5	1.88152
4	37	11.6	1.5	7	34.6	10.1	1.27196	6	25	20	1.31032
4	20.2	16.4	1.44217	7	17.8	14.9	1.2	6	40	12.5	1.34295
4	34	5.9	1.47703	7	31.6	19.7	1.27586	9	25	12.5	1.16291
4	17.2	10.7	1.40811	7	14.8	9.2	1.18962	6	25	5	1.28898
4	31	15.5	1.4808	7	28.6	14	1.26242	2	25	12.5	1.83759
5	14.2	5	1.29985	8	11.8	18.8	1.13577	6	10	12.5	1.2
5	28	9.8	1.378	8	25.6	8.3	1.2	2	10	20	1.60162
5	11.2	14.6	1.3076	8	39.4	13.1	1.24752	2	10	19.75	1.629

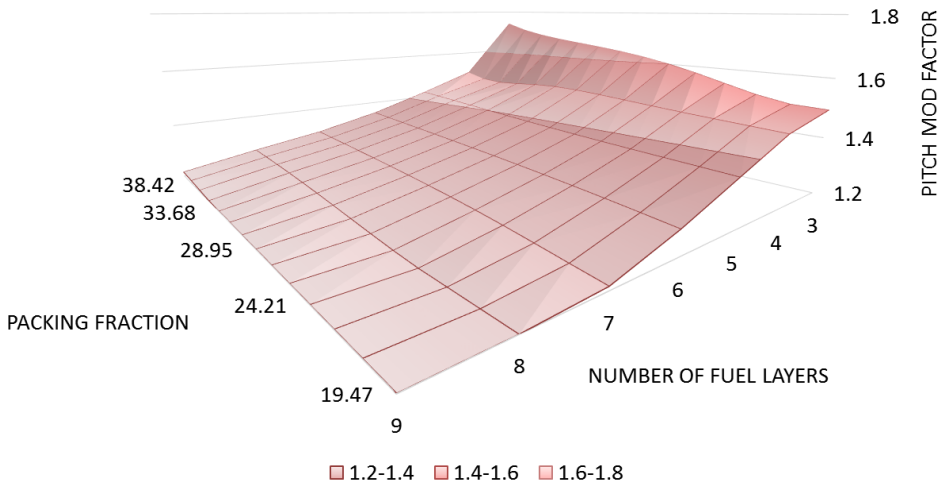

Figure 24. Pitch Mod Factor ANN regression with enrichment held constant at 19.75%.

3.3 Depletion and Non-Linear Reactivity Model

Depletion calculations are performed with the TRITON6-depl sequence in SCALE6.2 with the KENO Monte Carlo neutron transport solver in multi-group. Each calculation has a total of 23 burnsteps, with 3 burnsteps in the first 6 days to account for the rapid reactivity drop due to xenon buildup before equilibrium. The designs selected for depletion are sampled with LHS and supplemented with additional runs near the edge of the design space. Table 7 shows the resulting cycle length and burnup predicted by Triton MG depletion. Figure 25 shows a surface plot of the one batch burnup and cycle length as a function of packing fraction and number of fuel layers, with enrichment held constant at 19.75%.

Table 7. Depletion calculation results for parametric study.

FL	PF	EN	CL	BU	FL	PF	EN	CL	BU	FL	PF	EN	CL	BU
2	32	16.6	308	120593	5	22	11.6	406	81623	7	20.4	7.2	241	36393
3	36	12.6	393	94830	5	26	7.6	262	47119	7	25.2	5.4	156	20461
3	40	8.6	269	60503	5	13.2	17.4	460	130010	7	12	6.6	169	36351
3	27.6	12	306	88146	5	13.6	11	277	76740	8	32.8	18.8	781	75201
3	22.8	13.8	309	101103	6	38.4	19.2	833	96277	8	24.4	18.2	735	86202
3	18.8	17.8	352	130986	6	30	18.6	781	106414	8	33.2	12.4	455	43455
3	23.2	7.4	139	44952	6	34	14.6	610	76457	8	28.4	14.2	547	57975
4	35.6	19	740	134934	6	25.6	14	561	84958	8	37.2	8.4	256	22663
4	39.6	15	611	103771	6	16.8	19.8	699	140187	8	16	17.6	673	104573
4	31.2	14.4	528	105122	6	29.6	10	392	53885	8	20	13.6	519	69493
4	35.2	10.4	392	72011	6	17.2	13.4	472	93180	8	28.8	7.8	246	25829
4	26.8	9.8	315	69399	6	21.2	9.4	340	58384	8	11.2	19.4	670	132056
4	18	15.6	407	116927	6	12.4	15.2	452	110985	8	11.6	13	441	84903
4	14	19.6	429	145735	6	12.8	8.8	238	57210	8	15.6	9	309	48825
4	30.8	5.8	169	33934	7	37.6	17	714	71732	9	36.8	14.8	537	42565
5	34.8	16.8	708	104853	7	29.2	16.4	675	80263	9	19.6	20	793	95671
5	38.8	12.8	541	74511	7	38	10.6	393	39202	9	32.4	10.2	320	27611
5	26.4	16.2	629	111989	7	20.8	15.8	622	92729	9	24	9.6	316	33304
5	21.6	18	643	130872	7	24.8	11.8	457	60589	9	15.2	15.4	579	82750
5	30.4	12.2	488	79082	7	33.6	6	178	19272	9	28	5.6	122	11602
5	39.2	6.4	233	31869	7	16.4	11.2	404	70565					

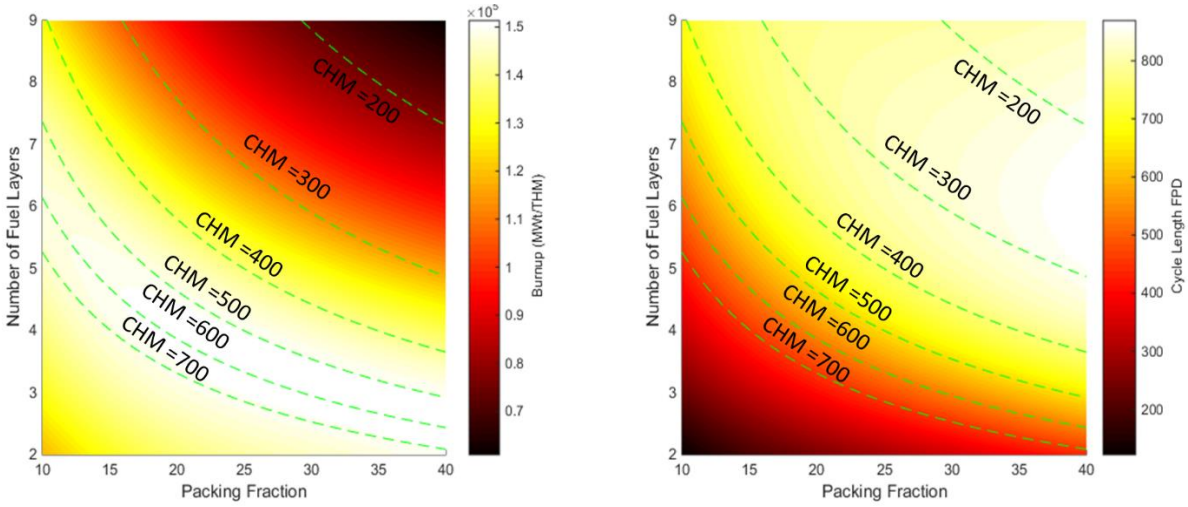

Figure 25. Plot on the left shows discharge burnup (MWd/tHM) as function of packing fraction and number of fuel layers. The plot on the right shows cycle length (FPD) as a function of the same variables. Both plots show iso-CHM lines. Enrichment is held constant at 19.75%.

Table 8. Burnup and cycle length of selected cases in the design space.

Cycle Length and Burnup of Selected Cases				
PF	35	35	35	35
FL	4	4	8	8
CHM	400	400	200	200
Enrichment	19.75	9	19.75	9
Cycle Length (FPD)	828	431.9	798	296.7
Burnup (GWd/tHM)	152.9	75.67	73.6	27.4

It appears from the results that for the same CHM there is some secondary spectral effect that improves cycle length when an equivalent amount of fuel is packed more tightly. When the fuel is spread further apart within the fuel plank there is more opportunity for neutron collisions with carbon slowing the neutron into the resonance region. In the resonance region the capture cross-section for ^{235}U dominates. When the fuel is packed more closely neutrons are more likely to interact directly with the fuel before leaving the fuel stripe. In the fast flux region, the elastic scattering cross-section dominates for ^{235}U. Also, when the fuel is tightly packed neutrons must travel farther through the moderator to reach the next fuel stripe, further softening the spectrum. The fission cross-section is dominant for ^{235}U in the thermal region of the spectrum. More tightly packed fuel is better utilized due to a secondary spectral effect that depends on geometry. Figure 26 shows dominant ^{235}U cross-sections as a function of energy.

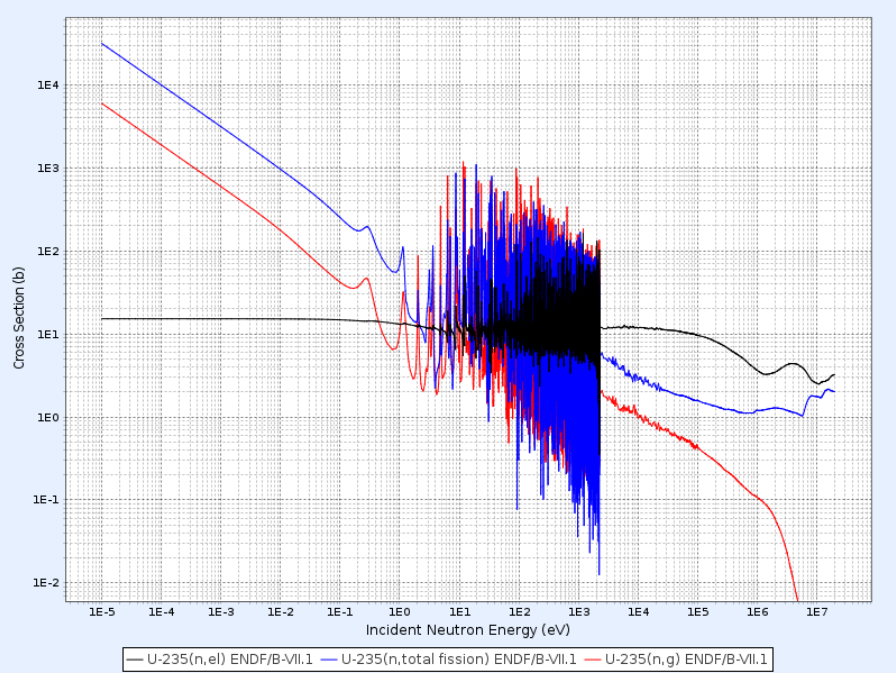

Figure 26. Plot of dominant ^{235}U cross-sections. Blue line is fission cross-section, red line is (n,γ) cross-section, and black line is elastic scattering cross-section.

Parametric studies were also performed to see the effect of changing parameters on multi-batch refueling performance. Figure 27 shows cycle length as a function of the number of batches and packing fraction. The figure shows that as CHM decreases the cycle length increases. At lower packing fractions multi-batch the difference in cycle length is lower, but this in fact may be more significant.

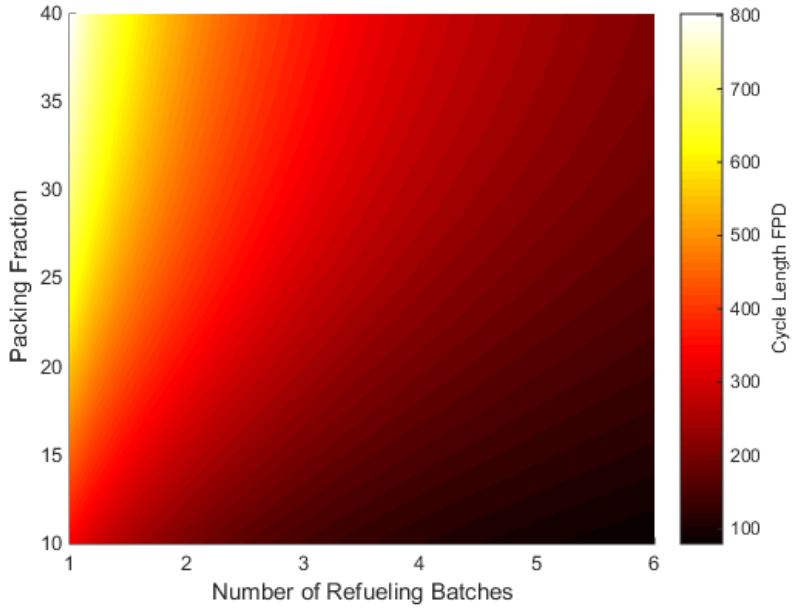

Figure 27. Cycle length (FPD) as a function of packing fraction and number of batches. Enrichment is held constant at 19.75%.

3.4 Reactivity Coefficients

The reactivity coefficients generally trend towards more negative as CHM is decreased. The void coefficient closely follows along iso-CHM lines while the power reactivity coefficient is more sensative to the fuel stripe thickness than packing fraction, but trends more positive with increasing CHM. Table 9 shows the results of the power coefficient calculations in SCALE. Table 10 shows the void coefficient results from SCALE. Figure 28 shows the void coefficient calculated with enrichment held constant at 19.75% and Figure 29 shows the void coefficient at 9% enrichment. Figure 30 and Figure 31 show the standard deviation of the void coefficient with enrichment held constant at 19.75% and 9%. The standard deviation is calculated using an ensemble of neural networks that fit the void coefficient data over the design space. The results show that decreasing the enrichment from 19.75% to 9% significantly shifts the void coefficient

more positive. This is expected since as the resonance absorption in the fuel increases due to higher ^{238}U content the spectrum is softened, increasing the effect of absorption in FLiBe. In both cases the void coefficient increases with increasing CHM. This is consistent with results that were predicted at Berkeley for the PB-AHTR [9]. The design becomes overmoderated beyond 400 CHM for the 19.75% enrichment case and about 240 CHM for the 9% enrichment case.

Table 9. Power reactivity coefficient results from SCALE6.2

FL	PF	EN	PW	BOC_P	MOC_P	EOC_P	FL	PF	EN	PW	BOC_P	MOC_P	EOC_P
2	11.25	11.25	0	-1.72E-05	-1.79E-05	-1.67E-05	2	11.25	11.25	100	-1.60E-05	-1.61E-05	-1.54E-05
2	25	16.25	0	-1.78E-05	-1.76E-05	-2.09E-05	2	25	16.25	100	-1.66E-05	-1.71E-05	-1.97E-05
3	38.75	5.625	0	-4.17E-05	-4.23E-05	-5.16E-05	3	38.75	5.625	100	-3.86E-05	-3.99E-05	-4.82E-05
3	21.25	10.625	0	-2.75E-05	-2.78E-05	-3.33E-05	3	21.25	10.625	100	-2.50E-05	-2.56E-05	-3.05E-05
3	35	15.625	0	-2.79E-05	-3.13E-05	-4.09E-05	3	35	15.625	100	-2.60E-05	-2.92E-05	-3.82E-05
3	17.5	5	0	-3.59E-05	-3.59E-05	-3.72E-05	3	17.5	5	100	-3.24E-05	-3.30E-05	-3.43E-05
4	31.25	10	0	-3.95E-05	-4.19E-05	-5.49E-05	4	31.25	10	100	-3.65E-05	-3.88E-05	-5.19E-05
4	13.75	15	0	-2.80E-05	-2.87E-05	-3.66E-05	4	13.75	15	100	-2.51E-05	-2.63E-05	-3.36E-05
4	27.5	20	0	-2.86E-05	-3.46E-05	-4.54E-05	4	27.5	20	100	-2.72E-05	-3.29E-05	-4.33E-05
5	10	9.375	0	-3.66E-05	-3.75E-05	-4.45E-05	5	10	9.375	100	-3.36E-05	-3.47E-05	-4.10E-05
5	23.75	14.375	0	-3.92E-05	-4.40E-05	-5.64E-05	5	23.75	14.375	100	-3.72E-05	-4.20E-05	-5.46E-05
5	37.5	19.375	0	-4.03E-05	-4.80E-05	-6.05E-05	5	37.5	19.375	100	-3.79E-05	-4.55E-05	-5.86E-05
6	20	8.75	0	-5.26E-05	-5.59E-05	-7.15E-05	6	20	8.75	100	-4.92E-05	-5.20E-05	-6.68E-05
6	33.75	13.75	0	-5.20E-05	-6.04E-05	-7.52E-05	6	33.75	13.75	100	-4.97E-05	-5.67E-05	-7.29E-05
6	16.25	18.75	0	-3.71E-05	-4.40E-05	-5.77E-05	6	16.25	18.75	100	-3.49E-05	-4.08E-05	-5.46E-05
6	30	8.125	0	-5.87E-05	-6.09E-05	-7.65E-05	6	30	8.125	100	-5.54E-05	-5.75E-05	-7.28E-05
7	12.5	13.125	0	-4.64E-05	-5.27E-05	-6.74E-05	7	12.5	13.125	100	-4.42E-05	-4.83E-05	-6.16E-05
7	26.25	18.125	0	-5.29E-05	-6.07E-05	-7.55E-05	7	26.25	18.125	100	-4.67E-05	-5.51E-05	-6.98E-05
7	40	7.5	0	-7.92E-05	-8.22E-05	-9.96E-05	7	40	7.5	100	-7.39E-05	-7.73E-05	-9.33E-05
8	22.5	12.5	0	-6.53E-05	-6.90E-05	-9.21E-05	8	22.5	12.5	100	-6.01E-05	-6.44E-05	-8.47E-05
8	36.25	17.5	0	-6.30E-05	-7.06E-05	-8.75E-05	8	36.25	17.5	100	-6.10E-05	-6.58E-05	-8.22E-05
8	18.75	6.875	0	-6.71E-05	-7.65E-05	-9.23E-05	8	18.75	6.875	100	-6.60E-05	-7.13E-05	-8.65E-05
8	32.5	11.875	0	-7.15E-05	-7.42E-05	-9.17E-05	8	32.5	11.875	100	-6.75E-05	-7.06E-05	-8.77E-05
9	15	16.875	0	-5.87E-05	-6.59E-05	-8.39E-05	9	15	16.875	100	-5.38E-05	-6.09E-05	-7.84E-05
9	28.75	6.25	0	-9.75E-05	-9.93E-05	-1.12E-04	9	28.75	6.25	100	-9.13E-05	-9.47E-05	-1.05E-04
2	10	5	0	-3.00E-05	-2.90E-05	-2.91E-05	2	10	5	100	-2.59E-05	-2.52E-05	-2.59E-05
2	10	20	0	-1.22E-05	-1.30E-05	-7.80E-06	2	10	20	100	-1.15E-05	-1.19E-05	-7.25E-06
2	40	5	0	-3.39E-05	-3.45E-05	-3.66E-05	2	40	5	100	-3.12E-05	-3.21E-05	-3.37E-05
2	40	20	0	-1.92E-05	-2.12E-05	-2.84E-05	2	40	20	100	-1.85E-05	-2.02E-05	-2.69E-05
4	40	19.75	0	-3.50E-05	-4.22E-05	-5.73E-05	4	40	19.75	100	-3.19E-05	-3.96E-05	-5.29E-05
5	10	19.75	0	-2.59E-05	-2.81E-05	-3.48E-05	5	10	19.75	100	-2.49E-05	-2.67E-05	-3.39E-05
8	10	19.75	0	-4.21E-05	-4.80E-05	-6.42E-05	8	10	19.75	100	-3.75E-05	-4.31E-05	-5.83E-05
9	15	19.75	0	-5.53E-05	-6.49E-05	-8.28E-05	9	15	19.75	100	-5.45E-05	-6.40E-05	-8.20E-05
9	40	19.75	0	-6.87E-05	-7.37E-05	-8.77E-05	9	40	19.75	100	-6.30E-05	-6.84E-05	-8.45E-05

Table 10. Void coefficient results from SCALE6.2

FL	PF	EN	BOC_V	MOC_V	EOC_V	FL	PF	EN	BOC_V	MOC_V	EOC_V
2	11.25	11.25	1.10E-03	1.11E-03	1.82E-03	6	20	8.75	1.79E-04	7.09E-05	-8.49E-05
2	25	16.25	4.06E-04	3.87E-04	1.01E-03	6	33.75	13.75	-6.85E-05	-1.42E-04	-3.43E-04
2	10	5	2.73E-03	2.73E-03	2.74E-03	6	16.25	18.75	2.48E-05	-7.99E-05	-2.24E-04
2	40	5	1.10E-03	9.53E-04	9.33E-04	6	30	8.125	7.23E-05	4.45E-05	-2.10E-04
2	40	20	1.94E-04	1.58E-04	4.31E-04	7	12.5	13.125	9.60E-05	3.57E-05	-1.34E-04
3	38.75	5.625	5.90E-04	5.13E-04	4.94E-04	7	26.25	18.125	-1.01E-04	-1.89E-04	-3.90E-04
3	21.25	10.625	4.48E-04	4.43E-04	6.63E-04	7	40	7.5	-5.25E-05	-1.18E-04	-3.54E-04
3	35	15.625	1.55E-04	9.98E-05	1.00E-04	8	22.5	12.5	-7.11E-05	-1.42E-04	-4.10E-04
3	17.5	5	1.26E-03	1.10E-03	1.46E-03	8	36.25	17.5	-1.79E-04	-2.52E-04	-3.80E-04
4	31.25	10	1.91E-04	1.40E-04	-1.98E-05	8	18.75	6.875	1.24E-04	8.51E-05	-1.94E-04
4	13.75	15	2.98E-04	2.50E-04	6.34E-04	8	32.5	11.875	-1.36E-04	-1.87E-04	-4.00E-04
4	27.5	20	3.69E-05	-2.60E-05	-1.15E-04	8	10	19.75	1.77E-05	-7.36E-05	-2.10E-04
4	40	19.75	-1.41E-05	-1.24E-04	-2.66E-04	9	15	16.875	-9.08E-05	-1.87E-04	-3.81E-04
5	10	9.375	5.08E-04	4.72E-04	6.77E-04	9	28.75	6.25	-7.45E-05	-1.12E-04	-3.24E-04
5	23.75	14.375	7.47E-05	-2.13E-05	-1.30E-04	9	15	19.75	-1.08E-04	-1.90E-04	-4.44E-04
5	37.5	19.375	-6.95E-05	-1.74E-04	-3.58E-04	9	40	19.75	-1.93E-04	-2.37E-04	-3.56E-04
5	10	19.75	1.80E-04	1.32E-04	3.42E-04						

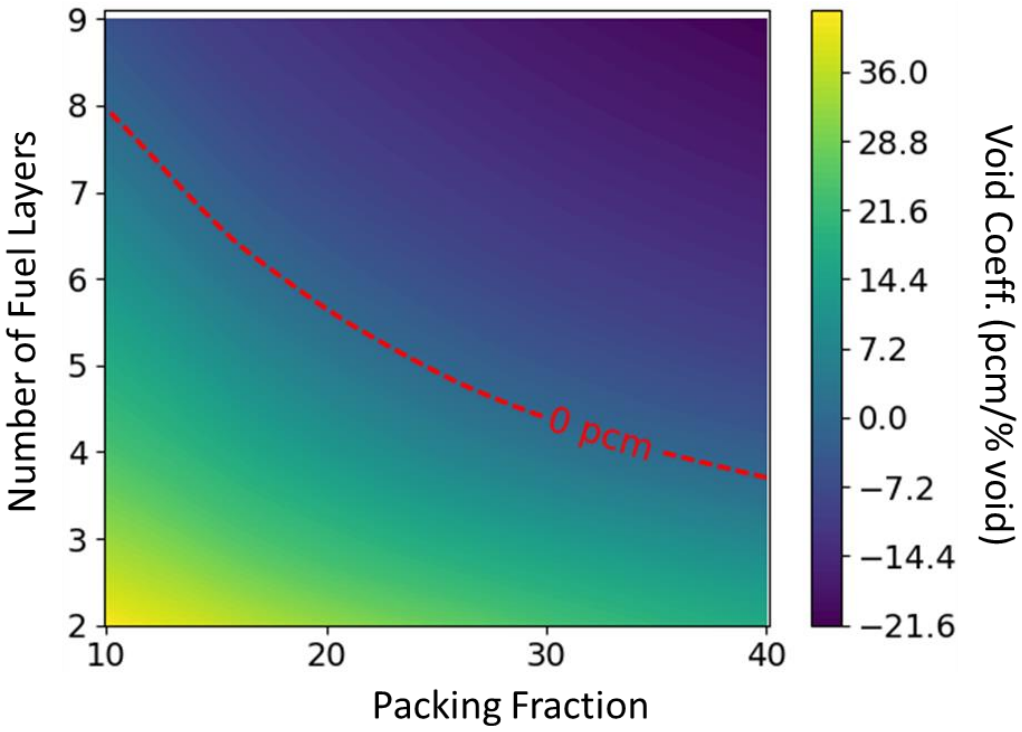

Figure 28. Void coefficient as a function of number of fuel layers and packing fraction with enrichment held constant at 19.75%.

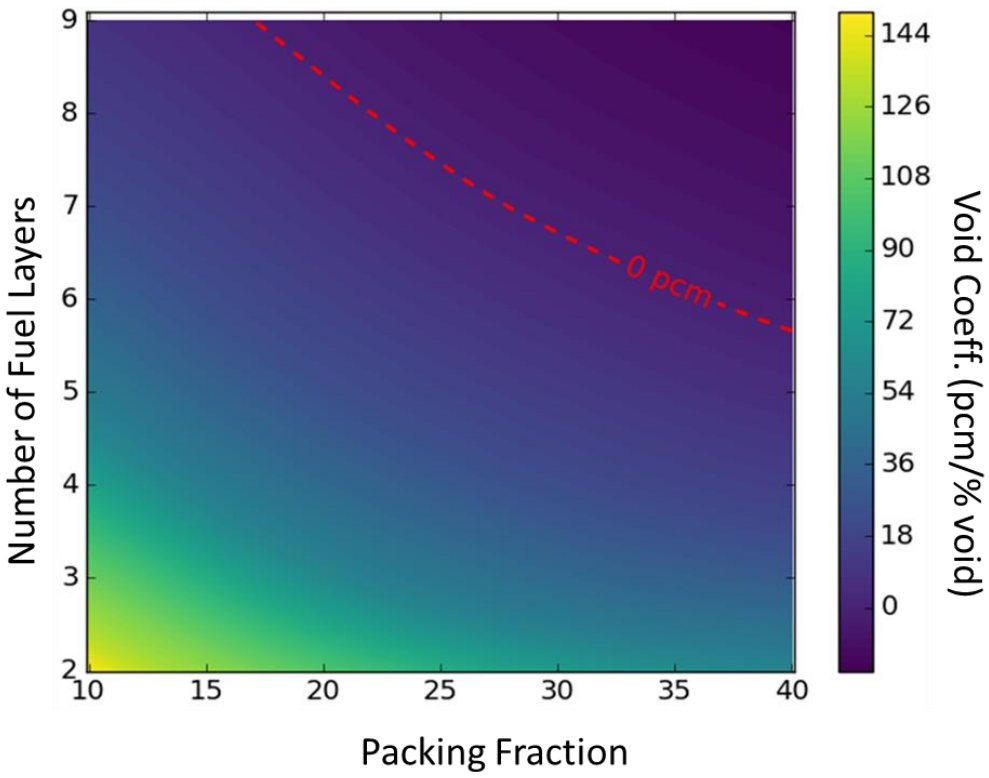

Figure 29. Void coefficient as a function of number of fuel layers and packing fraction with enrichment held constant at 9%.

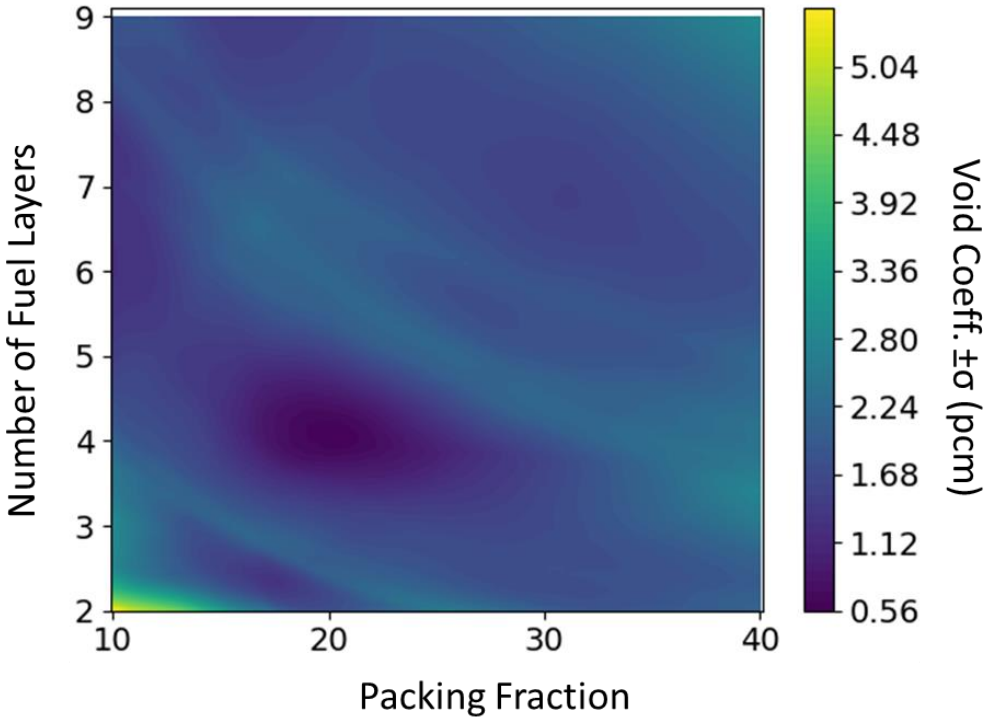

Figure 30. Void coefficient standard deviation as a function of number of fuel layers and packing fraction with enrichment held constant at 19.75%.

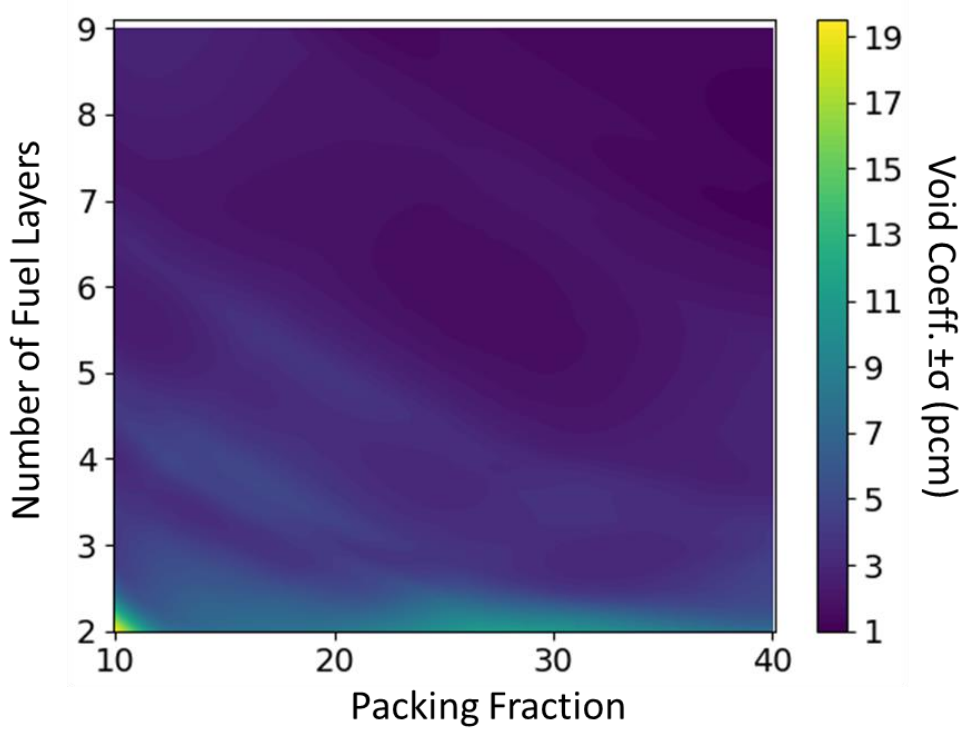

Figure 31. Void coefficient as a function of number of fuel layers and packing fraction with enrichment held constant at 9%.

In addition to the void coefficient, the power coefficient of reactivity is important to consider as a safety constraint for the design. Figure 32 shows the power coefficient calculated with enrichement held constant at 19.75% and power at 100%. Figure 33 shows the power coefficient for 9% enrichment. The power coefficient of reactivity increases as CHM increases. When the enrichment is lowered from 19.75% to 9% enrichment the power coefficient decreases. The power coefficient of reactivity is predicted to be negative over the whole design space. This largely because the significantly negative moderator (graphite) temperature coefficient, and the negative Doppler coefficient. Generally, the fuel and moderator temperature have a much larger increase in temperature as power increases compared to the coolant, making the power coefficient more reliant on the fuel and moderator temperature coefficients.

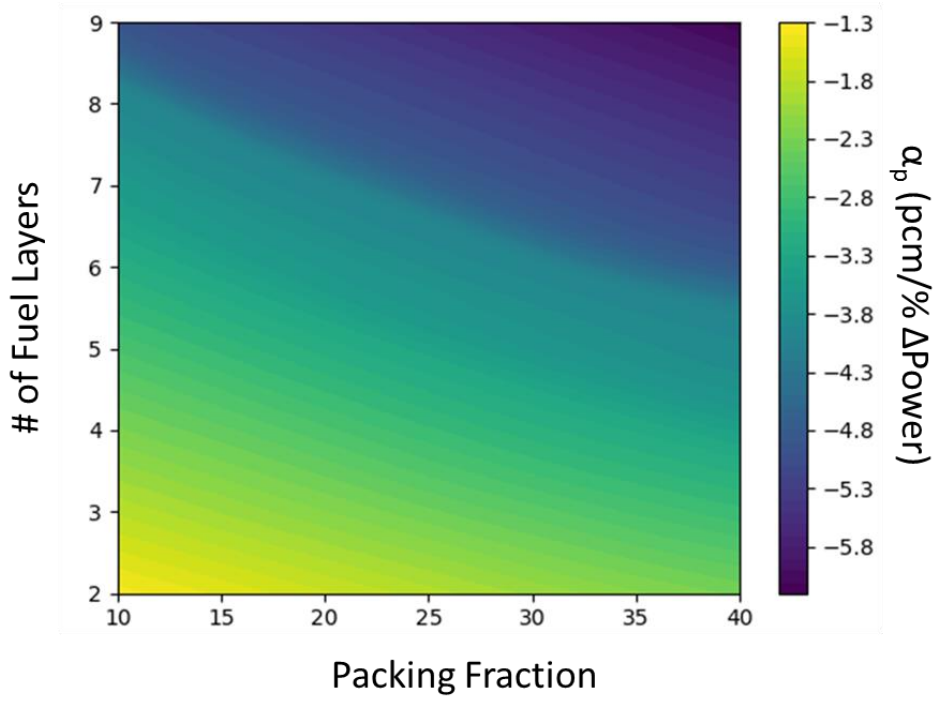

Figure 32. Power reactivity coefficient as a function of number of fuel layers and packing fraction with enrichment held at 19.75%.

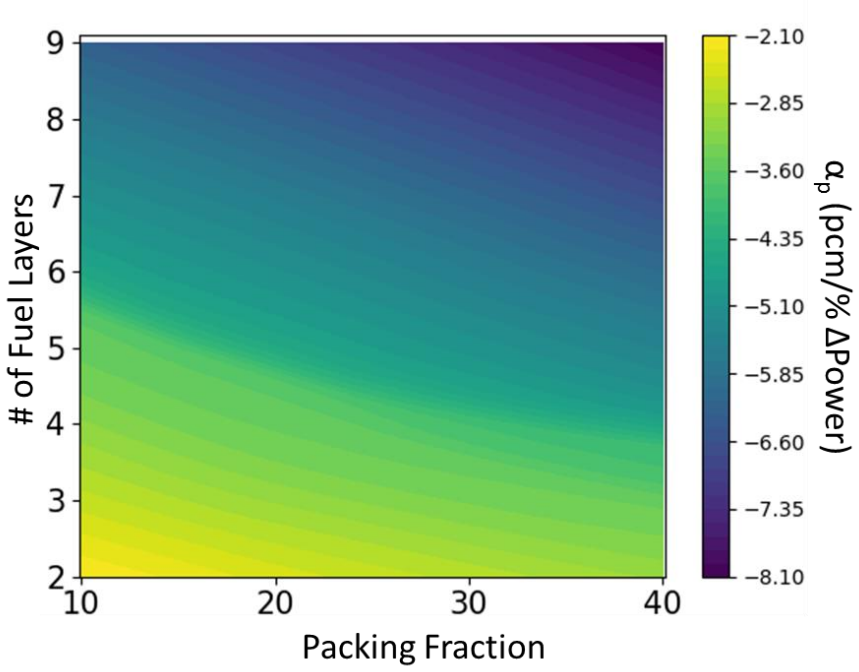

Figure 33. Power coefficient of reactivity as a function of number of fuel layers and packing fraction with enrichment held constant at 19.75%.

CHAPTER 4

STATISITICS AND OPTIMIZATION METHODOLOGY

4.1 Optimization Approach

This chapter presents the methodology developed and used for rigorous design optimization with machine learning. First, the surrogate models are generated in order to provide a computationally inexpensive continuous function to represent the objective function, which is described in this chapter. The objective function is a function of the cost model and the physics model. Once the objective function is accurately modeled an appropriate optimization algorithm is used to reliably find the optimal solution for the design space. Two different optimization algorithms are described in this chapter for the purpose of benchmarking in the next chapter.

The design problem presented in this research is relatively small, from a statistics standpoint, with only four parameters. However, results in Chapter 3 show a non-linear design space with non-linear constraints. Also, the problem design space is concave with local minima that are spread far apart. This requires a global heuristic optimization algorithm to provide a sufficiently reliable prediction of the optimal result. Finally, future work could expand the search space by considering additional fuel design variables.

4.2 Artificial Neural Network Regression

Multi-layer Perceptrons (MLP), also known as Feed-forward Artificial Neural Networks (ANN) have been shown to be highly effective for regression. Theoretically, a sufficiently large single hidden-layer MLP can uniformly approximate any continuous

well behaving function [6]. This makes MLPs effective for generating multi-dimensional non-linear surrogate models.

A deep feed forward neural network architecture, with multiple hidden layers, is used to produce surrogate models for MCDancoff Factors, cycle length, and burnup over the design space. Since the runtime for SCALE Monte Carlo neutron transport calculations are on the order of hours it is impractical to perform optimization calculations by direct simulations of transport and depletion for each design. In order to construct the models libraries in Python, Tensorflow and Keras, are used. These libraries enabled easy use of more advanced activation functions and training algorithms that were ideal for fitting non-linear hypersurfaces. After some testing the Parametric Rectified Linear Unit (PReLU) was found to be the most efficient activation function for fitting these models [12]. Adaptive learning rate methods for stochastic gradient decent (SGD) were also found to be very useful in shortening runtimes. Adam, an algorithm that uses adaptive momentum estimation, was chosen as the optimizer for SGD [17]. The algorithm adjust its learning rates for the parameters based on the gradient.

MLP's produce unstable solutions due to their stochastic nature. Larger networks are also very prone to overfitting. To mitigate overfitting bootstrap aggregation, dropout, and L2 regularization [20], [26], [28] were considered. L2 regularization is straight forward to implement, but many simulations would be required to optimize the parameter so the model can converge without overfitting. L2 regularization is also not as robust for larger networks compared to other methods [28]. Bootstrap aggregation is a very straightforward method that requires more computational time but significantly reduces error, overfitting, and provides an approximate confidence interval for the fit [20].

Dropout is effective for preventing overfitting since it forces the network to not rely too heavily on individual neurons and approximates having multiple networks with different architectures [26]. Bootstrap aggregation and dropout were chosen to generate the models. While there is some redundancy in using both dropout and bootstrap aggregation, it provides a much more robust model with an estimate of the confidence interval which is very useful for design optimization. In this case, precision on the order of 10^{-5} (reactivity pcm) is needed without overfitting, requiring more care when training the model. The network architecture has between 3 to 5 hidden layers depending on the data set fitted. The first hidden layer contains between 402-404 neurons, the second layer contains 148-150 neurons, the third layer contains 54-56 neurons, and so on in an exponentially decreasing pattern. Figure 34 shows a general layout of the neural network for modeling the MCDancoff Factor. The figure shows the nodes fully connected, which is appropriate for regression since in many non-linear problems there is often interdependency between parameters' effect on the objective function.

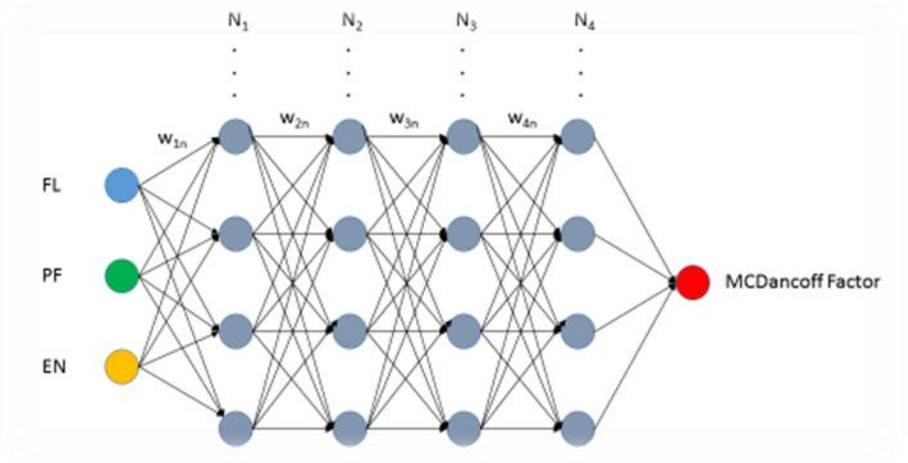

Figure 34. Deep Multi-layer Perceptron graph.

The following equation is used to describe how the weights propagate through the network and are activated at each node:

$$\boldsymbol{output} = \sum_{i=1}^{I} \boldsymbol{w_i f^i}\left(\sum_{j=1}^{J} \boldsymbol{w_j f^j}\left(\sum_{k=1}^{K} \boldsymbol{w_k f^k}\left(\sum_{l=1}^{L}(\boldsymbol{w_l x_l} - \boldsymbol{\theta_l}) - \boldsymbol{\theta_k}\right) - \boldsymbol{\theta_j}\right) - \boldsymbol{\theta_i}\right) \qquad (4.1)$$

Where w is a weight, f is an activation function, and θ is a constant, called a bias. The activation function used for this study, Parametric Rectified Linear Unit (PReLU), was recently developed to enhance image classification and was found to be very effective for deep neural network regression compared to other activation functions. Figure 35 shows the PReLU function, where α is adjusted by the chain rule during backpropagation.

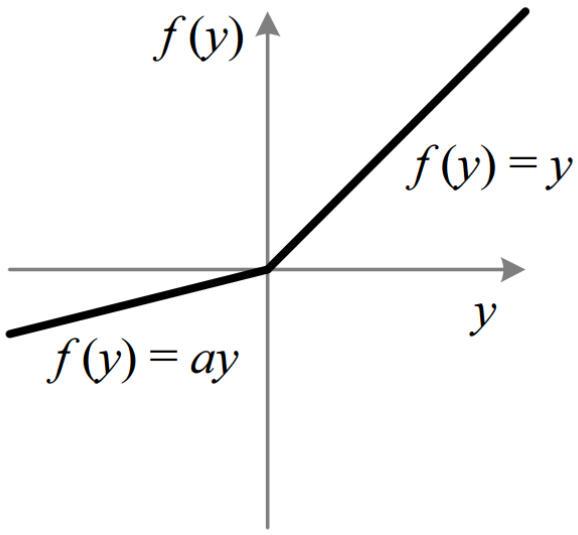

Figure 35. Plot of the PReLU activation function.

4.3 Global Heuristic Optimization

4.3.1 Preferred Neighborhood Aggregation Algorithm

A novel approach was taken to search for the optimum design. It is not only desirable to find the optimum, but also to analyze the sensitivity of the objective function in the region within the uncertainty of the optimum. A new algorithm, Preferred Neighborhood Aggregation (PNA) was developed to perform a global optimum search and converge upon the region within uncertainty of the optimum. Figure 36 shows a flowchart of the method.

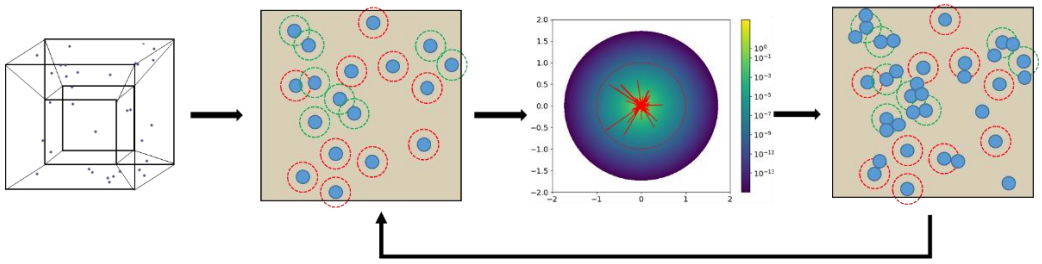

Figure 36. Flowchart showing processes in the Preferred Neighborhood Aggregation Algorithm.

The method begins with initially sampling over the design space. This can be done uniformly or randomly. The solutions are then evaluated and compared to the best solution. Members of the population which are within a desired level of uncertainty are considered "good" solutions. Solutions which don't fall within the level of uncertainty of the best solution are "poor" solutions. A cumulative distribution function (CDF) is then made with the best solution given a 5% chance of spawning a new neighbor, good solutions having a total of 70% chance of getting a new neighbor, and poor solutions given a total of 25% chance of getting a new neighbor. These probabilities were chosen so the new solution would be more likely to spawn near a good solution or the best solution so far, but would occasionally look elsewhere to efficiently explore the design space. Currently, they are simply initial guesses that are expected to provide acceptable

results. When a new sample is spawned it arrives randomly within a hypersphere of radius r_g around a random member of the previous generations based on the CDF. When the population of the new generation reaches size of the original population the objective function is evaluated for each member and compared to the value of the best solution so far. The members of the population are then categorized and added to the CDF for the next generation. This process is repeated until the optimal solution converges and the region of solutions within the level of uncertainty converges. When a new best solution is found, members of previous generations stored in the CDF in the good and poor solution lists are erased and the CDF is calculated with the new generation.

The radius of the hypersphere is determined by the number of parameters, the size of the population, width of the design hyperspace, and a varying radius factor. When the radius factor is equal to one, the hypersphere is large enough that neighboring members of the population, including those that are diagonal, are within the hypersphere assuming a hyper-cubic uniform lattice within the design hyperspace. The following definition for the radius was introduced and calculated each generation:

$$\boldsymbol{r_g = \frac{L\sqrt{m}}{n^{\frac{1}{m}} - 1} e^{-\xi nm}} \qquad (4.2)$$

Where L is the width of the design hyperspace, n is the size of the population, m is the number of parameters, and ξ is a random number between 0 and 1 that is changed for each parameter and causes the probability distribution function to become hyper-ellipsoidal. The generational radius equation makes it much more probable for the PNA algorithm to search very close to a previous solution. Furthermore, it has a small

probability of "jumping" in a single direction to more thoroughly explore the design space without sacrificing good convergence.

The vector from the randomly chosen parent to the new member being spawned within the surrounding hypersphere is calculated with n–dimensional spherical coordinates. The equations below show the conversion from Cartesian to n-dimensional spherical coordinates:

$$x_1 = r_g(\xi_{1j})\cos(\varphi_1)$$

$$x_2 = r_g(\xi_{2j})sin(\varphi_1)\cos(\varphi_2)$$

$$x_3 = r_g(\xi_{3j})sin(\varphi_1)sin(\varphi_2)\cos(\varphi_3)$$

$$\vdots$$

$$x_{n-1} = r_g(\xi_{(n-1)j})sin(\varphi_1)\cdots sin(\varphi_{n-2})\cos(\varphi_{n-1})$$

$$\boldsymbol{x_n = r_g(\xi_{nj})sin(\varphi_1)\cdots sin(\varphi_{n-1})\,\mathbf{sin}(\varphi_{n-1})} \qquad (4.3)$$

Where ξ_{ij} is a random number generated for each parameter i of a new member j of the population. φ_{n-1} ranges from 0 to 2π, while angles $\varphi_1, \varphi_2,\ldots,\varphi_{n-2}$ range from 0 to π.

The algorithm approximately converges to an optimal solution when the number of good solutions stops increasing and a new best solution is not found for a certain number of generations. The solution must meet the "No acceptance criteria" to converge. The "No acceptance criteria" is met when after a certain number of generations no improvement has been made in the best solution [34]. This ensures that the generation of good solutions are in equilibrium with poor solutions ensuring that the design space is well searched.

4.3.2 Differential Evolution

The Differential Evolution Algorithm (DE) is a global heuristic optimization algorithm under the category of evolutionary algorithms. It is used in this research to benchmark the PNA algorithm. It is somewhat similar to Genetic Algorithms (GAs) since it has a population of designs with variables that are exchanged amongst the designs. However, GA's exchange variables through mating while DE mutates its population by linear transformations randomly between each member of the population [31]. In general DE outperforms GA both in reliability of solutions and in runtime. Figure 37 is the flowchart of how DE progresses.

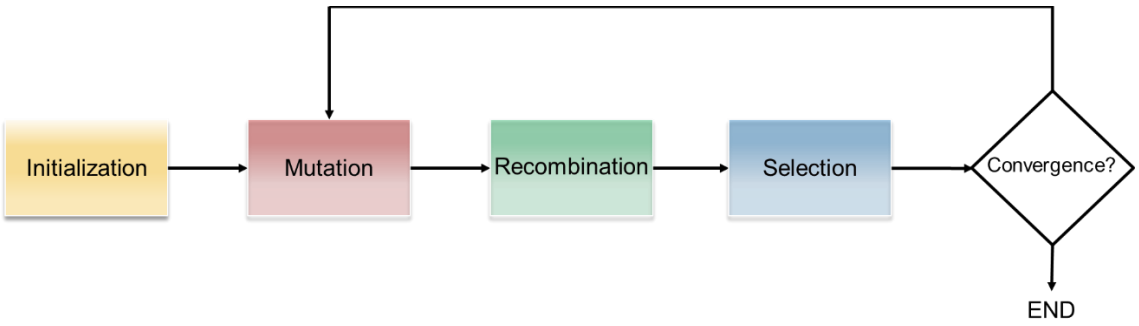

Figure 37. DE algorithm flowchart.

First the parameters are initialized. Then the population is generated randomly over the design space. Next, the loop of the algorithm starts with mutation over the population. Each member of the population goes through mutation in series. The parameter vector of the member of the population is called the target vector. Three other member parameter vectors are chosen at random to generate the donor vector through a linear transformation. Then in recombination the trial vector is generated when the parameters from the donor vector donates each parameter value to the target vector with a probability of acceptance given by the crossover ratio, an input parameter between [0,1]. Finally, in

the last step of the generation, selection, the trial vector and the target vector are evaluated based on the objective function. The trial vector and the target vector are compared on merit and the better of the two determines the parameters of the member in the next generation. If the target vector is the better design then it remains in the population until it is mutated resulting in a better design. This process of mutation, recombination, and selection repeats until convergence. Figure 38 shows a visualization of the mutation step. Figure 39 shows a visualization of recombination. The code used to execute the DE algorithm is from the SciPy Optimize library in Python.

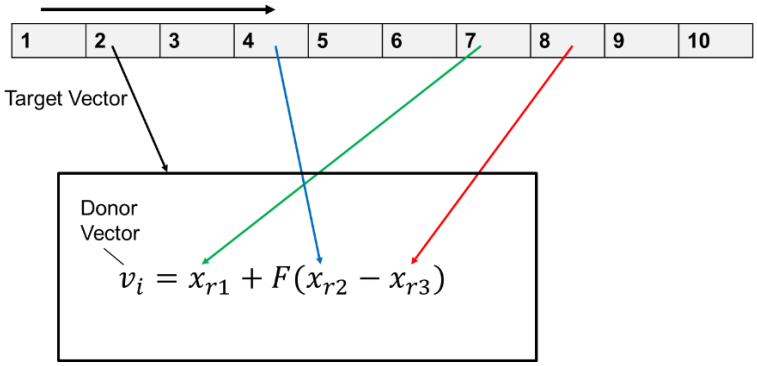

Figure 38 Visualization showing the recombination process.

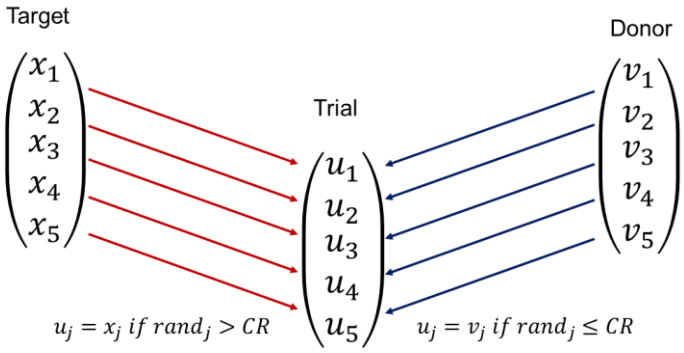

Figure 39. Visualization of the mutation process in DE.

4.4 Fuel Cycle Cost Model

A detailed fuel cycle cost model was used as the objective function for optimization of the fuel design. The fuel cycle cost model takes into account manufacturing cost of the planks, enrichment cost, cost of capital in manufacturing, quality assurance, and outage costs. The largest contributions to uncertainty in the cost model come from cost of manufacturing TRISO particles and determination of outage costs for this type of reactor. The overall fuel cycle cost is a balance of fuel utilization and outage costs. The cost model used in this research was adapted from the cost model developed by Chris Kingsbury [18], [19]. The cost model has been expanded to model changes in the plank thickness and number of fuel layers. Ultimately, the fuel cycle cost is represented by the two main components:

$$\boldsymbol{FCC} = \frac{\boldsymbol{Cost_{fuel}}[\$/\boldsymbol{kgU}]}{\boldsymbol{BU}[\boldsymbol{GWd/tHM}]*\boldsymbol{24}[\boldsymbol{h/d}]*\boldsymbol{\eta}} + \frac{(\boldsymbol{Cost_{outage}}[\$]}{(\boldsymbol{CL}[\boldsymbol{FPD}]*\boldsymbol{3400}[\boldsymbol{MWth}]*\boldsymbol{24}[\boldsymbol{h/d}]*\boldsymbol{\eta}))} \text{ (\$/MWh)} \qquad \textbf{(4.4)}$$

Where BU is discharge burnup in GWd/tHM, CL is cycle length, and η is the thermodynamic efficiency of the plant, assumed to be 44.1% for this study. The left term on the right side of the equation decreases with better fuel utilization. The rightmost term decreases when the outage cost is decreased or when cycle length is increased.

The objective function is then minimized with the following conditions in order to optimize the fuel design:

$$\textbf{minimize} \quad FCC(\text{BU}(FL,PF,EN,BA), \text{CL}(FL,PF,EN,BA))$$

$$\textbf{`subject to}: \quad \alpha_P(FL,PF,EN) \;\&\; \alpha_{void}(FL,PF,EN) \leq 0$$

$$2 \leq FL \leq 9$$

$$10\% \leq PF \leq 40\%$$

$$5\% \leq EN \leq 19.75\%$$

$$\mathbf{1} \leq \boldsymbol{BA} \leq \mathbf{6} \tag{4.5}$$

Where the objective function is a function of burnup and cycle length. The design is constrained to have negative power and void coefficients. The constraints on the parameters, number of fuel layers, packing fraction, enrichment, and number of batches, were chosen based on feasibility.

CHAPTER 5

OPTIMIZATION RESULTS

5.1 Preferred Neighborhood Aggregation Algorithm Benchmark

Benchmark calculations were performed to verify the PNA algorithm on a difficult global optimization problem. The PNA algorithm was compared to the DE algorithm on the Rastrigin Function in 2, 5, 10, 15, and 20 dimensions. The Rastrigin Function is characterized by the following equation:

$$\boldsymbol{f(x) = 10n + \sum_{i=1}^{n}\left[x_i^2 + 10cos(2\pi x_i)\right]} \quad \textbf{(5.1)}$$

Where n is number of dimensions, and $x_i \in [-5.12, 5.12]$. The function has a global minimum of $f(\boldsymbol{x} = \boldsymbol{0}) = 0$. The Rastrigin Function is a multimodal function making it more difficult to find the global minimum. Figure 40 is a surface plot of the Rastrigin Function in 2D

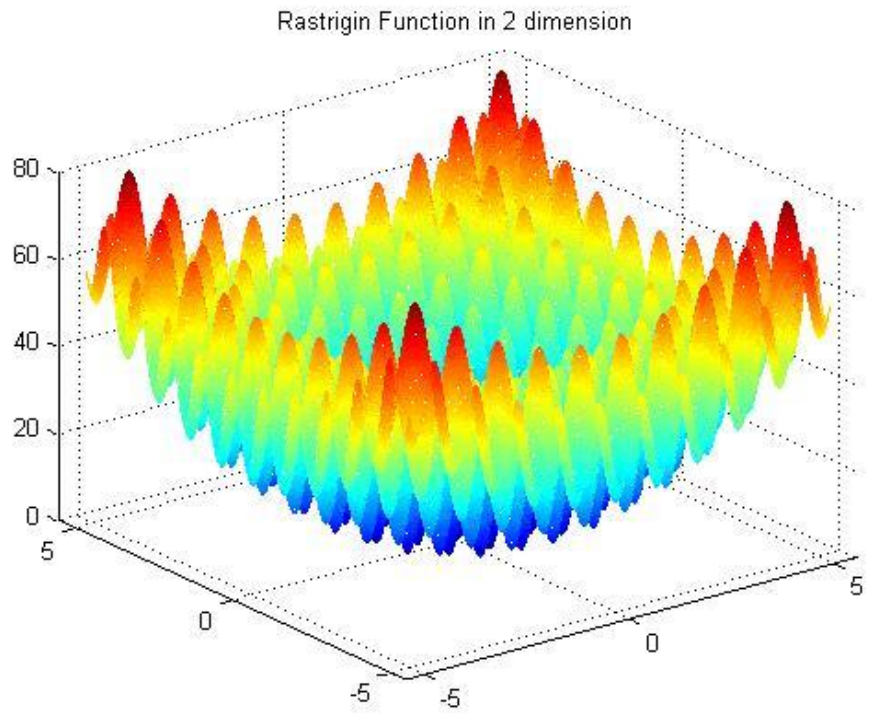

Figure 40. Plot of the Rastrigin Function in 2D.

The benchmark calculations are performed with both algorithms having a population of 15. The PNA algorithm is set to assume the uncertainty of each solution is f(**x**)/n for the benchmark. Benchmark calculations are compared in the number of objective function evaluations (fev) since some algorithms may evaluate the objective function many times per generation per population member. This can make it seem to converge faster, when in reality it often requires more calculations. Using fev provides a more even metric. An algorithm converging with fewer fev is more efficient. Benchmark results show that at lower dimensions the DE algorithm slightly outperforms the PNA algorithm in the number of objective function evaluations. At ten dimensions however, the results show PNA outperforms DE by almost a factor of three in the number of fev. At twenty dimensions PNA converges after about a quarter million fev, while DE doesn't even converge, but gets stuck at a local minimum even after over 700,000 fev. Table 11

shows a comparison of the two algorithms at 2, 5, 10, 15, and 20 dimensions. Figure 41 shows the convergence with fev for the PNA algorithm over the twenty dimensional Rastrigin Function. Figure 42 shows the convergence of the DE algorithm with fev. Figure 43 is a plot that compares the efficiency of PNA vs. DE as a function of dimensions. These results indicate that the PNA algorithm is more robust than the vanilla DE algorithm, especially at higher dimensionality.

Table 11. Resulting value of the objective function for the benchmark calculations comparing the PNA algorithm with the DE algorithm. (Value of true optimum is 0.)

2 Dimensions		
DE	0	2013
PNA	0	3045
5 Dimensions		
DE	0	15081
PNA	0	28230
10 Dimensions		
DE	0	84311
PNA	0	30810
15 Dimensions		
DE	0.9949591	332630
PNA	0	233325
20 Dimensions		
Algorithm	Result	FEV
DE	3.9798	718605
PNA	0	286000

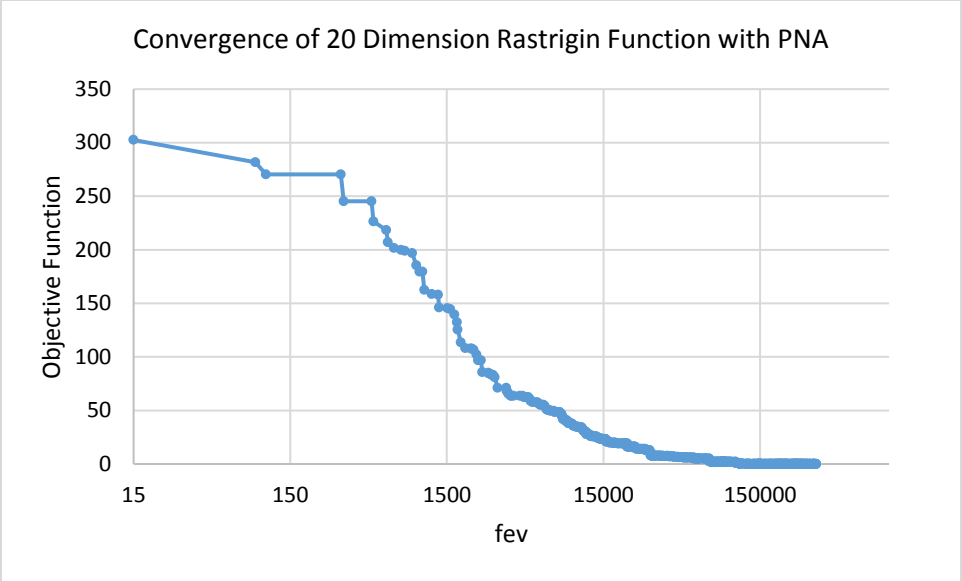

Figure 41. Convergence of Rastrigin Function in 20 dimension using Preferred Neighborhood Algorithm.

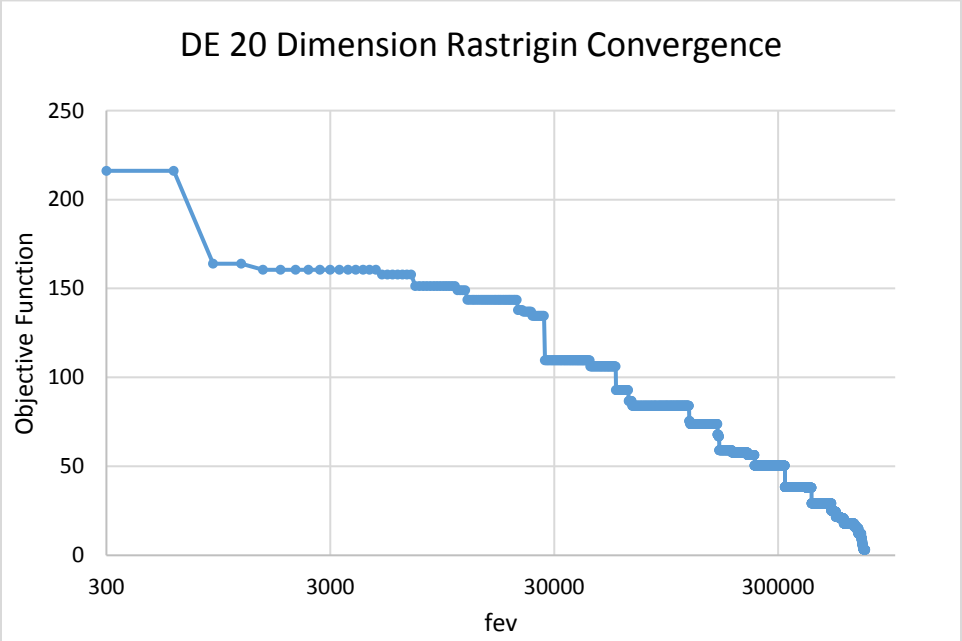

Figure 42. Differential Evolution Algorithm convergence on a 20 dimension Rastrigin function.

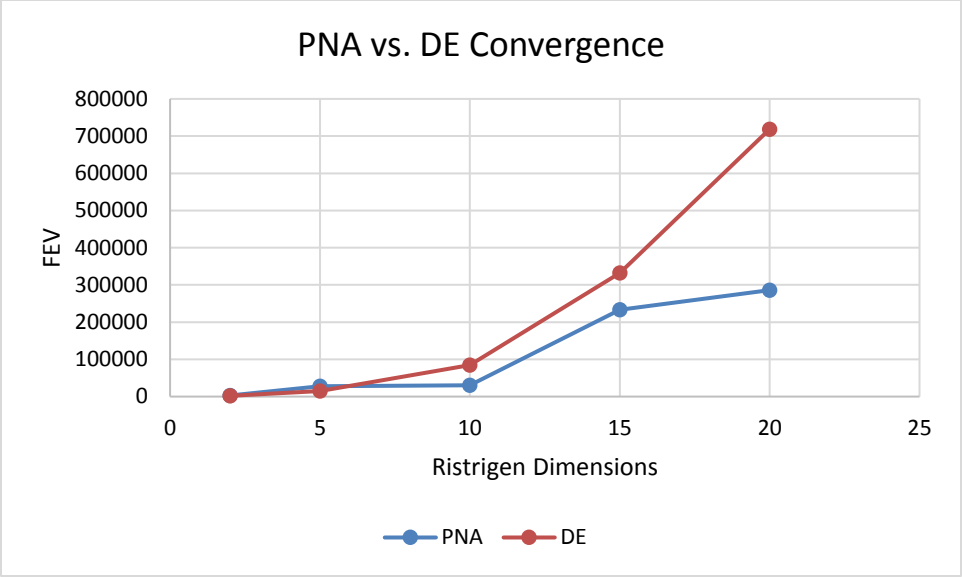

Figure 43. Comparison of PNA to DE convergence with different dimensions of the Rastrigin function.

5.2 Optimization with Cost Scenarios

Currently, there is a very large uncertainty in the fabrication cost for TRISO fuel and a very large uncertainty for the outage cost of refueling the AHTR. Since the uncertainty of the contribution to the objective function from these costs is likely to be even larger than the objective function, it is more useful to assume several cost scenarios were the two costs are set constant. The TRISO manufacturing cost per particle is assumed to be $0.01 for the high cost scenario and $0.00001 for the low cost scenario. The high outage cost scenario assumes a $50 million per outage cost, while the low outage cost scenario assumes a $20 million per outage cost. Analysis of different combinations of these scenarios provides insight into the sensitivity of the optimal design to costs. The optimization calculations are performed with the PNA algorithm set to find the region within 2σ of the optimal result.

5.2.1 High TRISO Fabrication Cost with High Outage Cost

The most pessimistic scenario predicts a FCC of 23.45 $/MWh. The design has 4.39 fuel layers, 39% packing fraction, 19.75% enrichment, and a 3.6 batch fuel cycle. Figure 44 shows the fuel cycle cost as a function of number of fuel layers and packing fraction. It also shows how the optimal solution converges over the slice of the design space. The figure is generated with enrichment held constant (sliced at optimal locations for showing a 2D figure) at 19.75% and number of refueling batches at 3.6. The FCC generally decreases with increasing CHM but is limited by the void coefficient. The optimal solution is at the constraining boundary. Figure 45 shows the standard deviation of the FCC (propagated uncertainty) over the section of the design space with enrichment held constant at 19.75% and number of refueling batches at 3.6. The standard deviation is generated from the ensemble of neural networks fitting the physics model. The standard deviation maxes out at about .5 $/MWh but is not near the optimal solution and has a FCC well above 2σ of the FCC of the optimal solution. The regions that have a FCC similar to the optimal solution have a relatively low standard deviation below .2 $/MWh and as low as .032 $/MWh.

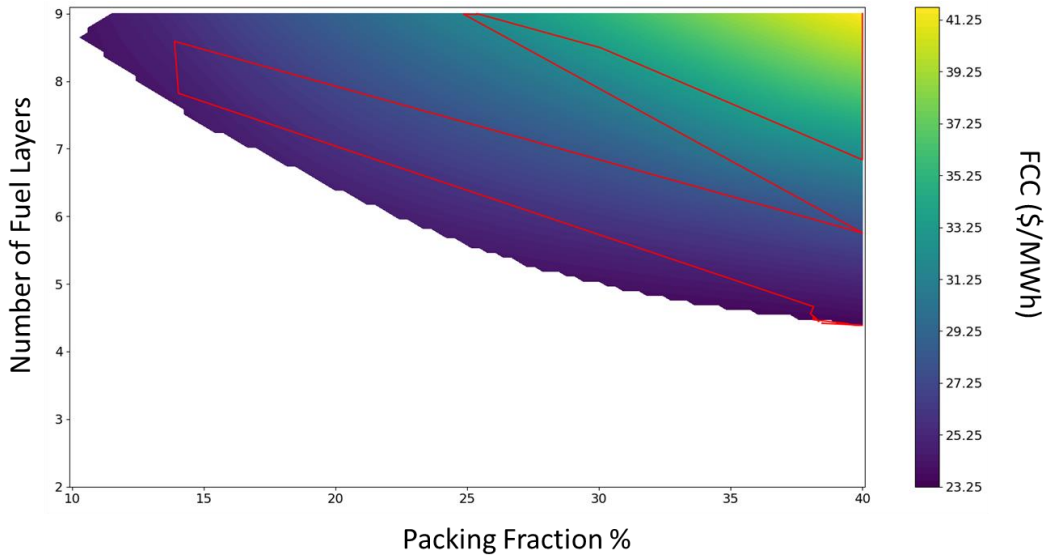

Figure 44. Convergence of best solution over the design space and FCC with enrichment held constant at 19.75% and 3.6 batches.

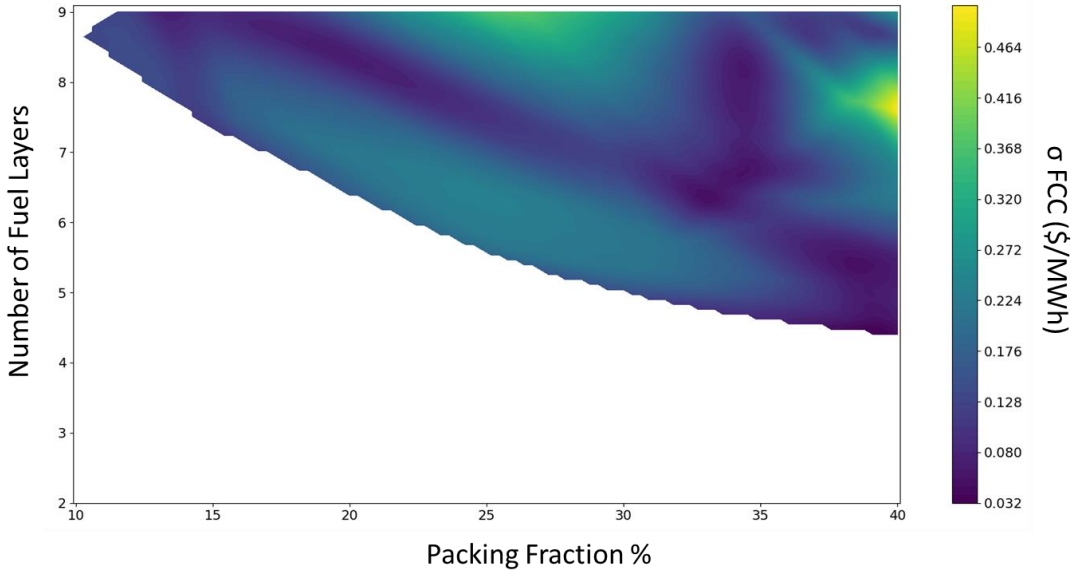

Figure 45. Standard Deviation of FCC ($/MWh) with enrichment held constant at 19.75% and 3.6 batches.

Figure 46 shows the convergence of the PNA algorithm for the design problem. It converges to the solution after about 1300 epochs (or generations) which corresponds to about 13000 objective function evaluations with a population size of 10. Figure 47 shows

a collection of solutions that are within 2σ of the optimal solution. This figure shows that the FCC is very sensitive to CHM as the range of solutions over packing fraction and number of fuel layers is small. The FCC is not very sensitive to number of batches. The design's performance is extremely sensitive to enrichment with all the solutions huddled near 19.75%.The average packing fraction among acceptable solutions is 39.8 ± .39%, the average number of fuel layers is 4.39 ± .025, the average enrichment is 19.74 ± .036%, and the average number of batches is 4.48 ± .57.

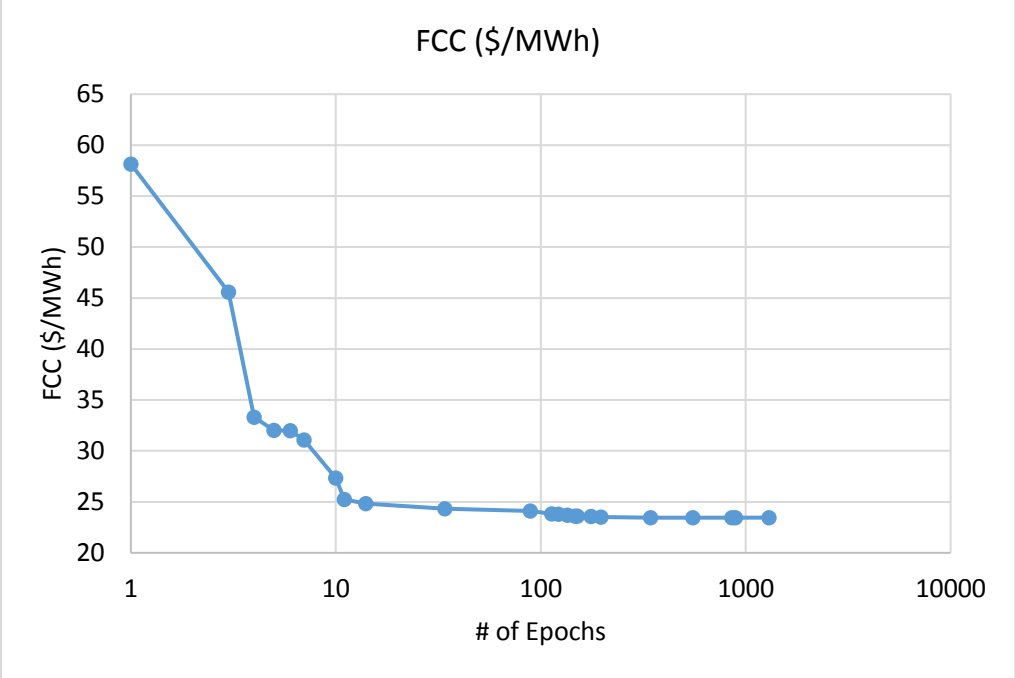

Figure 46. Convergence of optimal solution with increasing epochs.

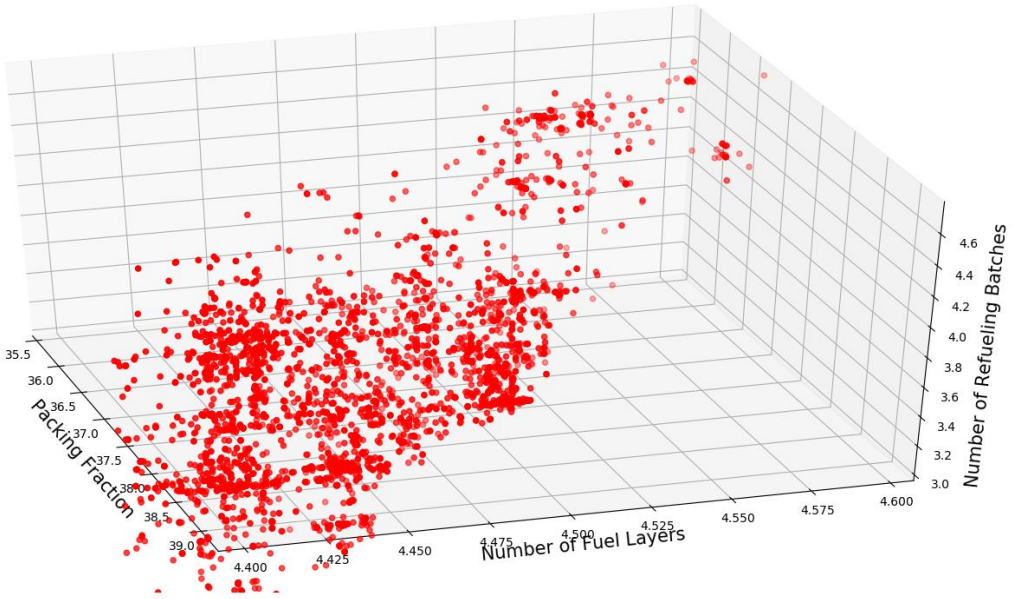

Figure 47. Solutions within 2σ of the optimal solution.

5.2.2 High TRISO Fabrication Cost with Low Outage Cost

Lowering the outage cost from $50 million to $20 million results in a FCC of 20.37 $/MWh. This is a design that has 4.42 FL, 38.6% packing fraction, 19.75% enrichment, and a 6 batch fuel cycle. When the outage cost is significantly reduced it is much more advantageous to increase the number of fuel batches, thus increasing discharge burnup and fuel utilization, in spite of the need to reload more frequently. This provides a modest reduction in fuel cycle cost compared to the most pessimistic case. The optimal fuel design is nearly the same as in the previous case. Figure 48 shows the FCC as a function of number of fuel layers and packing fraction with enrichment held constant at 19.75% and number of refueling batches constant at 6. It also shows how the optimal solution converges over the design space. Figure 49 shows the standard deviation of FCC as a function of number of fuel layers and packing fraction.

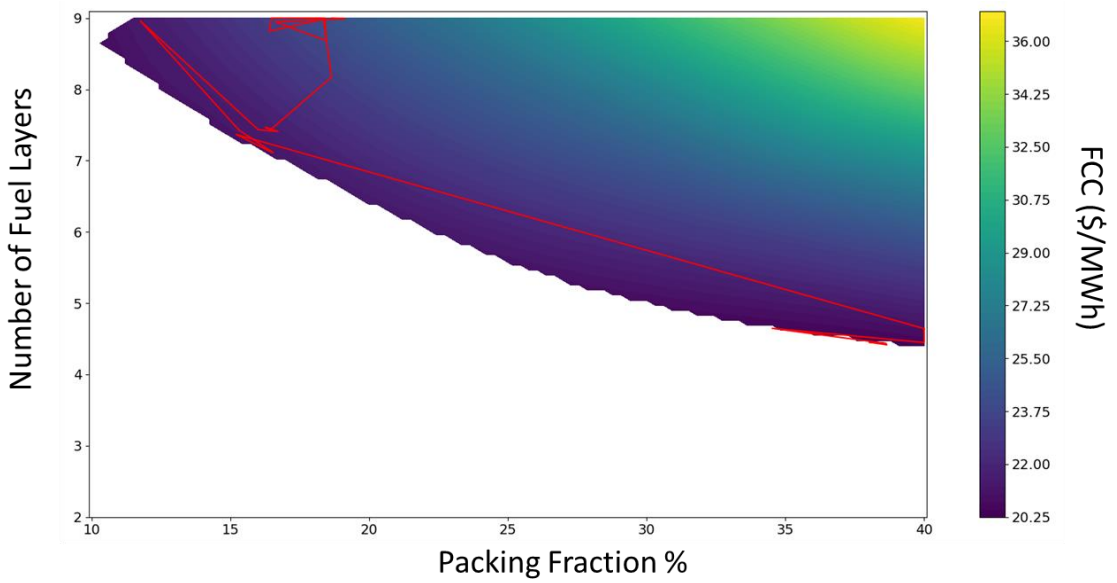

Figure 48. Convergence of the best solution over the design space and FCC with enrichment held constant at 19.75% and 6 batches.

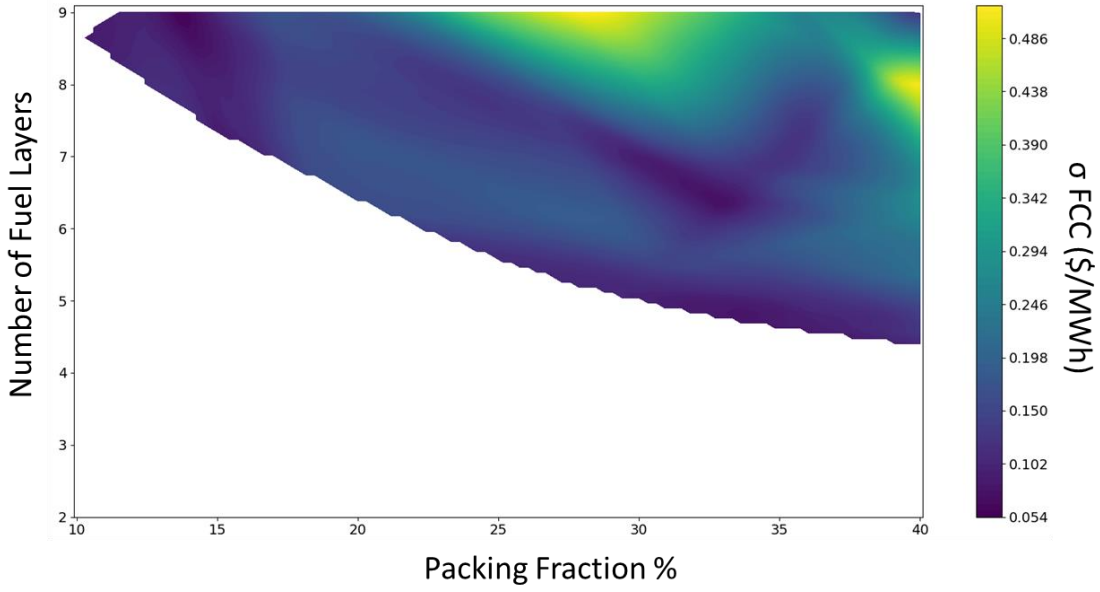

Figure 49. Standard deviation of FCC with enrichment held constant at 19.75% and 6 batches.

Figure 50 shows the distribution of solutions within 2σ of the optimal solution. It is evident that the solutions are hugging along the void coefficient constraint and that maximizing CHM minimizes FCC. It appears that in this scenario the optimum design is somewhat sensitive to number of refueling batches and would benefit from the number of

batches increase since the optimal solution is at the edge of the design space. Figure 51 shows the convergence of the optimum solution as a function of the number of epochs.

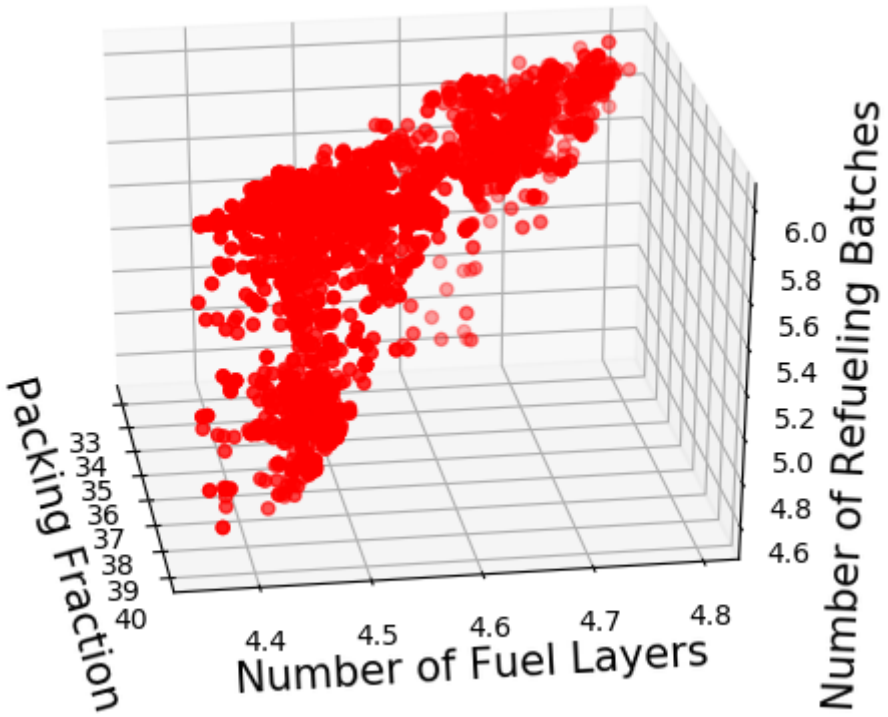

Figure 50. Solutions within 2σ of the optimal solution.

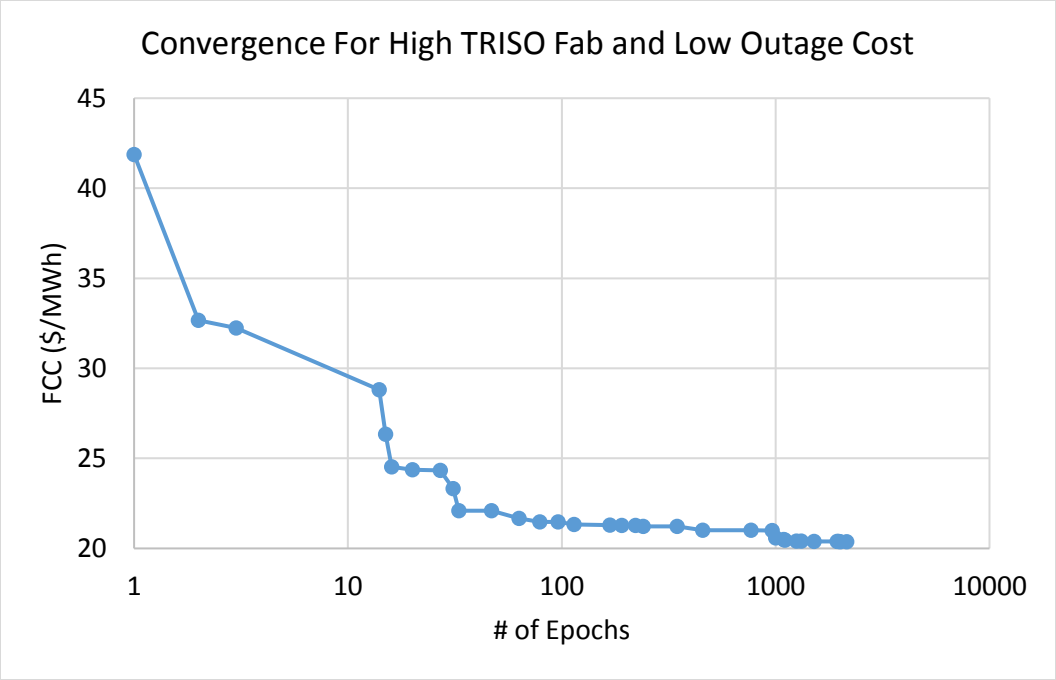

Figure 51. Convergence of optimal solution with increasing epochs.

5.2.3 Low TRISO Fabrication Cost with High Outage Cost

Lowering the cost of TRISO particle fabrication results in a slight shift in the design. The design shifts to increase cycle length (and reduce the frequency of outages) at a slight expense to fuel utilization. The FCC is significantly lowered down to 9.61 $/MWh. Figure 52 shows the FCC as a function of number of fuel layers and packing fraction with enrichment and number of batches held constant at 19.75% and 2.23 as well as the convergence of the best solution. The resulting design has 4.36 fuel layers, 40% packing fraction, 19.75% enrichment, and a 2.2 batch fuel cycle. Figure 53 shows the standard deviation of FCC as a function of packing fraction and number of fuel layers.

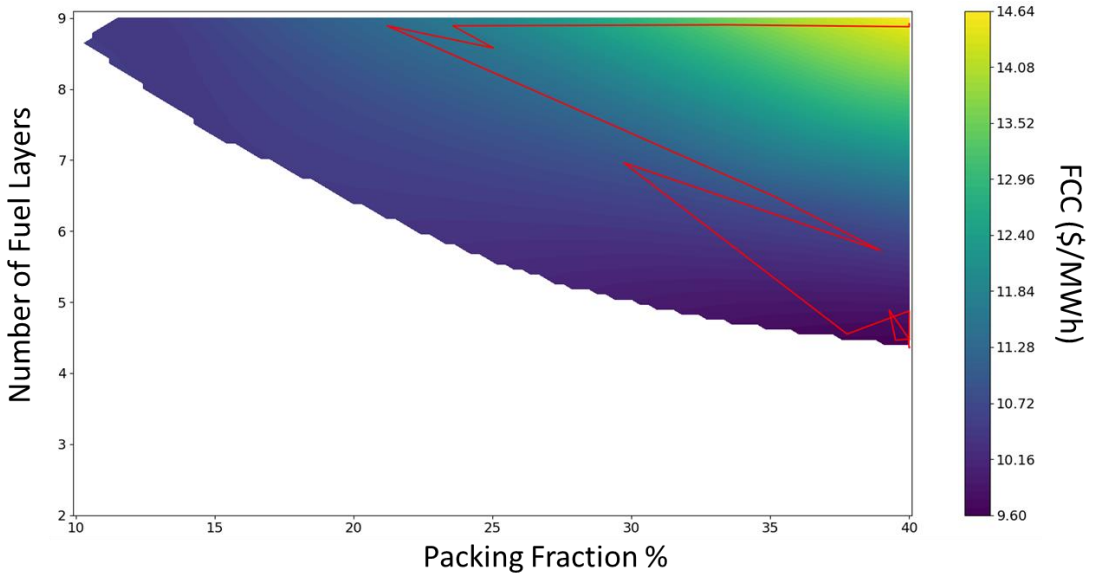

Figure 52. Convergence of the best solution over the design space and FCC with enrichment held constant at 19.75% and 2.2 batches.

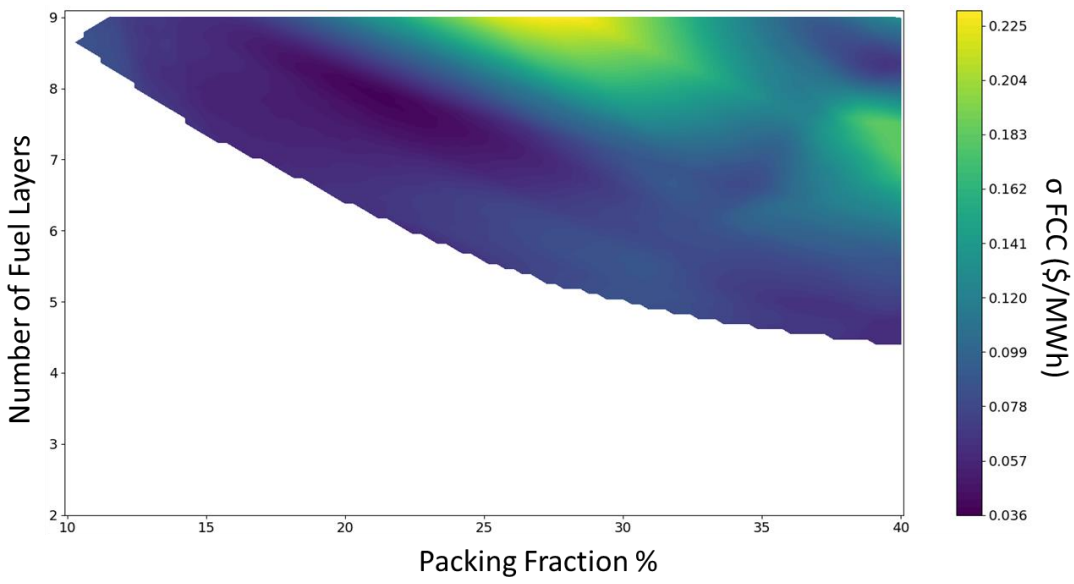

Figure 53. Standard Deviation of FCC ($/MWh) with enrichment held constant at 19.75% and 2.2 batches.

Figure 54 shows the distribution of solutions within 2σ of the optimal solution. It can be seen that the FCC is very sensitive to packing fraction and it appears that the solutions are tightly packed at the constraint on packing fraction. Figure 55 shows the convergence of the optimal solution.

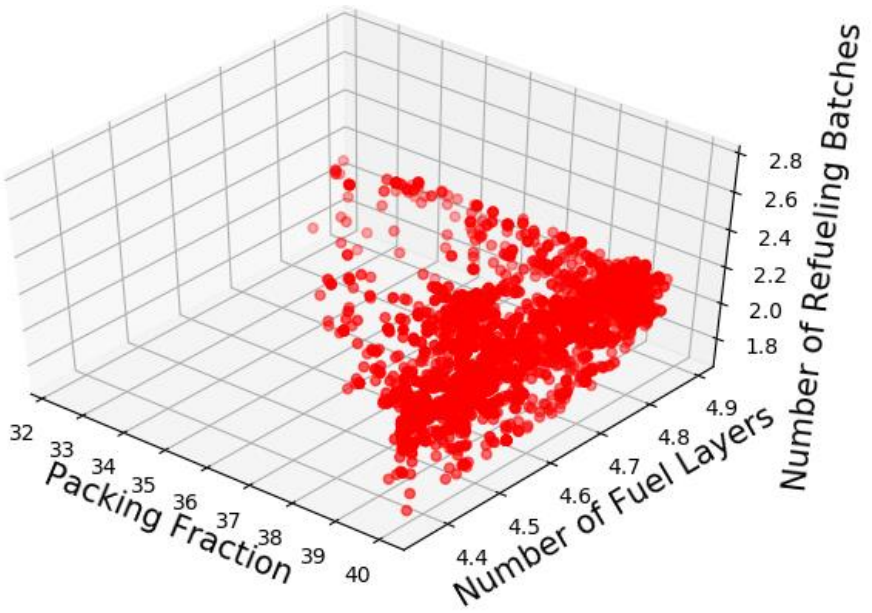

Figure 54. Solutions within 2σ of the optimal solution.

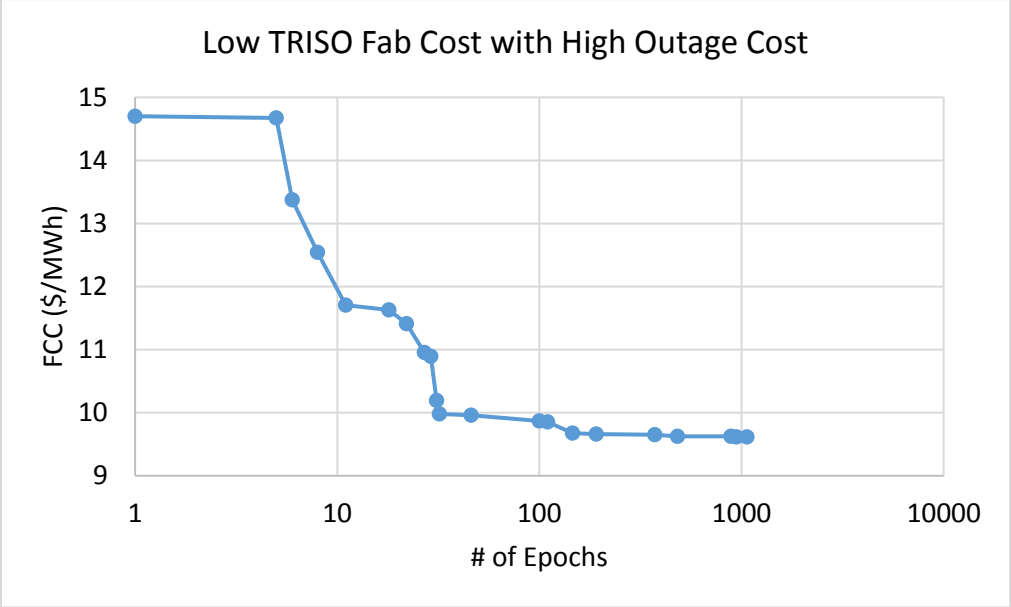

Figure 55. Convergence of optimal solution with increasing epochs.

5.2.4 Low TRISO Fabrication Cost with Low Outage Cost

It is apparent that the low TRISO fabrication cost scenarios lead to a slightly higher packing fraction, while lowering the outage cost doesn't directly impact the fuel plank design. Instead it leads to an increase in the number of batches. This scenario has

an optimal solution of 7.89 $/MWh with a design that has 4.36 fuel layers, 40% packing fraction, 19.75% enrichment, and 3.3 refueling batches. Figure 56 shows the FCC as a function of number of fuel layers and packing fraction with enrichment and number of batches held constant at 19.75% and 3.3 as well as the convergence of the best solution. Figure 57 shows the standard deviation of FCC as a function of packing fraction and number of fuel layers. Figure 58 shows the distribution of solutions within 2σ of the optimal solution. The distribution is similar to the previous scenario where the solutions are clustered at the packing fraction constraint. Figure 59 shows the convergence of the optimal solution.

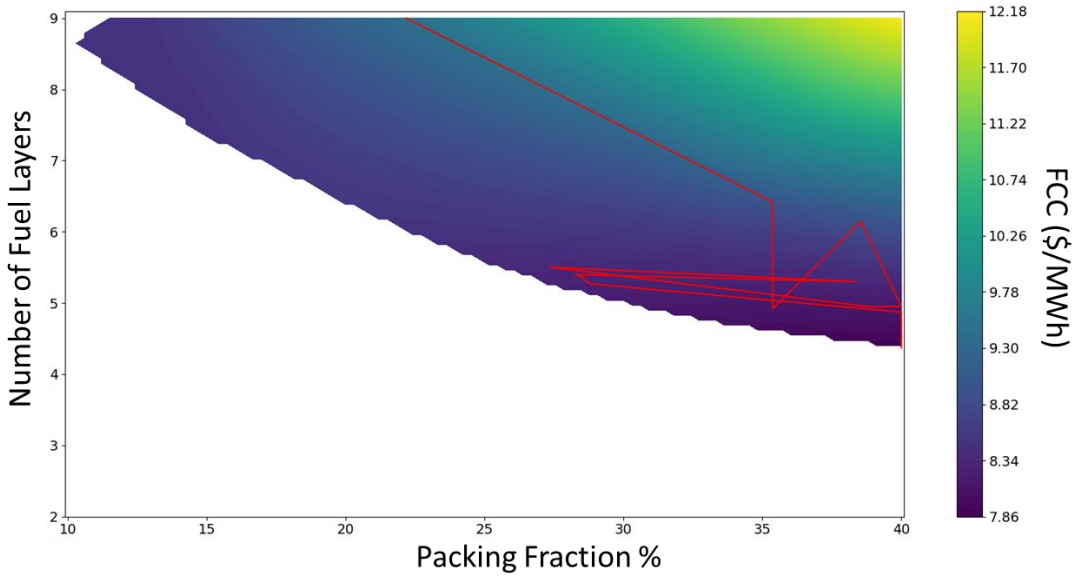

Figure 56. Convergence of the best solution over the design space and FCC with enrichment held constant at 19.75% and 3.3 batches.

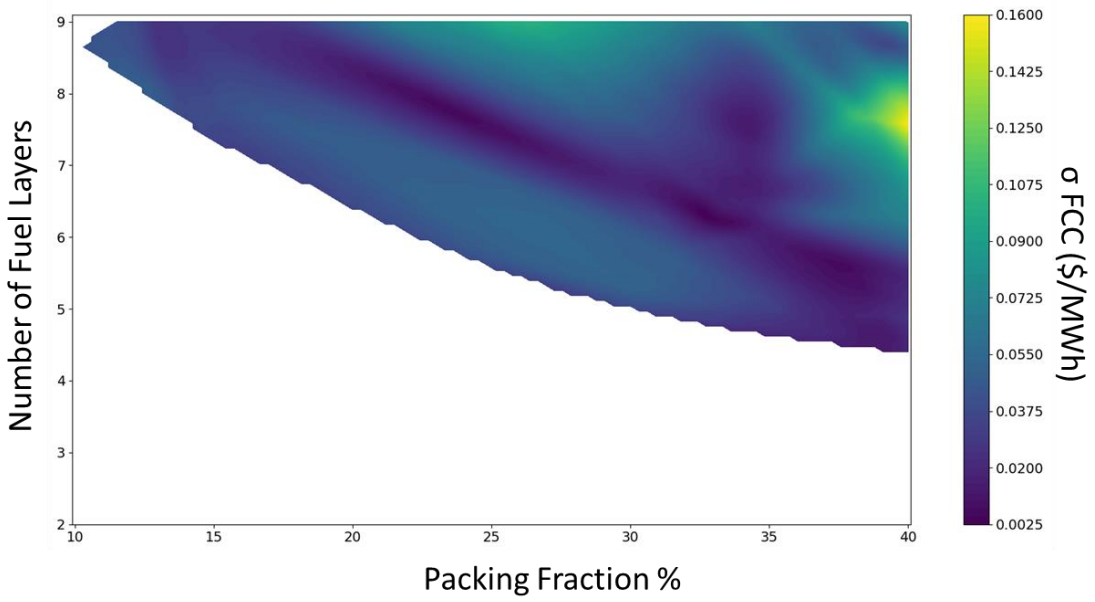

Figure 57. Standard Deviation of FCC ($/MWh) with enrichment held constant at 19.75% and 3.3 batches.

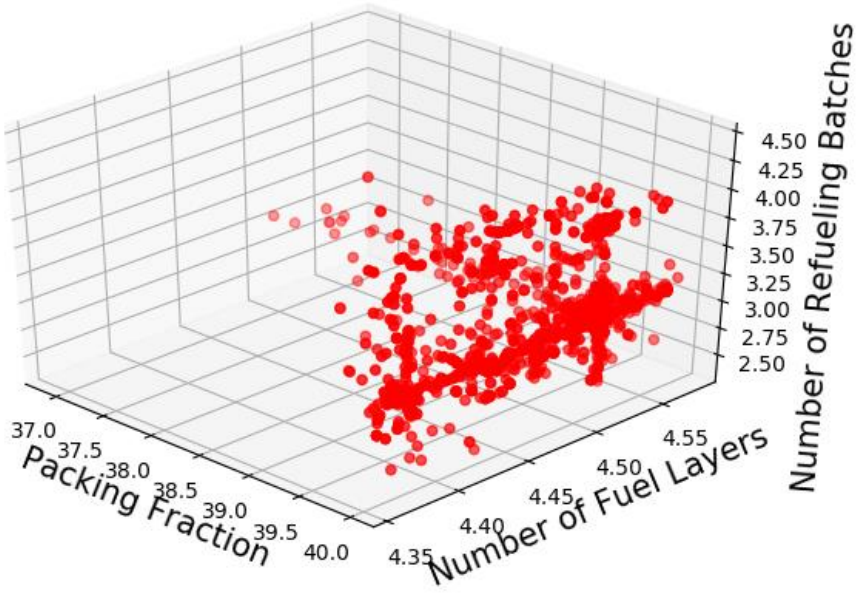

Figure 58. Solutions within 2σ of the optimal solution.

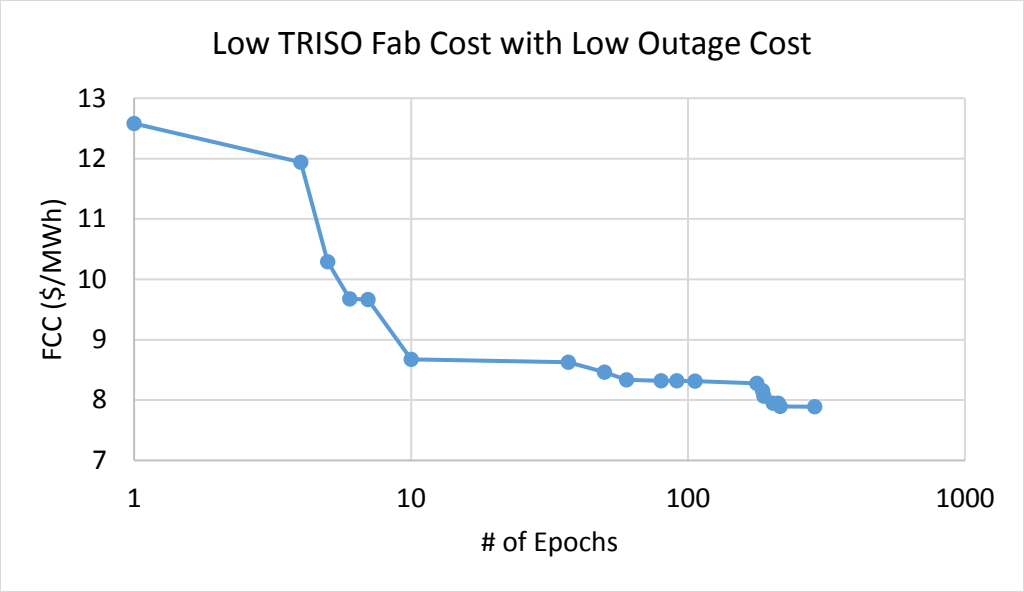

Figure 59. Convergence of optimal solution with increasing epochs.

5.2.5 High TRISO Fabrication Cost with High Outage Cost at 9% Enrichment

Due to some predictions that enrichment facilities may have difficulties in licensing enrichment over 10%, scenarios with a lower enrichment constraint on optimization are explored. The scenarios are optimized with a 9% enrichment constraint, while the other constraints are kept the same. The most pessimistic case has an optimum design with 6.77 fuel layers, 34.37% packing fraction, 9% enrichment, and a 6 batch fuel cycle. This results in a fuel cycle cost of 57.24 $/MWh. It's obvious from these results that lowering the enrichment makes the fuel cycle significantly more expensive, in particular if the TRISO fabrication cost is high. Figure 60 shows the FCC as a function of number of fuel layers and packing fraction with enrichment and number of batches held constant at 9% and 6 as well as the convergence of the best solution. Figure 61 shows the standard deviation of FCC as a function of packing fraction and number of fuel layers. Figure 62 shows the distribution of solutions within 2σ of the optimal solution. Figure 63

shows the convergence of the optimal solution. It is also apparent that lowering the enrichment significantly reduces the space within the constraints due to the more positive void coefficient.

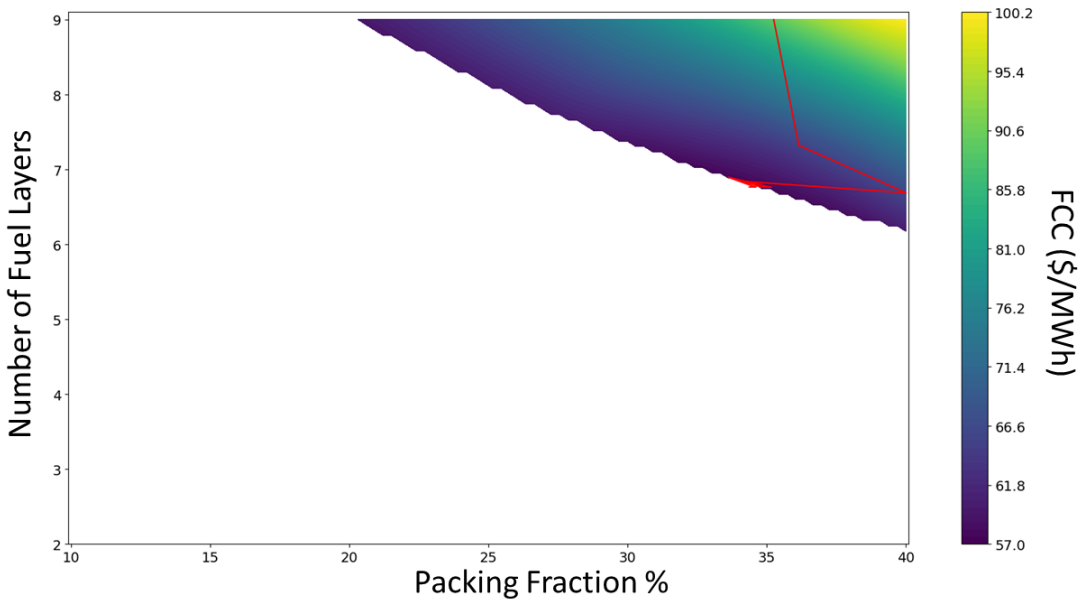

Figure 60. Convergence of the best solution over the design space and FCC with enrichment and number of batches held at 9% and 6, respectively.

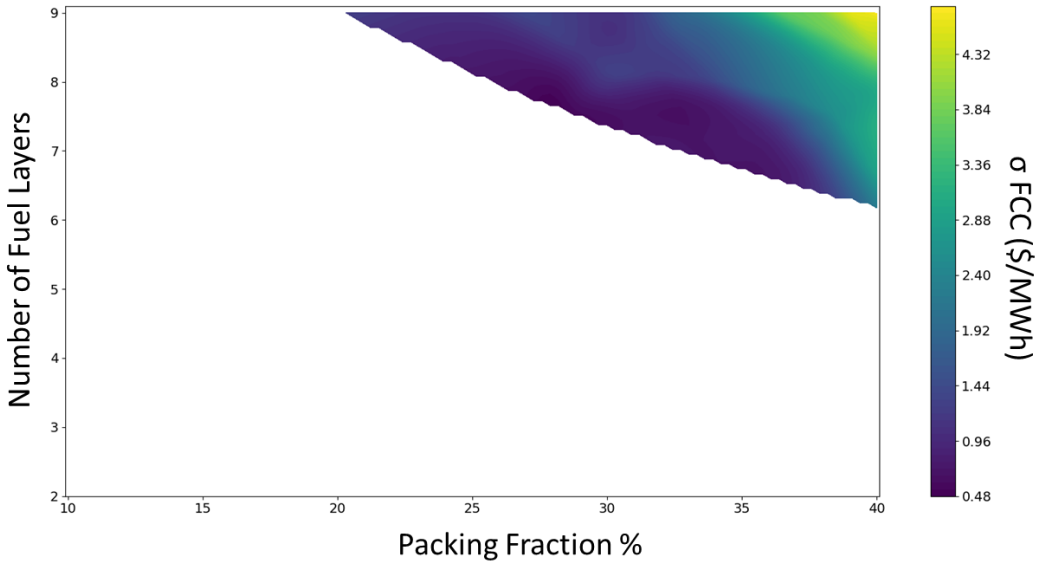

Figure 61. Standard Deviation of FCC ($/MWh) with enrichment held constant at 19.75% and 6 batches.

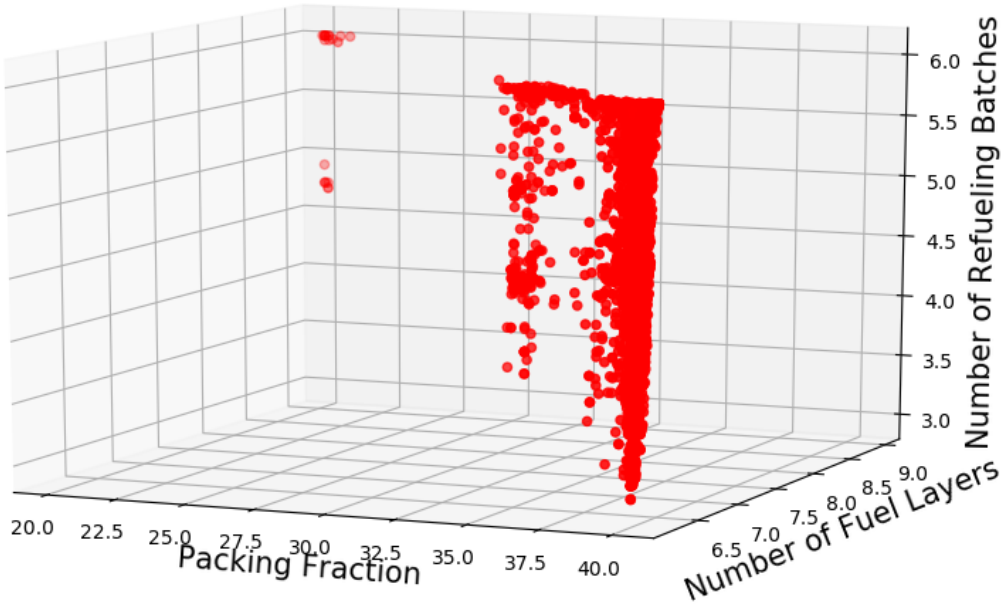

Figure 62. Solutions within 2σ of the optimal solution.

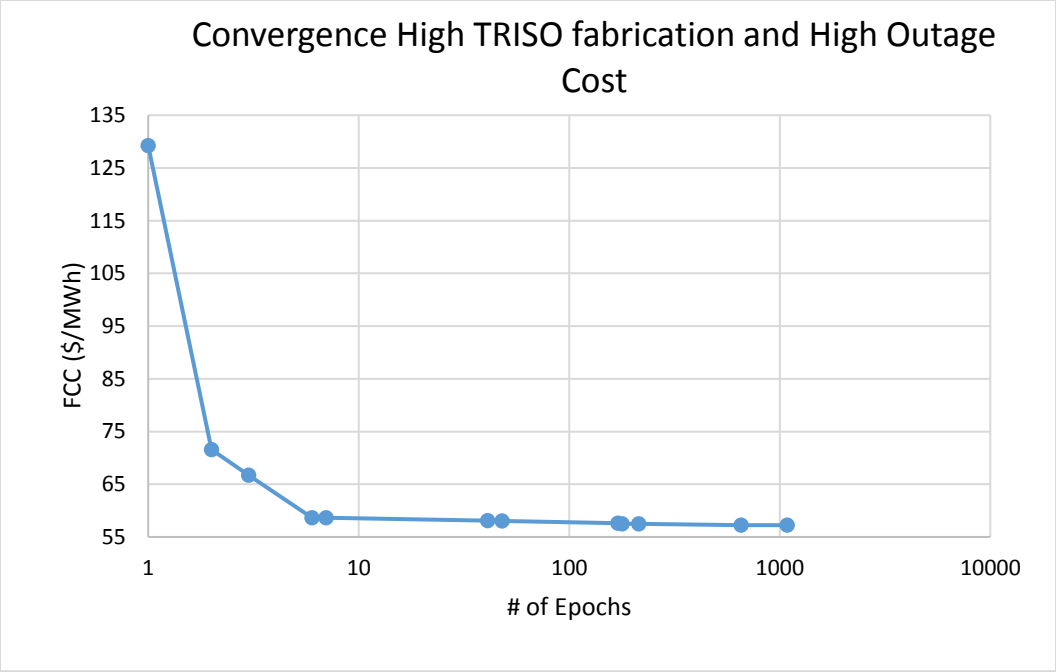

Figure 63. Convergence of the optimal solution with increasing epochs.

5.2.6 High TRISO Fabrication Cost with Low Outage Cost at 9% Enrichment

Lowering the outage cost provides a very small shift in the geometry of the design. Since the fuel utilization is much lower at 9% enrichment and the, the number of batches is against the constraint at 6 batches in the high TRISO fabrication cost scenario. The optimal design for this scenario has 6.68 fuel layers, 35.03% packing fraction, 9.00% enrichment, and 6 refueling batches. The resulting fuel cycle cost is 49.93 $/MWh. Figure 64 shows the FCC as a function of number of fuel layers and packing fraction with enrichment and number of batches held constant at 9% and 6 as well as the movement of the best solution over the design space. Figure 65 shows the standard deviation of FCC as a function of packing fraction and number of fuel layers.

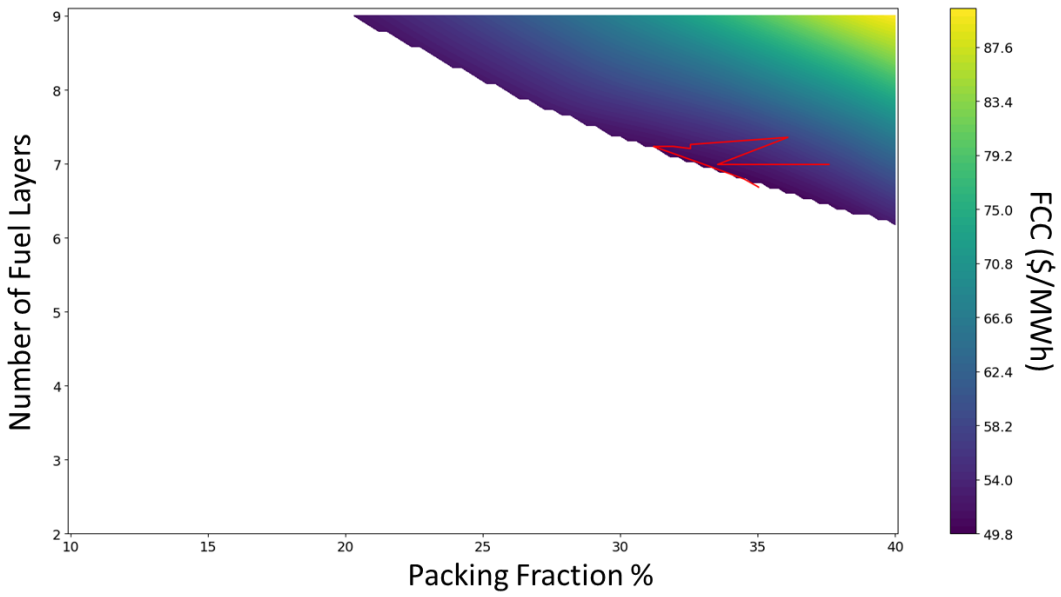

Figure 64. Convergence of the best solution over the design space and FCC with enrichment and number of batches held at 9% and 6, respectively.

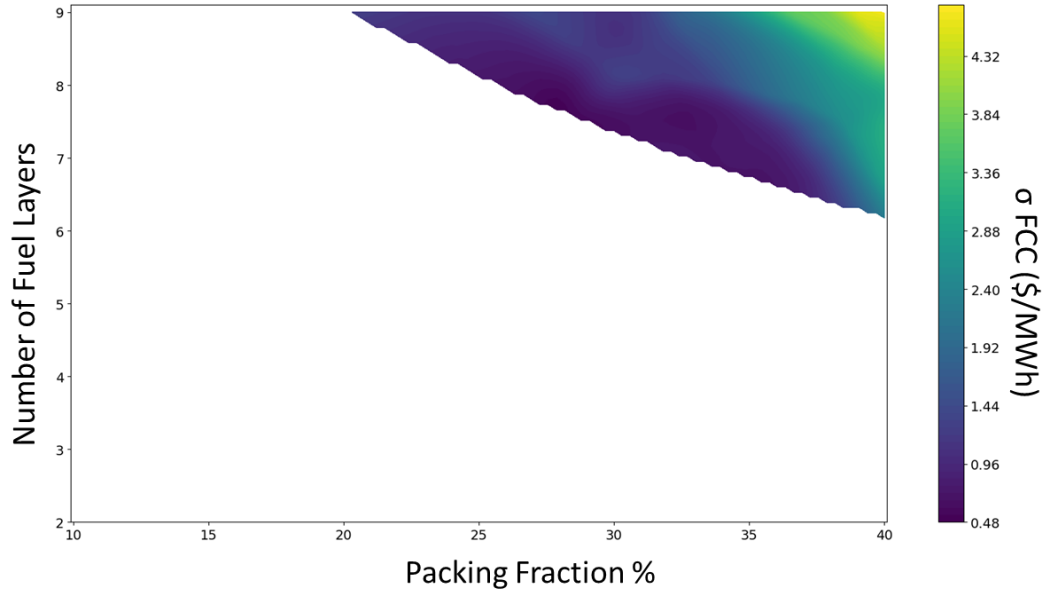

Figure 65. Standard Deviation of FCC ($/MWh) with enrichment held constant at 9% and 6 batches.

Figure 66 shows the distribution of solutions within 2σ of the optimal solution. The solutions within the confidence interval of the optimal solution are along the void coefficient constraint. As the fuel design shifts towards a higher packing fraction the near

optimal solutions appear to have less sensitivity to number of batches. Figure 67 shows the convergence of the optimal solution as a function of the number of epochs.

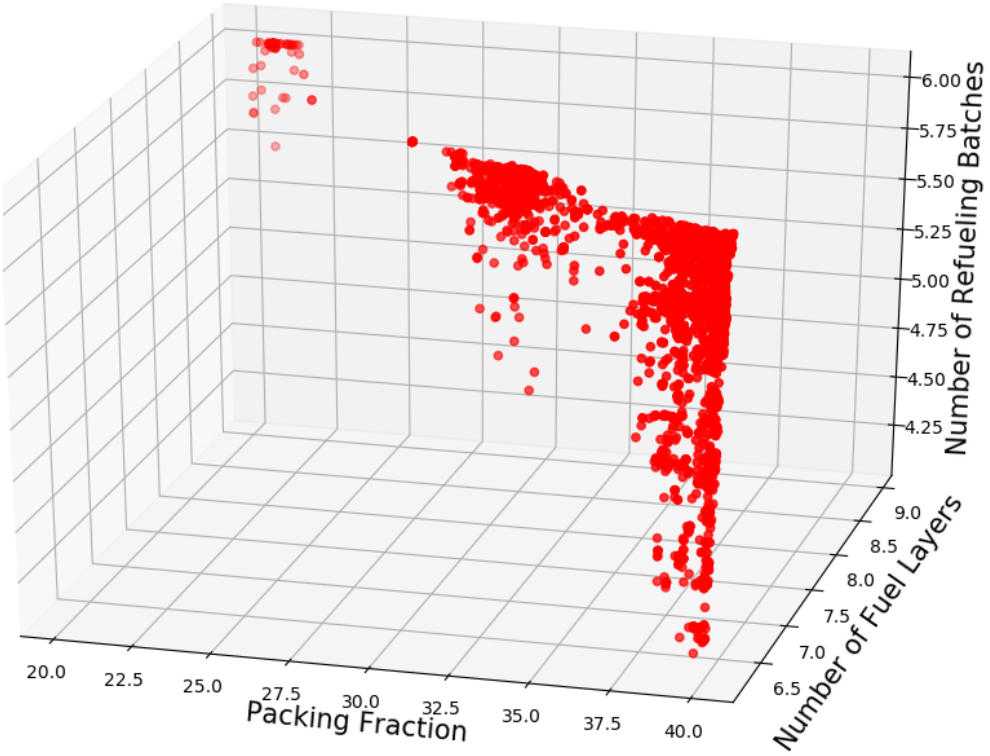

Figure 66. Solutions within 2σ of the optimal solution.

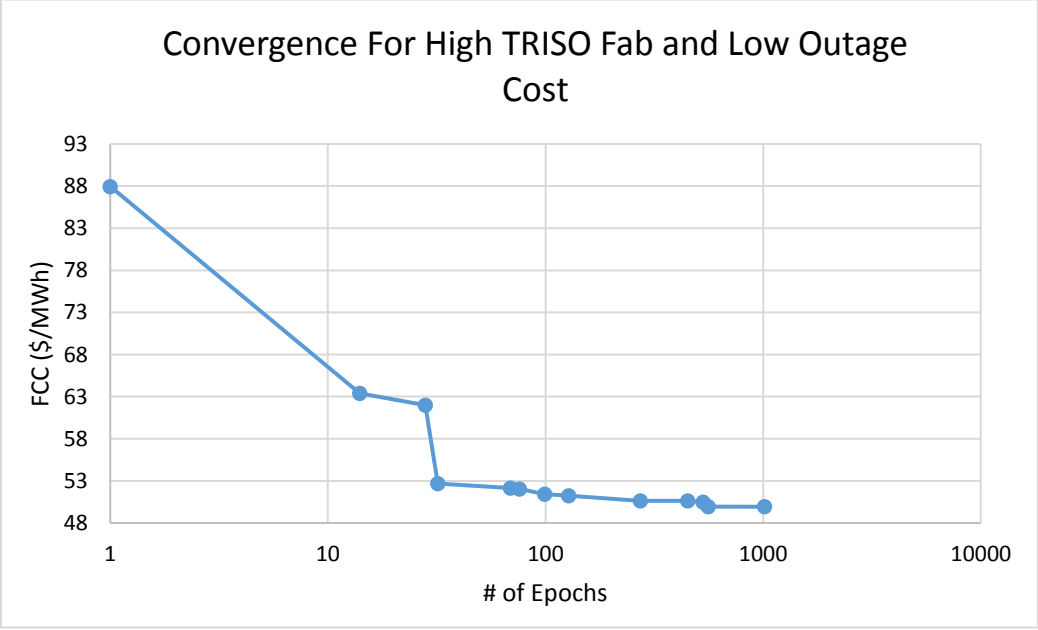

Figure 67. Convergence of optimal solution with increasing epochs.

5.2.7 Low TRISO Fabrication Cost with High Outage Cost at 9% Enrichment

An optimal fuel design with the low fabrication cost and high outage cost scenario results in a surprisingly small change to the optimal design. Only the number of refueling batches is largely changed. The optimal design has 6.58 fuel layers, 36.11% packing fraction, 9.00% enrichment, and 2.19 batches. The fuel cycle cost is predicted to be 18.91 $/MWh. Figure 68 shows the FCC over the constrained design space and the movement of the best solution as it converges to the optimum. Figure 69 shows the standard deviation of the FCC over the constrained design space. Figure 70 shows solutions that are within 2σ of the optimal solution. Nearly optimal solutions are again very close to the void coefficient constraint. In this scenario with high outage cost the sensitivity to number of batches is somewhat greater. The nearly optimal solutions mostly have a refueling scheme below 2.7 batches. Figure 71 shows the convergence of the optimal solutions as a function of number of epochs.

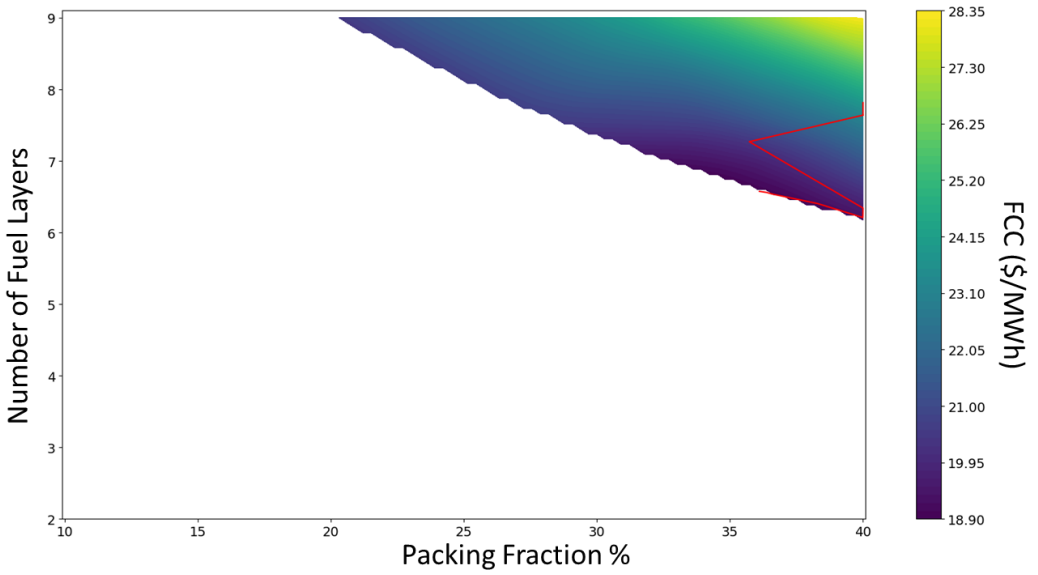

Figure 68. Convergence of the best solution over the design space and FCC with enrichment and number of batches held at 9% and 2.2, respectively.

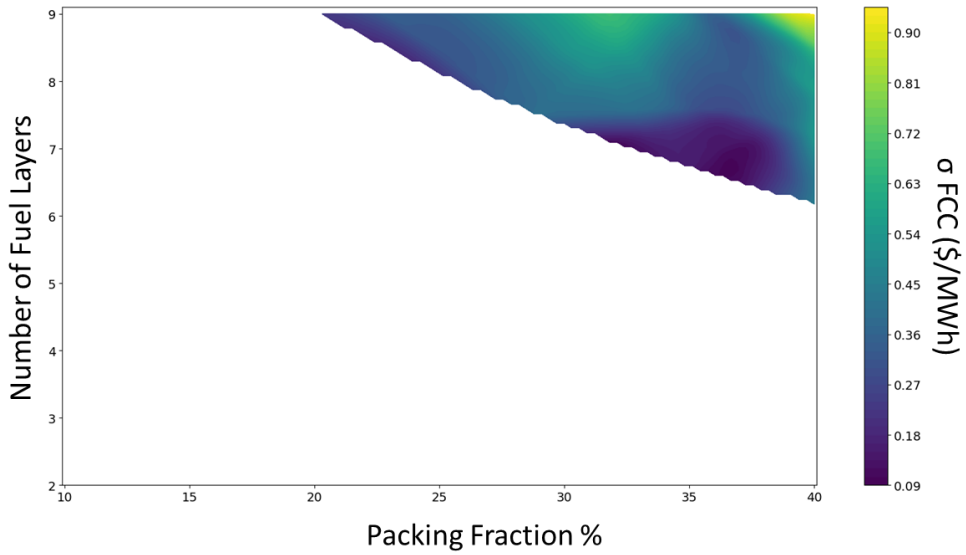

Figure 69. Standard Deviation of FCC ($/MWh) with enrichment held constant at 9% and 2.2 batches.

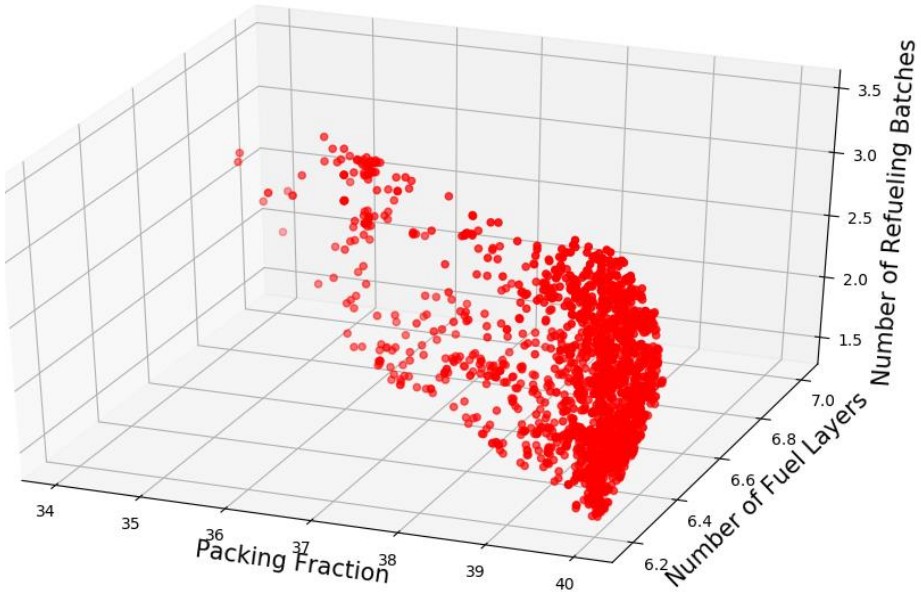

Figure 70. Solutions within 2σ of the optimal solution.

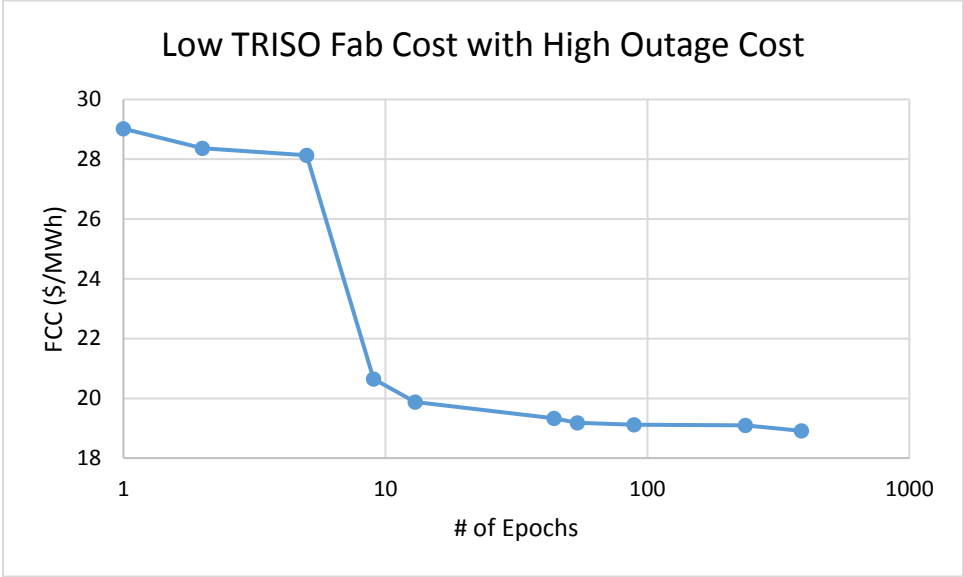

Figure 71. Convergence of optimal solution with increasing epochs.

5.2.8 Low TRISO Fabrication Cost with Low Outage Cost at 9% Enrichment

The most optimistic cost scenario with enrichment constrained to 9% gives only a very small improvement in FCC over the scenario with high outage cost. The resulting

optimal design only has a small change along the void coefficient constraint. This results in a CHM that is only slightly different. The optimal solution has 6.68 fuel layers, 35.06% packing fraction, 9.00% enrichment, and a 2.42 batch fuel cycle. Figure 72 shows the FCC over the constrained design space and the movement of the best solution as it converges to the optimum. Figure 73 shows the standard deviation of the FCC over the constrained design space. Figure 74 shows solutions that are within 2σ of the optimal solution. Nearly optimal solutions are once again very close to the void coefficient constraint. Solutions with low TRISO fabrication cost at 9% enrichment lead to a higher sensitivity to number of batches and to fewer batches of refueling. The nearly optimal solutions mostly have a refueling scheme below three batches. Figure 75 shows the convergence of the optimal solutions as a function of number of epochs.

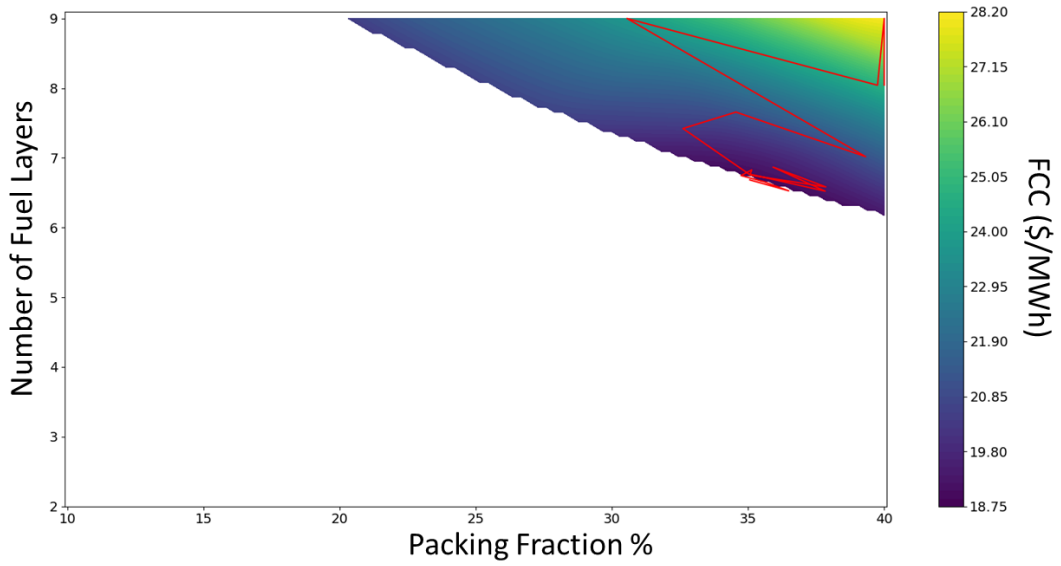

Figure 72. Convergence of the best solution over the design space and FCC with enrichment and number of batches held at 9% and 2.4, respectively.

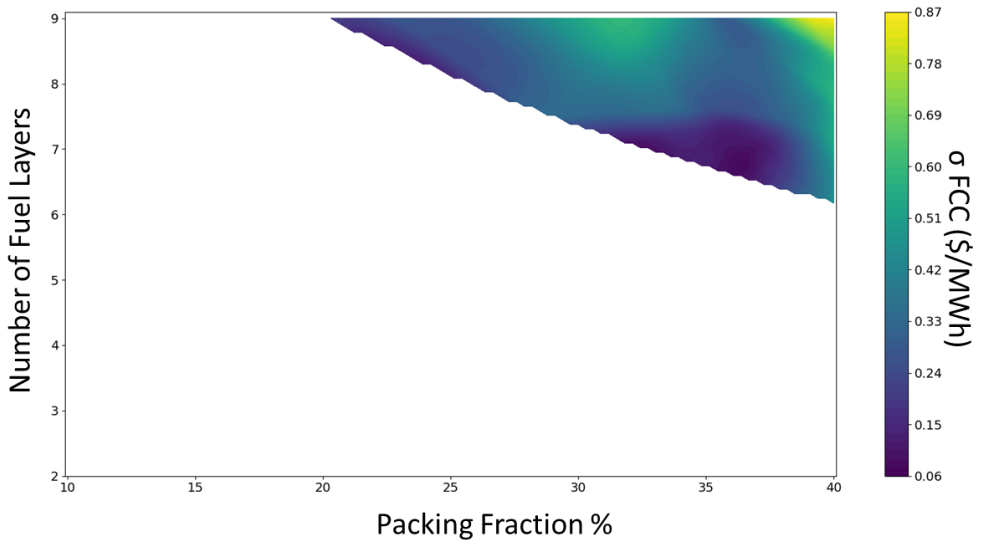

Figure 73. Standard Deviation of FCC ($/MWh) with enrichment held constant at 9% and 2.4 batches.

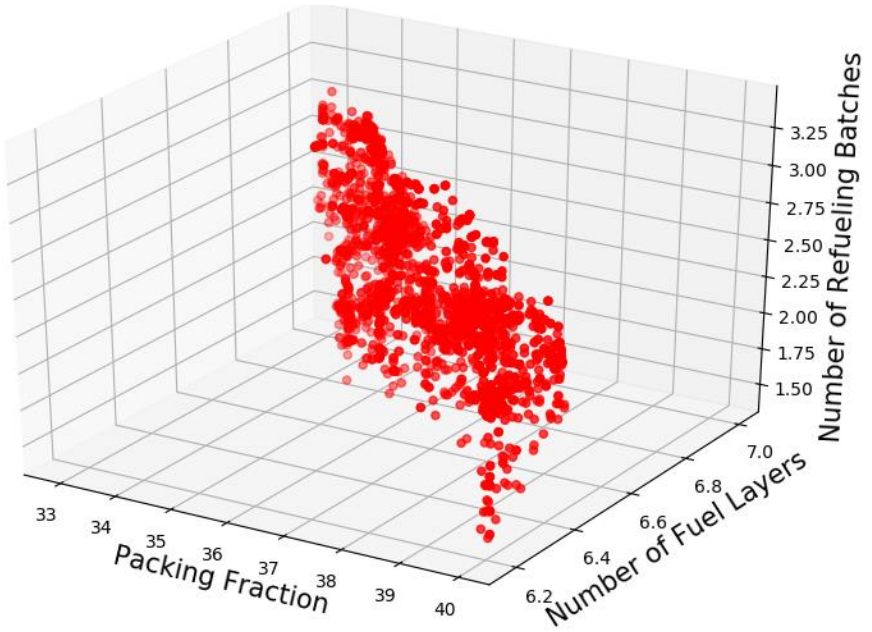

Figure 74. Solutions within 2σ of the optimal solution.

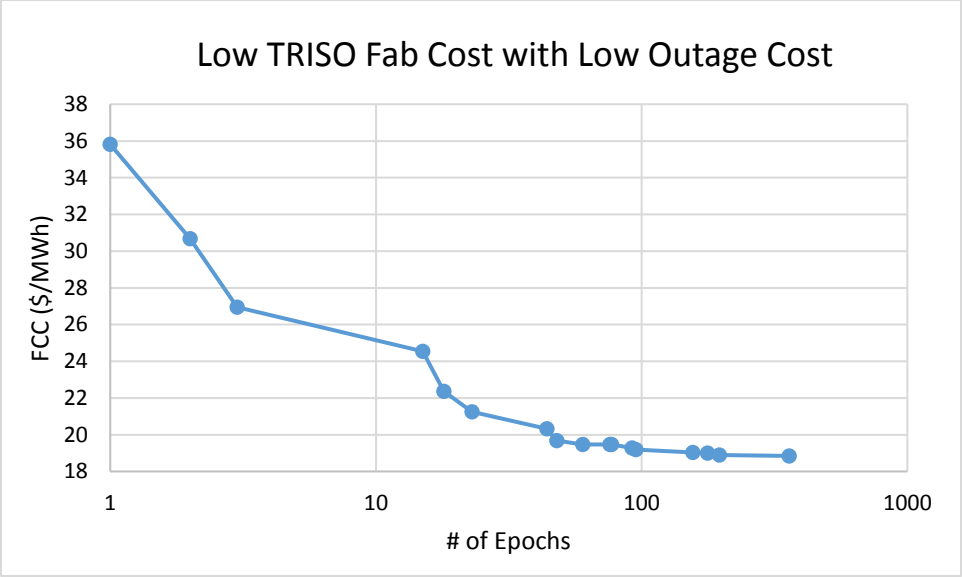

Figure 75. Convergence of optimal solution with increasing epochs.

5.2.9 Comparison of Optimization of Cost Scenarios

A major change in the cost of TRISO manufacturing or outage costs does not have a large impact on the geometry or composition of the fuel plank design. It does significantly change the optimal reloading scheme. However, the results from the different scenarios show that the FCC is not very sensitive to the number of batches at 19.75% enrichment. While the optimal number of batches change significantly, the FCC does not change much with a suboptimal number of batches. It becomes more sensitive as enrichment is lowered due to the lower fuel utilization. Since this study does not take into account seasonal cost effects the utility company would benefit most from choosing a refueling scheme that is most convenient for them, especially if 19.75% enrichment is feasible. At lower enrichment the fuel cycle cost is more sensitive to the reloading scheme and has a fairly large impact on cycle length and fuel utilization. Both 19.75%

and 9% enrichment constraint lead to a larger number of batches compared to a typical LWR fuel cycle with the high TRISO fabrication cost scenario.

Overall having the enrichment constrained to 19.75% results in much better fuel utilization and a lower fuel cycle cost. Since FHR fuel is robust with regards to high burnup, it is more practical from a technical and economic standpoint to use 19.75% enrichment. Clearly from the results only a policy argument could be made against using 19.75%. Table 12 shows a comparison of the different cost scenarios.

Table 12. Comparison of optimal solutions for FCC scenarios.

Scenarios with 19.75% Enrichment Constraint							
Scenario	# of FL	PF %	EN %	# of BA	FCC ($/MWh)	CL (FPD)	BU (MWd/tHM)
HighT_HighO	4.39	39.83	19.75	4.48	23.46	286	200512
HighT_LowO	4.42	38.63	19.75	5.96	20.37	233	217572
LowT_HighO	4.36	40.00	19.75	2.23	9.61	527	181782
LowT_LowO	4.36	40.00	19.75	3.26	7.89	388	195220
Scenarios with 9% Enrichment Constraint							
HighT_HighO	6.67	34.37	9.00	6.00	57.24	114	76779
HighT_LowO	6.68	35.03	9.00	6.00	49.93	114	75361
LowT_HighO	6.58	36.11	9.00	2.19	18.91	238	57304
LowT_LowO	6.68	35.06	9.00	2.42	18.85	223	59453

5.2.10 Comparison of Cost Scenarios without the Void Coefficient Constraint

It is expected that the void coefficient constraint is too conservative, and therefore limits the optimal design too much. While it would possibly be required under current regulatory environments it would not be practical for designs with 9% enrichment. Generally the positive "void coefficient," which in this case has nothing to do with boiling, would only have an effect under extremely catastrophic scenarios involving significant structural damage. Optimization calculations were performed for all previous

scenarios using the power reactivity coefficient and geometry constraints. The result is far less limiting although a more in depth safety analysis is necessary to understand the exact limitations of the design.

The first scenario with 19.75% enrichment, which assumes high TRISO and high outage cost shows a slight reduction in FCC compared to the void coefficient limited optimization calculation. The optimal solution for this scenario has 3.83 fuel layers, 34.67% packing fraction, 19.75% enrichment, and 2.84 batches. This results in a FCC of 22.39 $/MWh. It can be seen that solutions along the same CHM line of the optimal solution have a similar FCC. It can be seen from Figure 76, which shows the FCC as well as the convergence of the optimal solution over the design space, that the power coefficient of reactivity is not limiting over the design space. This is expected since in Chapter 3 it was shown that the power reactivity coefficient is negative over the design space. This results in an optimal result with a significantly lower CHM.

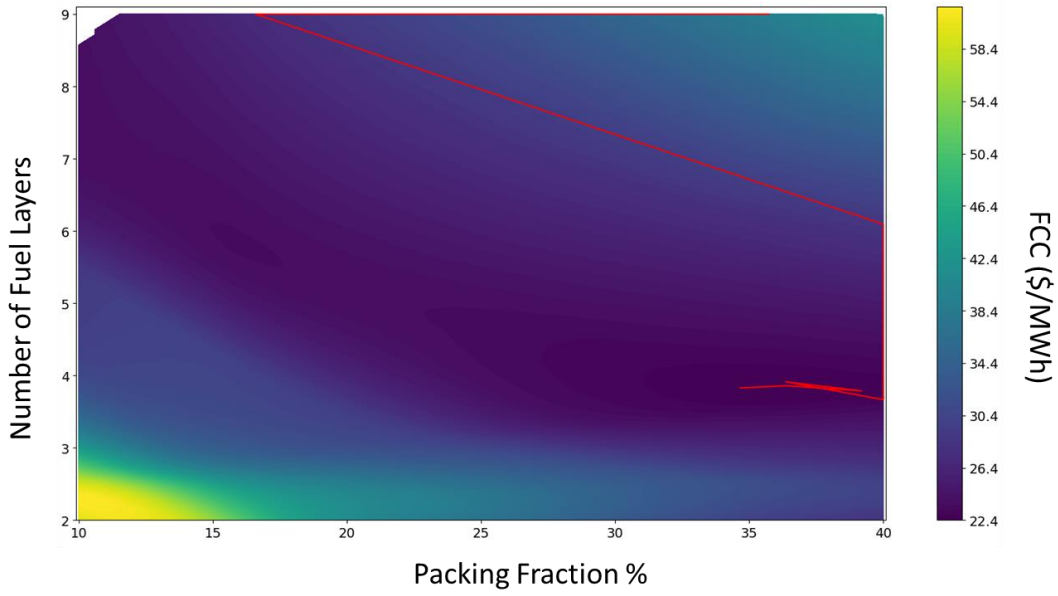

Figure 76. FCC and Optimal FCC convergence over the design space at 19.75% enrichment with batches held constant at 2.8 for the high TRISO and high outage cost scenario.

The low outage cost with high TRISO cost scenario shows a modest improvement in FCC when not bound by the void coefficient constraint. The FCC decreases to 19.64 $/MWh, from 20.37 $/MWh. The resulting optimal design has 3.91 fuel layers, 34.56% packing fraction, 19.75% enrichment, and 5.35 batches. This is only a small change from when the design is constrained by the void coefficient. Figure 77 shows the FCC and convergence of the optimal solution over the design space.

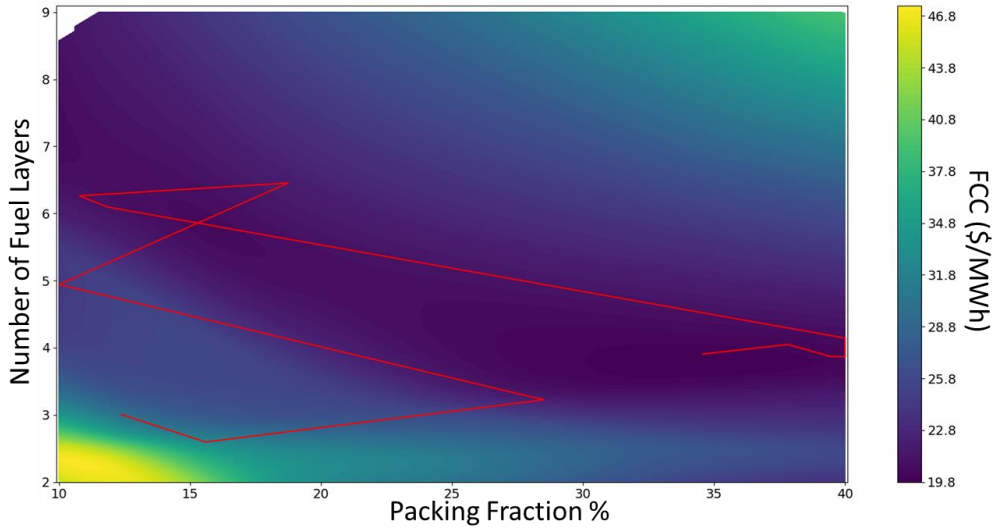

Figure 77. FCC and Optimal FCC convergence over the design space at 19.75% enrichment with batches held constant at 5.3 for the high TRISO and low outage cost scenario.

Lowering the TRISO manufacturing cost results in a large reduction in FCC. However, removing the void coefficient constraint only has a small effect on FCC and the resulting optimal design. In this case, the optimal design has 3.98 fuel layers, 40% packing fraction 19.75% enrichment, and 2.14 batches. The optimal FCC is 9.52 $/MWh. The design only has a slightly thinner fuel stripe compared to the design constrained by

the void coefficient. Figure 78 shows the FCC and convergence of the optimal solution over the design space.

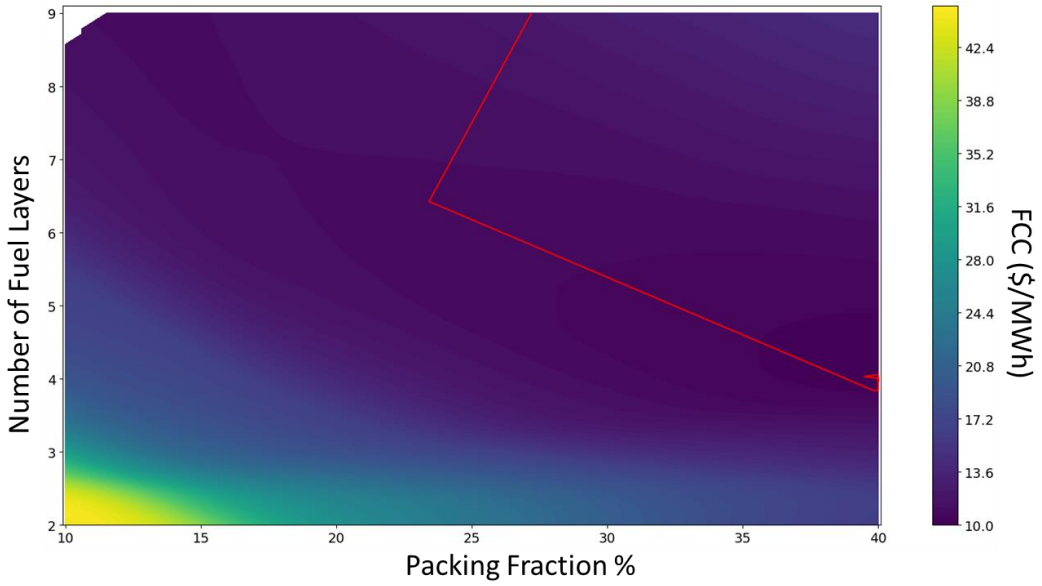

Figure 78. FCC and Optimal FCC convergence over the design space at 19.75% enrichment with batches held constant at 2.1 for the low TRISO and high outage cost scenario.

The most optimistic cost scenario, with low TRISO and outage costs is also minimally effected by the void coefficient constraint at 19.75% enrichment. The resulting optimal design has 3.97 fuel layers, 39.76% packing fraction, 19.75%, and 2.88 batches. This design gives a FCC of 7.80 $/MWh, only 9 ₵/MWh less than with the void coefficient constraint. Figure 79 shows the FCC and optimal solution convergence over the design space.

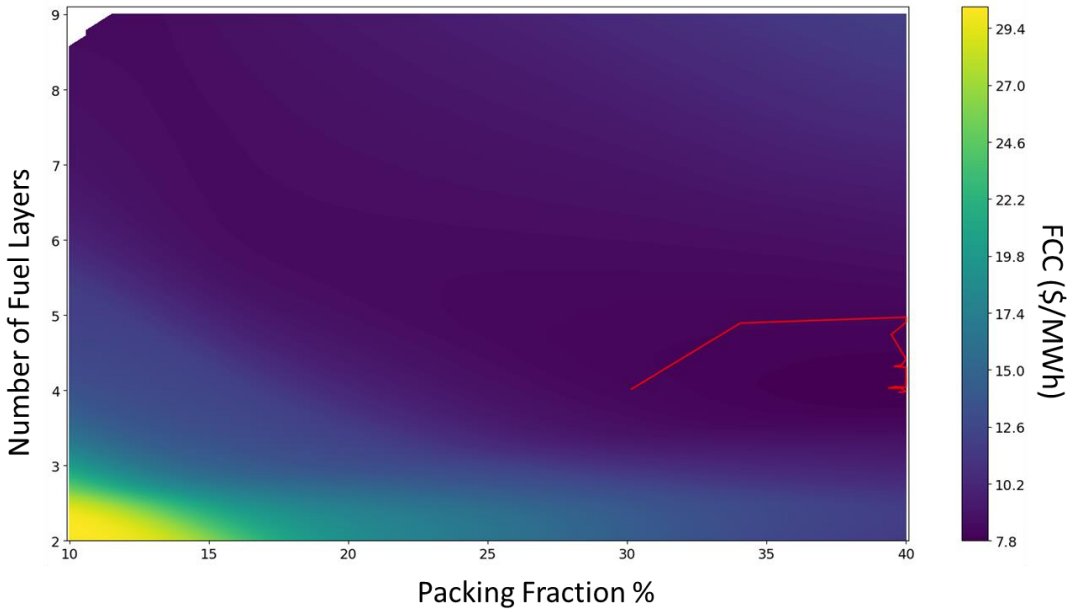

Figure 79. FCC and Optimal FCC convergence over the design space at 19.75% enrichment with batches held constant at 2.9 for the low TRISO and low outage cost scenario.

At lower enrichments, optimization without the void coefficient constraint results in a large improvement in optimal FCC. The most pessimistic cost scenario at 9% enrichment results in a FCC of 42.93 $/MWh, almost 15 $/MWh less than when constrained by the void coefficient. The optimal design has 3.58 fuel layers, 33.84% packing fraction, 9.00% enrichment, and 3.94 batches. This gives a CHM of 455, compared to only 239 CHM when the optimum is constrained by the void coefficient. However, at 9% enrichment the FCC is still almost twice as high compared to the design with 19.75% enrichment assuming high TRISO and outage costs. Figure 80 shows the FCC and optimal design convergence over the design space.

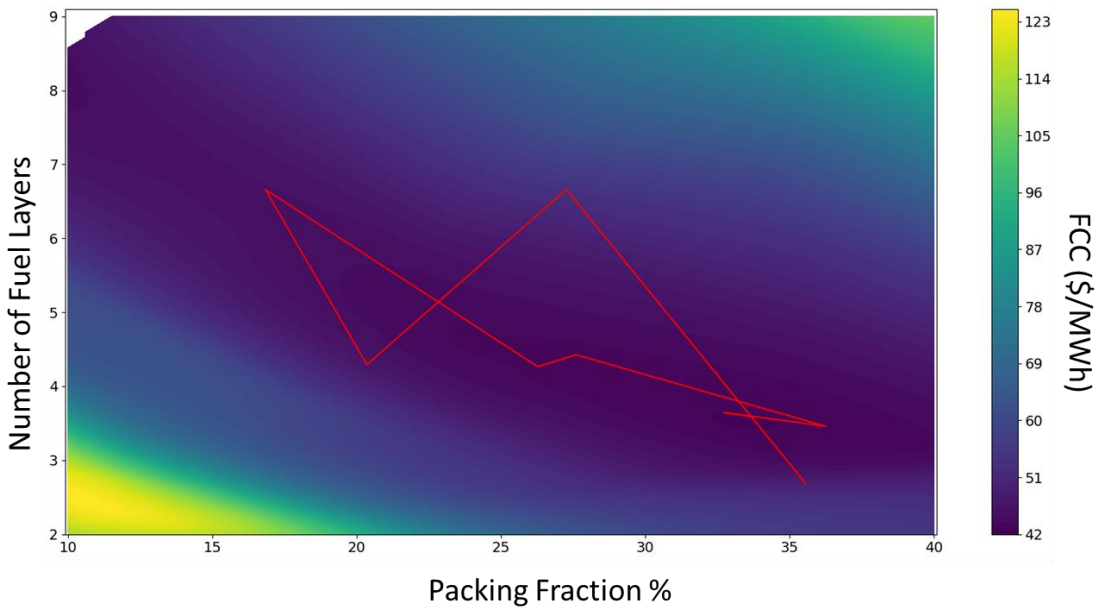

Figure 80. FCC and Optimal FCC convergence over the design space at 9% enrichment with batches held constant at 3.9 for the high TRISO and high outage cost scenario.

The scenario with lower outage cost at 9% enrichment results in a slightly lower FCC as expected. The design remains mostly the same but again the fuel cycle increases to a six batch fuel cycle. The resulting optimal fuel design has 3.78 fuel layers, 34.84% packing fraction, and 9% enrichment. Figure 81 shows the FCC and convergence of the optimal solution over the design space.

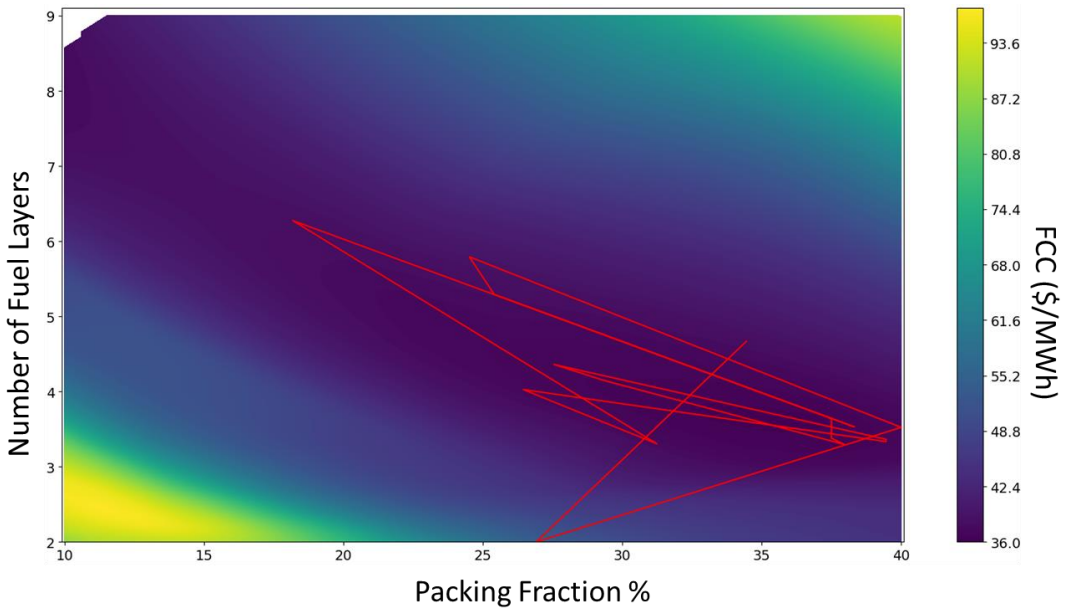

Figure 81. FCC and Optimal FCC convergence over the design space at 9% enrichment with batches held constant at 6 for the high TRISO and low outage cost scenario.

The low TRISO cost with high outage cost scenario at 9% enrichment does not improve much by removing the void coefficient constraint. The short cycle length at lower enrichment limits the optimal solution. Still, the TRISO particle manufacturing cost has a very significant impact on FCC, reduced by more than half. The optimal design for this scenario has 4.86 fuel layers, 31.91% packing fraction, 9% enrichment, and 1.87 batches. This results in a FCC of 16.64 $/MWh. Figure 82 shows the FCC and convergence of the optimal solution over the design space.

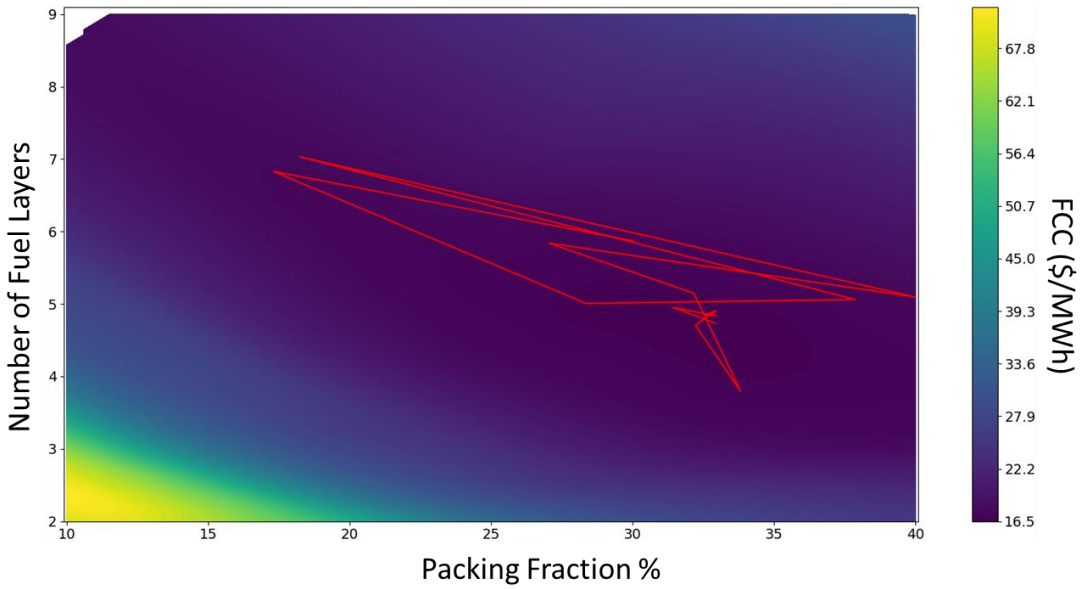

Figure 82. FCC and Optimal FCC convergence over the design space at 9% enrichment with batches held constant at 6 for the low TRISO and high outage cost scenario.

The most optimistic cost scenario at 9% enrichment greatly benefits from removal of the void coefficient constraint. Lower outage costs make the shorter cycle length less detrimental to the FCC, resulting in improved fuel utilization via high CHM. This scenario actually has a FCC comparable to the 19.75% enrichment. The optimal design has 4.52 fuel layers, 34.94% packing fraction, 9% enrichment, and 3.21 batches. Figure 83 shows FCC and the convergence of the optimal solution over the design space.

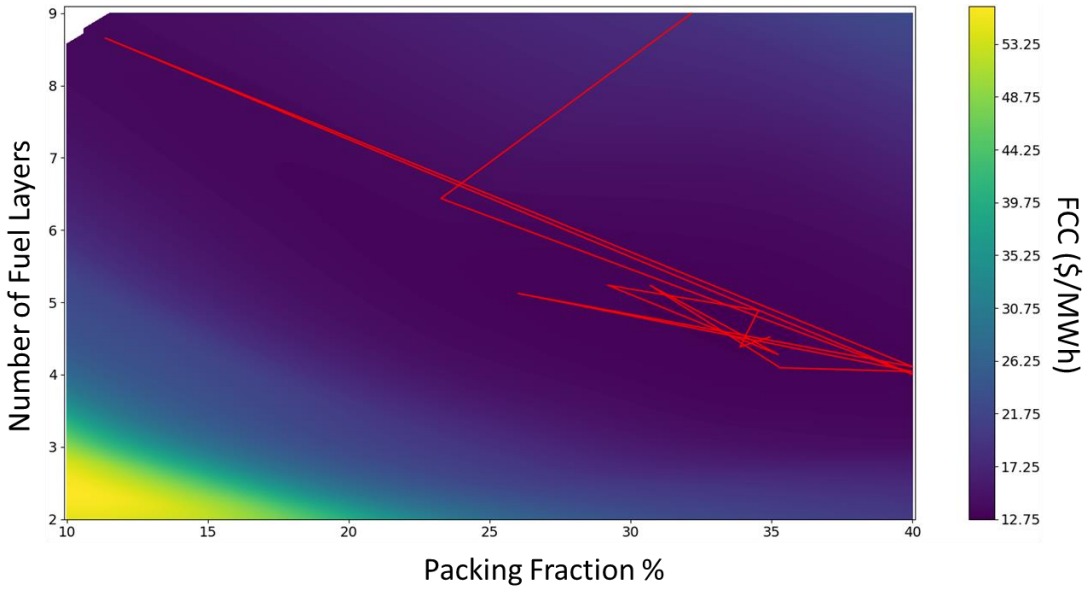

Figure 83. FCC and Optimal FCC convergence over the design space at 9% enrichment with batches held constant at 6 for the low TRISO and low outage cost scenario.

Overall, when the void coefficient constraint is removed the cost scenarios result in optimal fuel designs with similar geometry. Comparatively, at 9% enrichment the optimal designs are very limited by the void coefficient constraint, resulting in designs that have a much lower CHM. In all scenarios the FCC benefits from only considering the power coefficient as a safety constraint and not including the void coefficient constraint.

The optimal designs are significantly affected by the TRISO manufacturing cost. At both enrichments the scenario with high TRISO manufacturing cost and low outage cost results in designs that favor higher fuel utilization over longer cycle length. The optimal geometry differs more between enrichments for the low TRISO cost scenarios. These scenarios produce an optimal fuel stripe thickness (more fuel layers) that is thicker and has a lower packing fraction at 9% enrichment compared to 19.75% enrichment. This

shift is perhaps due to increased resonance absorption in the lower enriched fuel. Table 13 shows a comparison of optimal designs with different cost scenarios with the void coefficient constrain is removed.

These results show that the future regulatory environment and uranium enrichment infrastructure will be very important in determining the AHTR's economics. The eventual design's FCC could be significantly impacted by efforts to upgrade enrichment facilities and modernize NRC design regulations for Gen IV reactors. If TRISO manufacturing costs are high, it may be more important to upgrade enrichment infrastructure for 19.75% enriched uranium production. Assuming TRISO fuel costs are low then higher enrichment is less important, but constraining the optimal design by an archaic definition of the void coefficient would have a larger impact. A high fidelity CE depletion calculation was performed to verify the FCC surrogate model. The CE depletion calculation gave a difference in cycle length of about 7 days, which corresponds to a change in burnup of about 1000 MWd/tHM and a change in FCC of .15 $/MWh.

Table 13. Comparison of optimal designs with different cost scenarios with the void coefficient constraint removed.

Scenarios with 19.75% Enrichment Constraint							
Scenario	# of FL	PF %	EN %	# of BA	FCC ($/MWh)	CL (FPD)	BU (MWd/tHM)
HighT_HighO	3.83	34.67	19.75	2.84	22.39	389	214528
HighT_LowO	3.91	34.56	19.75	5.35	19.64	230	233826
LowT_HighO	3.98	40.00	19.75	2.14	9.52	527	191571
LowT_LowO	3.97	39.76	19.75	2.88	7.80	416	204300
Scenarios with 9% Enrichment Constraint							
HighT_HighO	3.58	33.84	9.00	3.94	42.93	137	113550
HighT_LowO	3.78	34.84	9.00	6.00	36.44	101	118670
LowT_HighO	4.86	31.91	9.00	1.87	16.64	267	80347
LowT_LowO	4.52	34.94	9.00	3.21	12.95	179	93851

CHAPTER 6

CONCLUSION

This research has demonstrated an advanced methodology for modeling and optimizing the neutronic design of the AHTR fuel assembly. Starting from a high fidelity CE Monte Carlo Transport model, approximations are chosen for practical execution of parametric studies. Supporting data for temperatures, leakage correction factors, and cost models are integrated into the methodology to improve the accuracy of the model. Artificial neural networks are then used to generate surrogate models over the design space in order to perform accurate optimization over a continuous function in a practical amount of time. A novel global heuristic optimization algorithm Preferred Neighborhood Aggregation (PNA) was developed to search for the optimal solution and to characterize the area of solutions that are near optimal. This optimization approach was used for several different cost scenarios and was able to show how changing the assumed major costs would affect the optimal solution.

The results demonstrate that changes in major external cost factors do not significantly change how the optimal fuel would be manufactured. The TRISO fabrication cost, however, does significantly affect the optimal reloading scheme as the balance of the fuel cycle cost shifts more toward favoring better fuel utilization or a longer cycle length. The void coefficient constraint generally seems to shift the optimal solution to a lower CHM. As the enrichment constraint is decreased from 19.75% to 9% enrichment the optimal solution is shifted to an even lower CHM by the void coefficient constraint, leading to poorer performance. However, when the design optimization is

constrained only by the power reactivity coefficient the resulting designs at 9% enrichment are similar to designs at 19.75% enrichment. The FCC is even comparable when assuming the TRISO particle manufacturing cost is lower. It seems that the design's economics would benefit from an effort to modernize NRC design regulations to be relevant for FHR physics. Upgrading enrichment capabilities to 20% would also help, but may or may not be financially justified depending on the regulatory environment for Gen IV reactors and the cost of manufacturing TRISO particles.

The methodology presented is significant because it enables the efficient use of computational resources for rigorous design optimization. This approach effectively mitigates the shortcomings that extremely long neutronics simulation runtimes impose on the design process. While artificial intelligence has been used before for nuclear engineering design applications, this is to the best of our knowledge the first attempt to apply neural networks to assist in the design of the AHTR fuel. This approach also brings additional benefit in its ability to characterize the region of near optimal solutions to give further understanding of how sensitive the optimal solution is to small changes in external costs.

It is recommended that future work more precisely explore the TRISO fuel manufacturing cost. This would narrow the fuel cycle cost uncertainty and provide more understanding of how the future regulatory environment would affect economics. Also, more in depth full core calculations would provide a more accurate physics model for design optimization. Rigorous safety analysis is needed to understand the relevance of the "void coefficient" as it pertains to the AHTR as a constraint in accident scenarios.

APPENDIX A. EFFECTS OF UPDATED PLANK CARBON DENSITY

The calculations in this research are based on the 2011 design specifications [13]. Since then, the design has been updated to have thicker sintered carbonaceous material in the fuel planks. The feasible density has been updated to 1.75 g/cc from 1.59 g/cc [33]. 2D fuel assembly depletion calculations were performed to assess the effect of changing the plank carbonaceous density from 1.59 g/cc to 1.75 g/cc and 1.9 g/cc. These calculations were completed to understand the change in cycle length by updating design specifications from what was used in this dissertation. Figure 84 shows a plot of depletion calculations comparing K_{inf} of different fuel plank carbon densities over the cycle length for a packing fraction of 40%. Figure 85 also shows a plot of K_{inf} same as the previous figure, but with 20% packing fraction. Table 14 compares the results at approximately EOC for the two packing fractions. The results show that as the carbon density in the fuel planks increases cycle length increases. At 40% packing fraction the change in cycle length from 1.59 g/cc to 1.75 g/cc is smaller compared to the change in cycle length at 20% packing fraction design. This corresponds to an increase in cycle length of approximately 50 FPDs at 40% packing fraction and approximately 75 FPDs at 20% packing fraction.

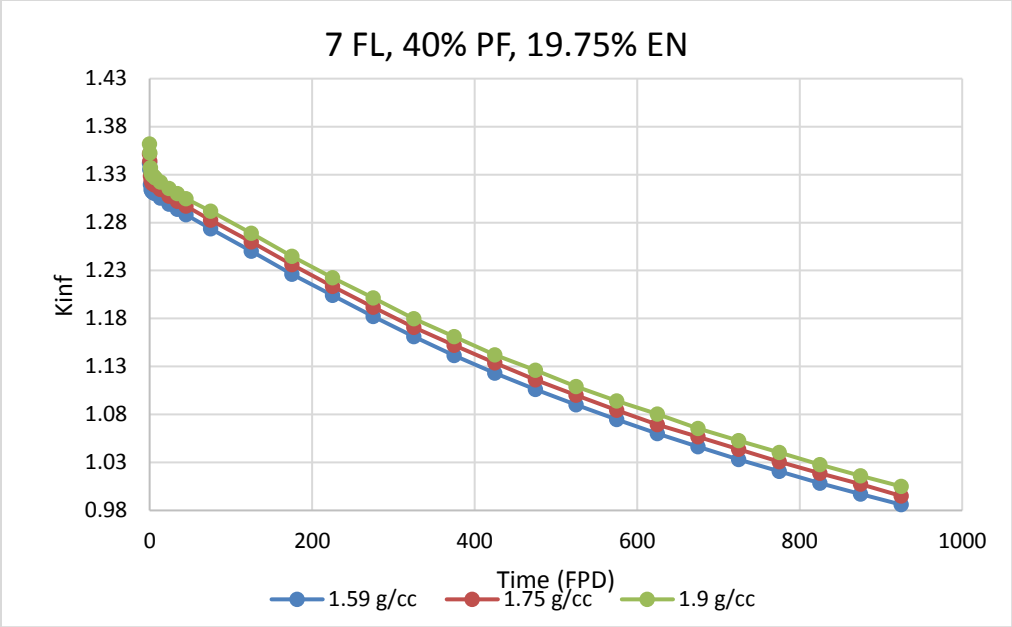

Figure 84. 2D Fuel assembly depletion calculations comparing performance of planks with different carbonaceous density for a design with 7 FL, 40% PF, and 19.75% EN.

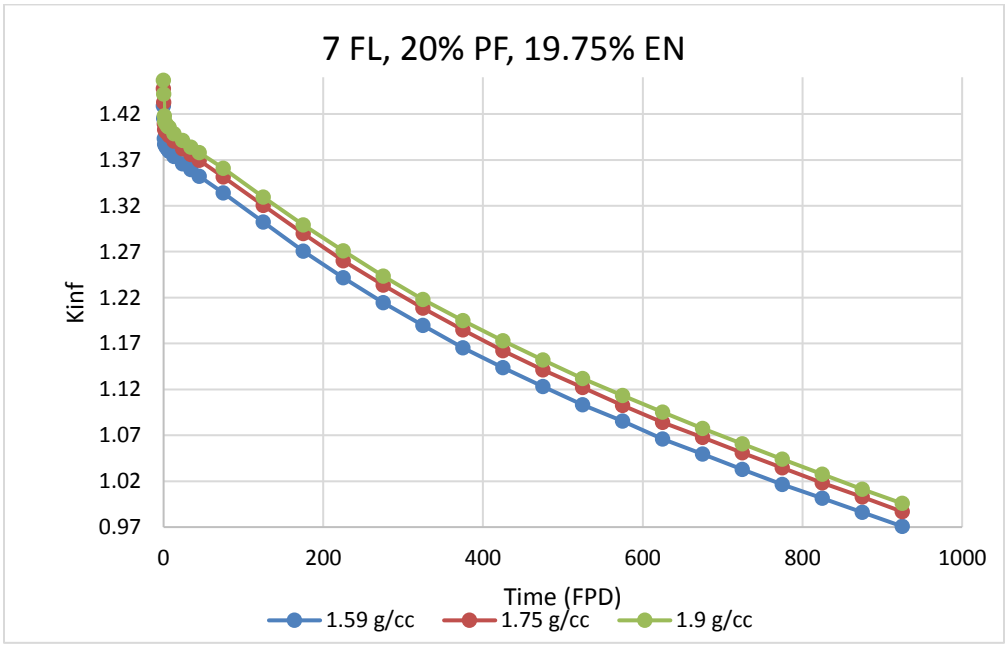

Figure 85. 2D Fuel assembly depletion calculations comparing performance of planks with different carbonaceous density for a design with 7 FL, 20% PF, and 19.75% EN.

Table 14. Comparison of ΔK_{inf} at approximate EOC for different fuel plank carbonaceous material densities.

4 FL, 40% PF, 19.75% EN	
C Density	Δkinf (pcm) at 875 FPD
1.59 g/cc	0
1.75 g/cc	1025
1.9 g/cc	1882
4 FL, 20% PF, 19.75% EN	
C Density	Δkinf (pcm) at 875 FPD
1.59 g/cc	0
1.75 g/cc	1687
1.9 g/cc	2515

Another set of calculations was performed to see the effect of changing fuel plank carbon density at lower enrichment. Figure 86 shows K_{inf} over the cycle length for two different densities at 40% packing fraction and 9% enrichment. It appears that the effect is smaller when enrichment is lowered to 9% from 19.75% compared to decreasing the packing fraction from 40% to 20%. The difference in K_{inf} between plank carbon densities of 1.59 g/cc and 1.9 g/cc at near EOC is about 2000 pcm. This corresponds to an increase in cycle length of approximately 50 FPDs. It can be concluded from these results that the updated design specifications would lead to a significant performance increase compared to the final optimization results presented in this dissertation. However, it does not appear to change the overall trend shown in the optimization results. The optimal results would be shifted only slightly assuming the CHM is increased by a small amount over the whole design space.

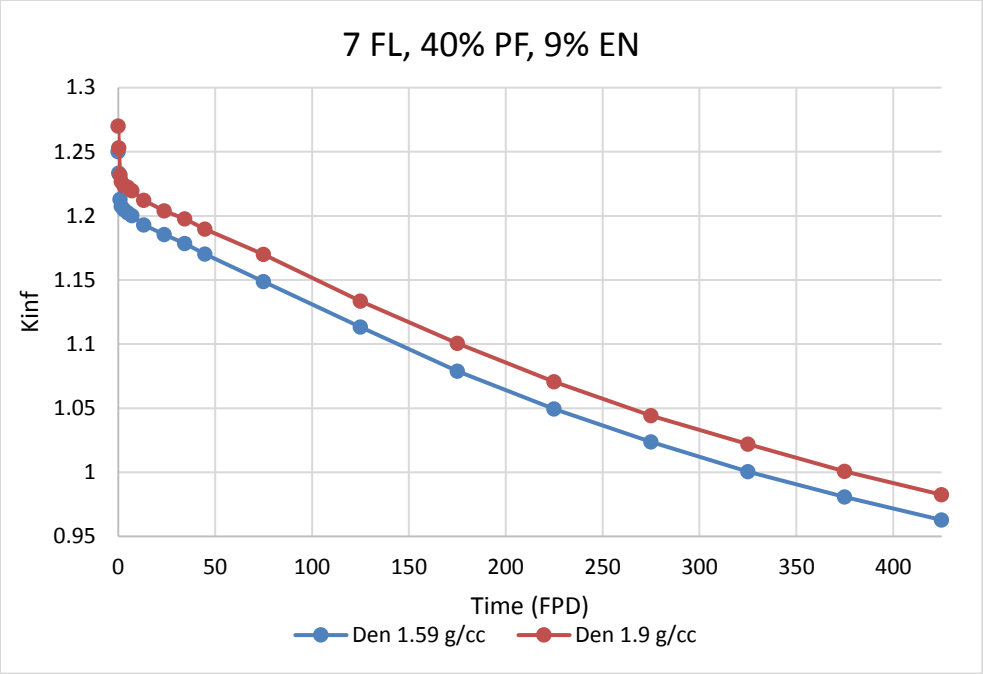

Figure 86. 2D Fuel assembly depletion calculations comparing performance of planks with different carbonaceous density for a design with 7 FL, 40% PF, and 9% EN.

REFERENCES

[1] P. Avigni, “On-line Refueling for the Advanced High Temperature Reactor.” Ph.D. Thesis, Georgia Institute of Technology, 2017

[2] P. Avigni, “Thermal Hydraulic Modeling of the Advanced High Temperature Reactor for the Evaluation of Steady State and Transient Conditions.” Master’s Thesis, Politecnico Di Milano, 2012.

[3] P. Avigni, B. Petrovic, “Fuel Element and Full Core Thermal-Hydraulic Analysis of the AHTR for the Evaluation of the LOFC Transient, Annals of Nuclear Energy, 64, 499-510 (2014). http://dx.doi.org/10.1016/j.anucene.2013.05.029, 2013

[4] Cantor, S., Density and viscosity of several molten fluoride mixtures. ORNL/TM-4308, Oak Ridge National Laboratory (ORNL), 1973.

[5] Cisneros, A. T., & Ilas, D., “Neutronics and Depletion Methods for Parametric Studies of Fluoride-Salt-Cooled High-Temperature Reactors with Slab Fuel Geometry and Multi-Batch Fuel Management Schemes”. PHYSOR 2012, Knoxville, Tenn., April 15-20, CDROM (2012).

[6] Cybenko, G. 1989. Approximation by superpositions of a sigmoidal function Mathematics of Control, Signals, and Systems, 2(4), 303–314.

[7] Driscoll, M., J., et al., The Linear Reactivity Model for Nuclear Fuel Management, American Nuclear Society (1990).

[8] Duderstadt, J. J., & Hamilton, L. J. (1976). Nuclear Reactor Analysis. John Wiley & Sons, Inc. Ann Arbor, Michigan, United States of America.

[9] Fratoni, M. (2008). Development and applications of methodologies for the neutronic design of the Pebble Bed Advanced High Temperature Reactor (PB-AHTR). Ph.D. Thesis, University of California, Nuclear Engineering,Berkeley.

[10] Gentry, C., “Development of a Reactor Physics Analysis Procedure for the Plank-Based and Liquid Salt-Cooled Advanced High Temperature Reactor." Ph.D. Thesis, University of Tennessee, 2016.

[11] Gentry, C., Maldonado, G.,I., Chvala, O., Petrovic, B., “Neutronic Evaluation of a Liquid Salt Cooled Reactor Assembly,” Nuclear Science Engineering, 2017

[12] He, K., Zhang, X., Ren, S., and Sun, J. Delving deep into rectifiers: Surpassing Human-level Performance on ImageNet Classification. In IEEE International Conference on Computer Vision (ICCV), 2015.

[13] Holcomb, D. E., Ilas, D., Varma, V. K., Cisneros, A. T., Kelly, R. P., & Gehin, J. C., "Core and Refueling Design Studies for the Advanced High Temperature Reactor," ORNL/TM-2011/365, Oak Ridge National Laboratory, Oak Ridge, Tenn. (September 2011).

[14] Holcomb, D., Peretz, F., & Qualls, A., "Advanced High Temperature Reactor Systems and Economic Analysis," ORNL/TM-2011/364 Oak Ridge National Laboratory, Oak Ridge, Tenn. (September 2011).

[15] Huang, M., & Petrovic, B., "Use of MCDancoff Correction Factor for Multi-Group Fuel Depletion Analysis of Liquid Salt Cooled Reactors," PHYSOR 2014, Kyoto, Japan, September 28th – October 3rd, CD-ROM (2014).

[16] Kelly, R., & Ilas, D., "Verification of a Depletion Method in SCALE for the Advanced High Temperature Reactor," PHYSOR 2012, Knoxville, Tenn., April 15-20, CD-ROM (2012).

[17] Kingma, D., Ba., J., Adam: A method for stochastic optimization. arXiv preprint arXiv:1412.6980, 2014.

[18] Kingsbury, C. W. (2015). Fuel Cycle Cost and Fabrication Model for Fluoride-Salt High-Temperature Reactor (FHR) "Plank" Fuel Design Optimization. Master's Thesis, Georgia Institute of Technology, Nuclear and Radiological Engineering, Atlanta.

[19] C. Kingsbury, B. Petrovic, "Updated Fuel Cycle Cost Model of the Fluoride-salt-cooled High-temperature Reactor (FHR) Based on Neutronic Calculations Using MC Dancoff Factors", Proc. Advances in Nuclear Fuel Management V (ANFM 2015), Hilton Head Island, SC, March 29 – April 1, 2015.

[20] Leo Breiman, Bagging predictors, Machine Learning, v.24 n.2, p.123-140, Aug. 1996.

[21] Lewis, S. M. (2014). Simplified Core Physics and Fuel Cycle Cost Model for Preliminary Evaluation of LSCR Fueling Options. Master's Thesis, Georgia Institute of Technology, Nuclear and Radiological Engineering, Atlanta.

[22] S. Lewis, B. Petrovic, "Determining the Equivalent Reactivity of a LSCR 2D Fuel Assembly and 3D Full Core Models," Trans. Am. Nucl. Soc., 109, 1402-1404 (2013).

[23] S. Lewis, B. Petrovic, "Simplified Fuel Cycle Cost Model Applied to LCSR Parametric Studies," Trans. Am. Nucl. Soc., 109, 1476-1479 (2013).

[24] Marsden, B. J., Haverty, M., Bodel, W., Hall, G. N., Jones, A. N., Mummery, P. M. & Treifi, M. (2016) Dimensional change, irradiation creep and thermal/mechanical property changes in nuclear graphite, International Materials Reviews, 61:3, 155-182, DOI:10.1080/09506608.2015.1136460

[25] Nagley, S., Barnes, C., Husser D. L., Nowlin, M. L., Richardson, W. C., "Fabrication of Uranium Oxycarbide Kernels for HTR Fuel," INL/CON-10-18858 Idaho National Laboratory, Idaho Falls, Idaho (October 2010).

[26] Srivastava N., Hinton G., Krizhevsky A., Sutskever I., Salakhutdinov R., Dropout: a simple way to prevent neural networks from overfitting, The Journal of Machine Learning Research, v.15 n.1, p.1929-1958, January 2014.

[27] Petrovic, B., & Maldonado, G. I., "Final Report: Fuel and Core Design Options to Overcome the Heavy Metal Loading Limit and Improve Performance and Safety of Liquid Salt Cooled Reactors," SRC#00128483, Georgia Institute of Technology & University of Tennessee, Atlanta, Georgia (April 2016).

[28] Phaisangittisagul E., An Analysis of the Regularization Between L2 and Dropout in Single Hidden Layer Neural Network, Intelligent Systems, 7th International Conference on Intelligent Systems, Modelling and Simulation (ISMS), Bangkok, Thailand, 2016.

[29] Scale: A Comprehensive Modeling and Simulation Suite for Nuclear Safety Analysis and Design, ORNL/TM-2005/39, Version 6.1, June 2011. Available from Radiation Safety Information Computational Center at Oak Ridge National Laboratory as CCC-785

[30] Scale: A Comprehensive Modeling and Simulation Suite for Nuclear Safety Analysis and Design, ORNL/TM-2005/39, Version 6.2.1, August 2016. Available from Radiation Safety Information Computational Center at Oak Ridge National Laboratory as CCC-834

[31] Storn, R., K.V. Price, "Differential Evolution - A Simple and Efficient Heuristic for Global Optimization over Continuous Spaces", Journal of Global Optimization, 11: 341–359, 1997

[32] Van Dam, E. R., Den Hertog, D., Husslage, B. G. M., & Rennen, G. (2011). Space-filling Latin hypercube designs for computer experiments. Optimization and Engineering, 12(4), 611-630. DOI: 10.1007/s11081-010-9129-8

[33] Varma, V.K., Holcomb, D.E., Peretz, F.J., Bradley, E.C., Ilas, D., Qualls, A.L., Zaharia, N.M., 2012. AHTR mechanical, structural, and neutronic preconceptual design. Oak Ridge National Laboratory, ORNL/TM-2012/320.

[34] Zielinski, K., Peters, D., Laur, R.: Stopping Criteria for Single-Objective Optimization. In: Proceedings of the Third International Conference on Computational Intelligence, Robotics and Autonomous Systems, Singapore (2005)